III-Nitride Nanowire Heterostructures: p-Type Conduction and High Efficiency Infrared and Ultraviolet Light Sources

Huy Binh Le

Department of Electrical and Computer Engineering
Faculty of Engineering
McGill University
Montreal, Canada

October 2016

A thesis submitted to McGill University in partial fulfillment of the requirements
of
the degree of Doctor of Philosophy

To my Wife- Hong Nhung Tran and my Family

Table of Contents

Abstract

The molecular beam epitaxy growth, fabrication, characterization and device applications of III-nitride nanowire heterostructures on Si (111) are presented in this dissertation. By improving the epitaxial growth process, we have achieved, for the first time, *p*-type conduction of InN. We report on the observation of ambipolar transport characteristics of InN:Mg nanowires at room-temperature, providing unambiguous evidence that the Fermi level is fundamentally unpinned on the grown surfaces of InN. Furthermore, our work suggests that defects and the incorporation of impurities on the grown surfaces of InN are the primary causes of the commonly measured accumulation of electrons and Fermi-level pinning. We also report on the achievement of electroluminescence emission of single InN *p*-*i*-*n* nanowire light emitting diodes (LEDs). Electroluminescence emission with a peak energy of 0.71 eV (1.75 μm) was observed at 77 K. The measurement of near-bandgap electroluminescence provides unambiguous evidence for the achievement of *p*-type conduction of InN.

We have demonstrated the selective area epitaxial growth (SAG) of $Al_xGa_{1-x}N$ nanowire arrays using Ti mask. We show that the luminescence peak emission of the AlGaN nanowires grown by SAG technique can be tuned from 327 nm to 210 nm. The AlGaN deep ultraviolet (DUV) LEDs operating at 279 nm exhibit excellent optical and electrical performance, including an internal quantum efficiency (IQE) of ~45% at room-temperature and a light output power of ~3.5 W/cm^2 at an injection current of 500 A/cm^2. By further exploiting the advantages of SAG $Al_xGa_{1-x}N$ nanowire arrays, we have also demonstrated that nearly dislocation-free semipolar AlGaN templates can be achieved on *c*-plane sapphire substrate through controlled nanowire coalescence

by selective-area epitaxy. The coalesced Mg-doped AlGaN layers exhibit superior charge carrier transport properties, including a free hole concentration of ~7.4×10^{18} cm^{-3} and mobility ~8.85 $cm^2/V\cdot s$ at room-temperature. The semipolar AlGaN UV LEDs demonstrate excellent optical and electrical performance, including an IQE of ~83% at room-temperature and a device turn-on voltage of ~3.3 V. This work establishes the use of engineered nanowire structures as a viable architecture to achieve large-area, dislocation-free planar photonic and electronic devices. This unique concept will also enable the scaled up manufacturing of large-area, low-cost semipolar/nonpolar GaN and/or AlN templates/substrates.

We also report on the demonstration of GaN/AlGaN nanowire edge emitting lasers operating in the UV spectral range. The nanowire heterostructures were monolithically grown on sapphire substrate using a selective area growth process. The nanowire lasers exhibited an ultralow threshold current of ~10.6 mA at room-temperature under continuous wave operation. This work provides a viable approach for achieving conventional edge emitting lasers by using nearly dislocation-free nanowire structures, thereby offering a new avenue for achieving ultralow threshold ultraviolet lasers that were not previously possible.

Abrégé

L'épitaxie par jets moléculaires, la fabrication, la caractérisation et les applications des dispositifs à base de nanofils en III-N sur un substrat de Si (111) sont présentés dans cette thèse. En améliorant considérablement le processus de croissance épitaxiale, nous avons réalisé, pour la première fois, la conductivité de type p du InN. Nous rapportons l'observation des caractéristiques de transport ambipolaire dans les nanofils en InN:Mg à température ambiante, prouvant que le niveau de Fermi est fondamentalement désépinglé sur les surfaces en InN. En outre, notre travail suggère que les défauts et l'incorporation d'impuretés sur les surfaces en InN sont les principales causes d'accumulation d'électrons communément mesurée et l'épinglage du niveau de Fermi. Nous rapportons également sur la réalisation des émissions par électroluminescence de diodes électroluminescentes (LED) p-i-n composées de nanofils uniques en InN. Des émissions avec une énergie de pointe de 0,71 eV (1,75 um) ont été observées à 77 K. La mesure de l'électroluminescence au quasi-bandgap fournit une preuve sans équivoque pour la réalisation de conductivité de type p du InN.

Nous avons démontré la croissance épitaxiale sélective (SAG) de réseaux de nanofils d'$Al_xGa_{1-x}N$ en utilisant un masque en Ti. Nous montrons que l'émission de lumière des nanofils en AlGaN obtenus par la technique SAG peut être variée de 327 nm à 210 nm, couvrant le spectre ultraviolet en entier. Notre LED en AlGaN fonctionnant à 279 nm démontre d'excellentes performances optiques et électriques, y compris une efficacité interne quantique (IQE) de ~ 45% à la température ambiante et une puissance de sortie lumineuse de ~ 3,5 W/cm^2 avec un courant d'injection de 500 A/cm2. En exploitant davantage la SAG de réseaux de nanofils en $Al_xGa_{1-x}N$, nous avons également démontré que l'AlGaN semi-polaire presque libre de dislocations peut être

obtenu sur un substrat de saphir grâce à la coalescence des nanofils contrôlée par SAG. Ces couches d'AlGaN dopées de Mg présentent des propriétés supérieures de transport de porteurs de charge, y compris une concentration de trous libres de ~7.4×10^{18} cm^{-3} et de mobilité ~8,85 $cm^2/V\cdot s$ à température ambiante. Les LEDs UV en AlGaN semi-polaire démontrent d'excellentes performances optiques et électriques, y compris une IQE de ~ 83% à température ambiante et un seuil de tension de ~3,3 V. Ce travail établit l'usage des structures de nanofils afin de produire des dispositifs photoniques et électroniques à grande surface et libre de dislocations. Ce concept unique permettra également la fabrication à grande échelle et à faible coût de GaN semi-polaire/apolaire et/ou d'AlN.

Nous rapportons finalement sur la démonstration de diodes laser en nanofils de GaN/AlGaN émettant dans la gamme spectrale UV. La croisance monolithique des hétérostructures de nanofils a été effectué sur substrat de saphir en utilisant un processus de croissance sélective. Les lasers en nanofils présentent un courant de seuil ultra-faible de ~10.6 mA à température ambiante et onde entretenue. Ce travail fournit une approche viable pour la réalisation de diodes laser classiques en utilisant des structures de nanofils pratiquement sans dislocation, offrant ainsi une nouvelle voie pour la réalisation de lasers ultraviolets à seuils ultra-faibles ce qui n'était pas possible auparavant.

Acknowledgement

This doctoral dissertation would not be completed successfully without the supervision, support and encouragement from many people. I would like to express my sincere appreciation to every individual who was involved in this thesis work.

First of all, I would like to express my great and sincere gratitude to my brilliant, knowledgeable supervisor, Professor Zetian Mi who has provided tremendous support during my PhD study in both personal life and research. Most impressively, he has endless motivation and is available almost 24/7 to discuss about my projects, suggest solutions and new ideas. Under his supervision, I have achieved not only a great progress in research work but also research attitude as well as motivation. This dissertation would not be possible without his guidance, advice and encouragement. I would also like to express my sincere appreciation to Professor Ishiang Shih and Professor Vamsy Chodavarapu for their valuable questions, comments and suggestions during examinations and evaluation of the thesis work. I also wish to acknowledge my PhD defense committee members, Professors Thomas Szkopek, Xiuyu Liu, Jun Song, Pouya Valizadeh for their interest, evaluation and valuable suggestions.

I am sincerely grateful to my co-supervisor, Professor Thomas Szkopek for insightful discussions and advices about transport measurements and other research topics. My special appreciation is to his generosity for my access to his lab tools and setups.

During my PhD study, I am greatly indebted to my group members for their assistance and discussions. My special thanks to: Dr. Saeed Fathololoumi, Dr. Hieu P. T. Nguyen, Dr. Songrui Zhao, Dr. Qi Wang, Dr. Shamsul Arafin, Dr. K. H. Li, Dr. Yong Ho Ra, Dr. Omid Salehzadeh, Hong Nhung Tran, M. Hadi Tavakoli Dastjerdi, Mehrdad Djavid, Andy Shih, Shizhao Fan, Bander

Alotaibi, Sharif M. Sadaf, Md Golam Kibria, Ashfiqua Connie, M. F. A. Chowdhury, Yongjie Wang, Renjie Wang, Yuanpeng Wu, Roksana Rashid, and Xianhe Liu. A special thank is to David Laleyan for translating the abstract to French.

Besides the great assistance from my group members, I wish to express my great appreciation to our collaborators including Professor Gianluigi A.Botton, Steffi Y. Woo, A. Pofelski at McMaster University for (S)TEM studies. Great appreciation I would like to send to McGill nanotools microfab members, including Dr. Matthieu Manini, Donald Berry, Jun Lee, Dr. Lino Eugene, Dr. Zhao Lu, Dr. Sasa Ristic, Peng Yang for their technical supports and discussions. I would also like to thank Nicole MacDonald, Jean-Philippe Masse, Christophe Clément and Marie-Hélène Bernier at Ecole Polytechnique, Montreal for their support, training, discussion on FIB, TEM, EBL and cleanroom tools.

Last but not least, I would like send my great gratitude to my grandparents, my parents Huy-Son Le and Thi-Hang-Nga Nguyen, my parents-in-law Van-Thuc Tran and Thi-Hoa Luong and all my brothers, sisters and relatives for their love, support, encouragement and strong belief in my study. Sincere and special thanks are dedicated to my wife also my colleague, Hong-Nhung Tran and our beloved daughter Tran-Thanh-Thu Le who have been always with me under any circumstance, I am thankful for her endless support, assistance, patience, encouragement and love.

This thesis work would not be possible without financial support for equipment and facilities. I am thankful to Natural Sciences and Engineering Research Council of Canada (NSERC), the Fonds de recherché sur la nature et les technologies, Canada Foundation for Innovation, and the Hydro-Quebec Nano-Engineering Program at McGill University for their financial supports to my research.

List of Figures

List of Tables

List of Acronyms

2D	Two Dimension
CBE	Chemical Beam Epitaxy
CCD	Charge Coupled Device
CVD	Chemical Vapor Deposition
CBM	Conduction Band Minimum
CNL	Charge Neutral Level
DH	Double Heterostructure
DUV	Deep Ultraviolet
EBL	Electron Beam Lithography
EL	Electroluminescence
ELO	Epitaxial Lateral Overgrowth
EQE	External Quantum Efficiency
FET	Field Effect Transistor
FIB	Focused Ion Beam
FRS	Free Spectral Range
FWHM	Full Width at Half Maximum
HAADF	High Angle Annular Dark Field
HEMT	High Electron Mobility Transistor
HVPE	Hydride Vapor Phase Epitaxy
IQE	Internal Quantum Efficiency
IR	Infrared

LED	Light Emitting Diode
LD	Laser Diode
MBE	Molecular Beam Epitaxy
MOCVD	Metal-Organic Chemical Vapor Deposition
MOVPE	Metal-Organic Vapor-Phase Epitaxy
MOSFET	Metal-Oxide-Semiconductor Field-Effect Transistor
MQW	Multiple Quantum Well
NIR	Near Infrared
NW	Nanowire
PAMBE	Plasma Assisted Molecular Beam Epitaxy
PL	Photoluminescence
QCSE	Quantum Confined Stark Effect
QD	Quantum Dot
RF	Radio Frequency
RIE	Reactive-Ion Etching
SAE	Selective Area Epitaxy
SAG	Selective Area Growth
SEM	Scanning Electron Microscopy
SIMS	Secondary Ion Mass Spectroscopy
STEM	Scanning Tunneling Electron Microscope
TD	Threading Dislocation
TE	Transverse Electric
TEM	Transmission Electron Microscopy

TM	Transverse Magnetic
UV	Ultraviolet
VBM	Valence Band Maximum
VLS	Vapor-Liquid-Solid
XRD	X-Ray Diffraction

Contribution of Authors

This dissertation works includes a collection of manuscripts written by the candidate and his supervisor, Professor Zetian Mi. The results presented in this thesis are the collaborations of many individuals with their valuable contributions. The molecular beam epitaxial growth of nanowire and nano-stripe structures was performed by Dr. S. Zhao, X. Liu and the candidate. The patterns for selective area epitaxial growth were prepared by X. Liu and the candidate. The (S)TEM studies including imaging and analysis were carried out by Steffi Y. Woo, A. Pofelski, Prof. G. A. Botton in the Canadian Centre for Electron Microscopy, a national facility supported by NSERC, the Canada Foundation for Innovation, and McMaster University. The device fabrication including single nanowire-based LEDs, single nanowire transistors, UV and DUV LEDs, plasmonic stripe lasers and edge emitting lasers was performed by the candidate with some assistance from H. N. Tran and X. Liu. Other important assistances including tool maintenance, lab organization, material orderings are greatly contributed by all lab members.

Chapter 1: Introduction

1.1. III-Nitride Optoelectronics: Current Status and Challenges

In the past decades, group III-nitride semiconductors, including InN, GaN, AlN and their alloys, have attracted a significant level of interest due to their excellent optical and electrical transport properties, including high electron mobility, large saturation velocity, large electric breakdown field, and extreme chemical stability [1-6]. Tremendous progress has been made in the development of III-nitride compound heterostructures for applications in light emitting diodes (LEDs) [7-16], laser diodes (LDs) [13, 17-23], photodetectors [24-27], solar cells [28-31], as well as high electron mobility transistors (HEMTs) [32-35] and sensors [36-38]. As direct energy bandgap materials, III-nitride semiconductors can absorb and emit light covering a broad wavelength range, from the deep ultraviolet (DUV), through the visible, to the near infrared wavelengths, encompassing the entire solar spectrum, shown in Figure 1-1 [1, 2].

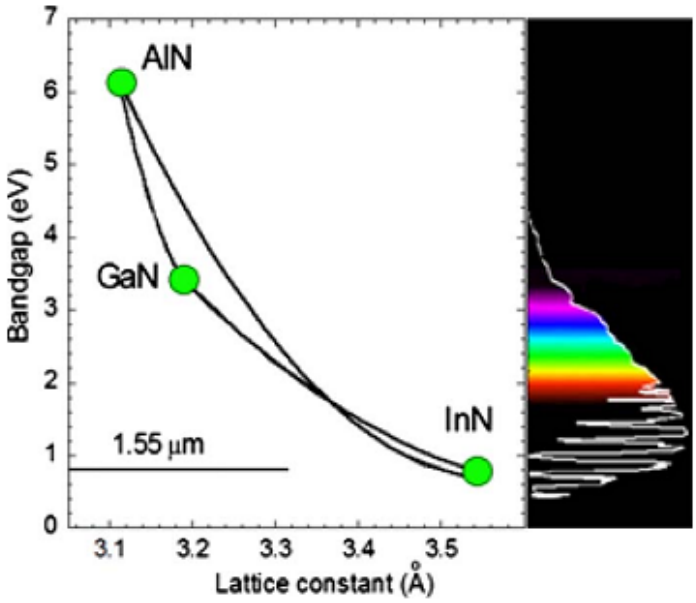

Figure 1-1: The bandgap of the group III-nitride alloys as a function of lattice constant, covering nearly entire the solar spectrum [1].

The importance of III-nitride materials in general and GaN-based materials in particular has been concretely realized by the Nobel Prize 2014 in Physics awarded to Profs. Isamu Akasaki, Hiroshi Amano, and Shuji Nakamura for their invention of GaN-based blue LEDs. Today, GaN-based materials are the materials of choice for LED lighting, radio-frequency electronics, and many others. However, the performance of conventional III-nitride quantum well LEDs and LDs exhibit very poor performance in the visible, near-infrared and UV/DUV spectral ranges, due to the presence of large densities of defects and dislocations, inefficient *p*-type conduction, and strong polarization fields and the resulting quantum-confined Stark effect. In Section 1.1.1 and 1.1.2, we provide a detailed overview of the current status and major challenges of In(Ga)N and Al(Ga)N epilayers, respectively.

1.1.1. Indium nitride (InN) and Indium-rich InGaN epilayers

To date, efforts have been largely devoted to developing GaN-based optoelectronic and electronic devices in the visible and ultraviolet spectral range. Much less efforts have been made to develop InN and In-rich InGaN alloys. Nevertheless, InN is of importance amongst III-nitride semiconductor group because of its unique properties. InN has a very narrow bandgap (~0.65 eV). There has been a 30-year history with significant efforts to unveil the real band gap of InN. The major breakthrough started from 2002. By using molecular beam epitaxy, the crystal quality of InN has been much improved. As a result, the bandgap of InN was revised from ~1.89 eV [39] to a much narrower value of ~0.65 eV [2, 40-44]. The large discrepancy in InN bandgap with previous reports is believed to be related to Burstein-Moss effect [45]. This discovery extends the fundamental bandgap, in other words, spectral range of group III-nitride semiconductors from the deep ultraviolet (DUV) at ~0.2 μm (6.2eV for AlN) to the near infrared (NIR) at ~1.9 μm (0.65eV for InN), which therefore opens up lots of potential applications. Secondly, amongst III-nitride

family, InN possesses the highest electron mobility (~12000 $cm^2/V \cdot s$) and the largest electron saturation velocity (~10^8 cm/s) at room-temperature [46, 47]. Lastly, InN has a very large absorption coefficient which is ~10^5 cm^{-1} in the visible spectrum range and ~10^4 cm^{-1} in the telecommunication wavelength (Figure 1-1) [41, 42, 45]. However, the realization of practical InN planar-based devices has been still primarily limited by three major practical challenges: (1) lack of suitable substrate; (2) unintentional propensity for *n*-type doping; (3) surface electron accumulation.

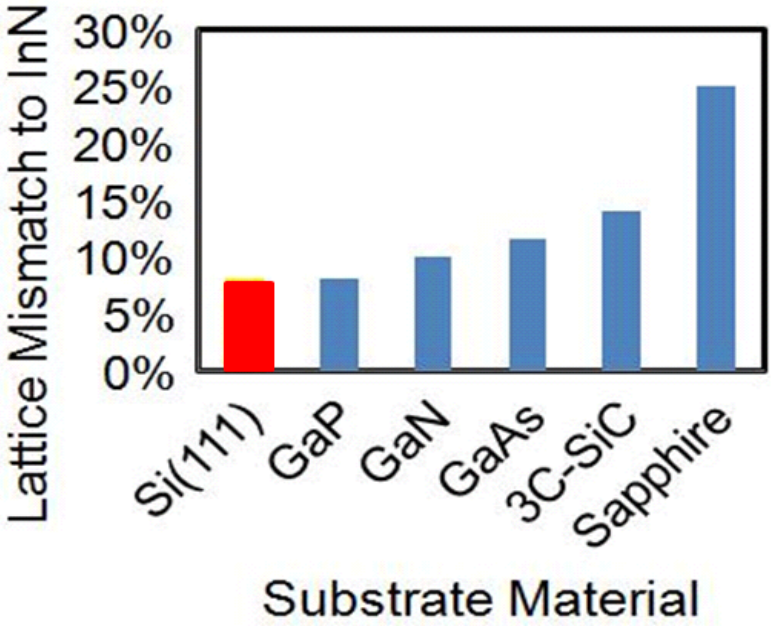

Figure 1-2: The lattice mismatch of InN to different substrates, ranging from ~7% to 27% [48].

Shown in Figure 1-2 is the lattice mismatch percentage of various commercialized substrates to InN which is in range of ~7% to ~27%. In addition, apart from Si, other substrates are very expensive which makes InN-based device growth on these substrates not practical. As seen, the lowest lattice mismatched substrate to InN is Si, which, however, is still very large, 7%. The direct consequence of large lattice mismatch is the presence of large densities of structural defects and dislocations. Those structural defects lead to other issues for InN-based applications which has

been commonly observed in other narrow bandgap materials such as InAs and InSb. Moreover, the large lattice mismatch with GaN (~11%) results in the formation of In-rich clusters in InGaN ternary compounds, due to In phase separation.

Secondly, InN has an extremely large electron affinity (~5.8eV) and the conduction band minimum (CBM) positions well below most of the defect levels. Illustrated in Figure 1-3 is the band line-ups for a range of semiconductors and insulators.

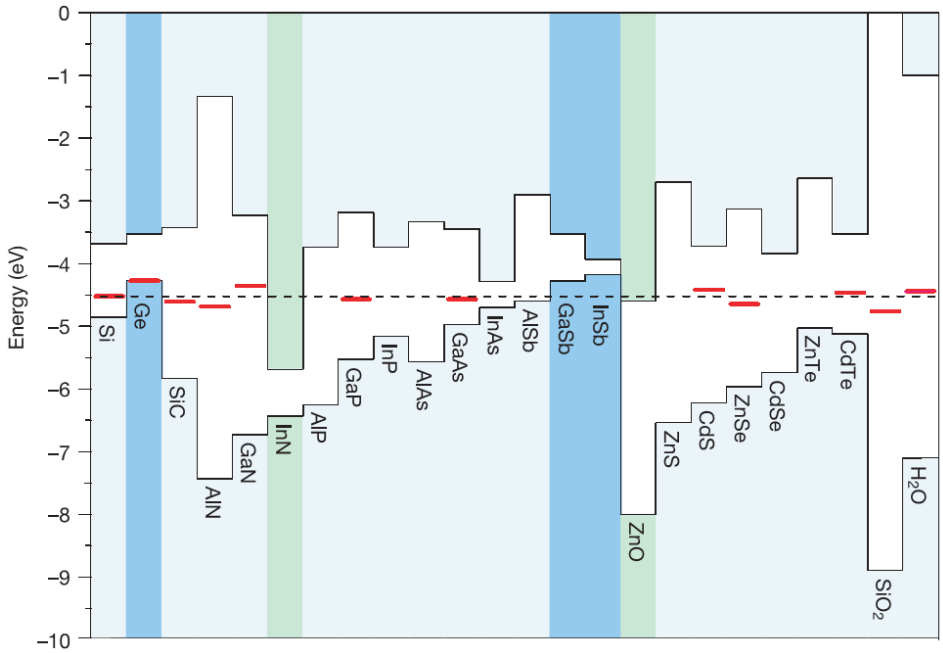

Figure 1-3: Band line-ups for various semiconductors and insulators [49].

As seen, the charge neutrality level (CNL), i.e. the location halfway Fermi level, is positioned ~1.2 eV above the CBM. Consequently, defects or impurities in InN are generally donor-like, resulting in extremely high background electron concentrations even for nominally undoped InN [50-54]. The large background electron concentration induces a large Burstein-Moss shift of the fundamental bandgap. As a consequence, the Fermi level lie inside the conduction band or other words optical absorption edge commonly measured using transmission/reflection spectroscopy is

pushed into conduction band; this explains the previous observation of a large bandgap of ~1.89 eV of InN [45]. Later on, tremendous efforts have been devoted to reducing the background electron concentration which is closely related to the improvement of material crystal quality by different growth approaches including metal-organic chemical vapor deposition (MOCVD), and plasma-assisted molecular beam epitaxy (MBE), in order to realize intrinsic InN epilayers but with limited success.

The third major challenge of InN epilayers is associated with uncontrolled surface charge property and/or surface electron accumulation which is in range of ~10^{13} cm^{-2} and have been near-universally measured on the grown surfaces of InN [51, 53, 55]. Previously, surface electron accumulation, i.e., surface Fermi-level pinning deep in the conduction band, had been considered as a fundanmental property of InN [49, 50, 56]. Later on, by using first-principles calculations, C. G. Van de Walle and D. Segev predicted that the electron accumulation could exist at polar surface, meanwhile it could be absent at non-polar planes [57]. The theory prediction is consistent with experimental results for polar surfaces [55, 58]. However, for non-polar planes, this has remained a highly debatable issue: serveral reports show the presence of surface electron accumulation[59-61], but there have been also a few experimental studies reporting an absence of electron accumulation [62-64].

Clearly, the *lack of suitable substrate, strong n-type characteristics of nominally non-doped InN, and uncontrolled surface charge properties* have severely limited the direct measurement of *p*-type conduction in InN epilayers, and further limited practical device applications of InN-based materials.

1.1.2. Aluminum nitride (AlN) and Aluminum-rich AlGaN epilayers

Optoelectronic devices, including LEDs and LDs, with emission wavelengths in the UV spectral region (200-365 nm) have been developed using Al(In)GaN-based semiconductor, which are of tremendous importance for a wide range of applications in lighting, display, air-water purification, disinfection, chemical and biochemical sensors, and white-light generation via phosphor excitation [65-67]. In the past decades, mercury and Xenon lamps have been used widely as a source of UV emission. However, these light sources are expensive, not friendly to environment due to presence of mercury, have short lifetime, and require high voltage operation[68]. More importantly, the emission wavelength cannot be tuned, limiting their practical operations. On the other hand, in contrast to mercury-based UV lamps, AlGaN-based UV LEDs are emerging as promising candidates for UV light sources because of its many advantages, including cost-effective, mercury-free, long-life, low-to-moderate voltage operations, etc. [69]. To date, however, the performance of such devices degrades considerably with decreasing operation wavelength, i.e. increasing Al content, which is mainly due to increasing densities of defects and dislocations during epitaxial growth [70-72]. For example, the currently reported maximum light output powers for AlGaN multiple quantum well (MQW) deep ultraviolet LEDs for the peak wavelengths of 241 nm, 256 nm and 284 nm are 1.1 mW, 4.0 mW and 10.6 mW, respectively [71]. The highest reported external quantum efficiency (EQE) of 279 nm emission is as low as 7% [73-75]. The internal quantum efficiency (IQE) drops drastically from ~50% to less than 1% for the LEDs operating in the wavelength range of 250-300nm to 210 nm, respectively [67, 76, 77]. The AlGaN QW lasers also exhibit very poor performance with decreasing wavelength. The shortest wavelength of electrically injected AlGaN QW laser have been reported so far is 336 nm, with the threshold current density on the order of 10 kA/cm^2 [78, 79]. To date, the major challenges of III-

nitride UV light sources are: (1) large densities of defects and dislocations; (2) inefficient *p*-doping; (3) strong polarization fields; (4) unique TM polarization of the light emission.

Large densities of defects and dislocations: As afore-described in previous Sections, III-nitride semiconductors have been grown on different kinds of substrates, such as SiC, sapphire, Si which have various lattice constants and thermal expansion coefficients, as summarized in Table 1-1 [3]. The direct consequence is related to formation of structural defects and threading dislocations (TD) and cracks during epilayer growth process [69].

Substrate Material	**Symmetry**	**Lattice Constant (Å)**	**Thermal Expansion Coefficient ($\times 10^{-6}$/K)**
Wurtzite GaN	Hexagonal	a = 3.189	5.59
		c = 5.185	3.17
Wurtzite AlN	Hexagonal	a = 3.189	4.2
		c = 5.185	5.3
α-Al_2O_3	Hexagonal	a = 4.758	7.5
		c = 12.991	8.5
Si	Cubic	a = 5.4301	3.59
GaAs	Cubic	a = 5.6533	6
6H-SiC	Hexagonal	a = 4.758	…
		c = 12.991	…
3C-SiC	Cubic	a = 4.36	…
InP	Cubic	a = 5.8693	4.5
GaP	Cubic	a = 5.4512	6.45
MgO	Cubic	a = 4.216	10.5

ZnO	Hexagonal	a = 3.252	2.9
		c = 5.213	4.75
$MgAl_2O_4$	Cubic	a = 8.083	7.45

Table 1-1: Lattice parameters and thermal expansion coefficients for III-nitride semiconductors (AlN, GaN) and the commonly used substrates.

To date, dislocation densities on the order of 10^8 cm^{-2}, or higher have been commonly measured in AlGaN and/or InGaN heterostructures grown on sapphire, SiC and other foreign substrates [13, 80, 81]. Many approaches have been investigated extensively to reduce dislocation densities, including insertion of a low temperature AlGaN/AlN layer [82, 83], pulsed atomic layer deposition technique, and epitaxial lateral overgrowth (ELO) [84-88]. With the use of epitaxial lateral overgrowth method, significantly reduced dislocation densities (~10^6 cm^{-2}) have been achieved in GaN film structures [84, 89-91]. A limitation of this approach, however, is that dislocation reduction occurs primarily over the mask regions, instead of the entire film [84, 86].

Inefficient p-doping: For III-nitride semiconductors, magnesium (Mg) is typically used as *p*-type dopant. With increasing bandgap energies from ~0.65eV for InN through ~3.4eV for GaN to ~6.2eV for AlN, the activation energies for Mg dopant also increase accordingly, i.e. ~61 meV for InN, ~166 meV for GaN, ~550 meV for AlN, respectively [92-94]. For deep UV application, inefficient *p*-doping issue becomes more pronounced. Typically, the activation energy of a Mg acceptor in $Al_xGa_{1-x}N$ increases from ~160 meV to ~500 meV with increasing Al composition from 0% to 100% corresponding to fraction x from 0 to 1, respectively [95-98] as shown in Figure 1-4, which makes the realization of high-efficiency DUV-LEDs difficult. Owning to the high acceptor ionization energy, the commonly measured hole concentration in Mg-doped AlN epilayer is as low as ~10^{10} cm^{-3} [76]. Meanwhile, the realization of *p*-type conduction in narrow bandgap

$In_yGa_{1-y}N$ have been severely limited by the commonly measured surface electron accumulation [93, 99].

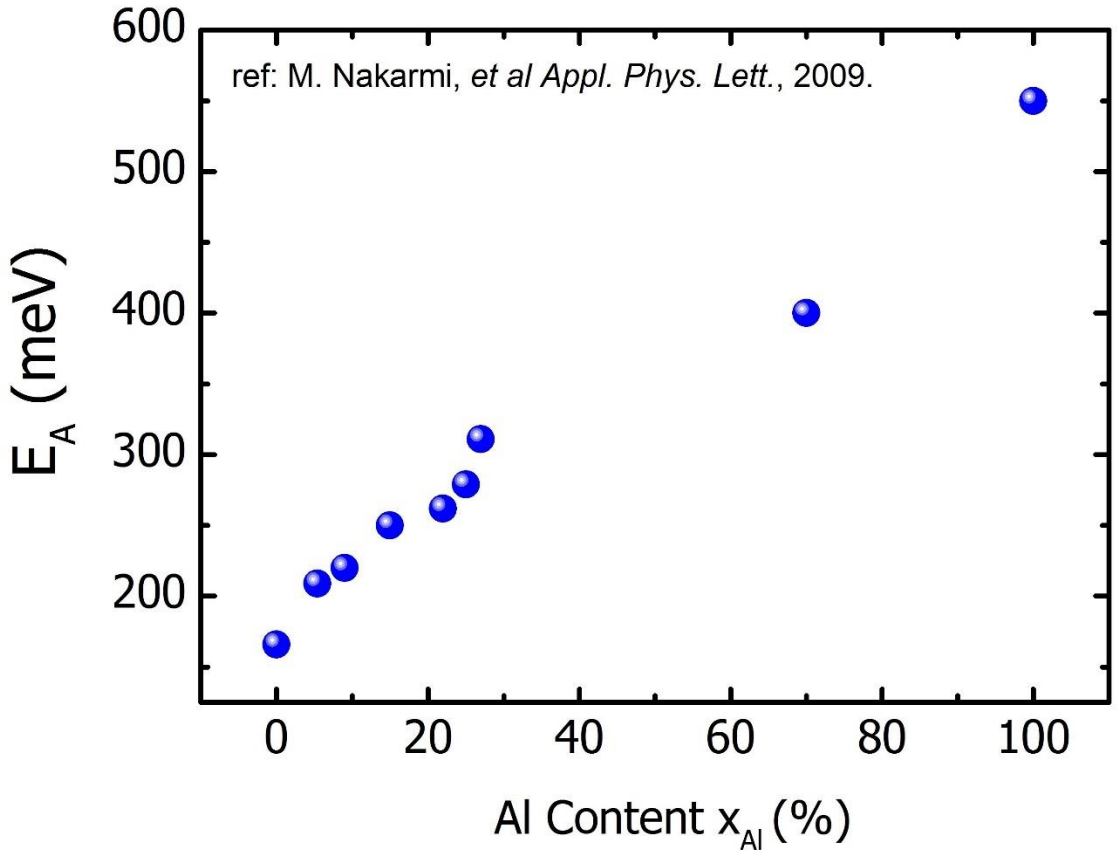

Figure 1-4: Mg acceptor energy level in $Al_xGa_{1-x}N$ alloys.

Strong polarization fields and unique TM polarization of the light emission: Another major challenge for achieving high performance LEDs and lasers operating in the deep visible and deep UV spectral ranges is the large polarization fields associated with the conventional *c*-plane of wurtzite III-nitrides [100-104]. For the $Al_xGa_{1-x}N$ epilayers grown along *c*-axis, the optical emission is strongly polarized, i.e. electric field of photoluminescence (**E**) of GaN is perpendicular to *c*-axis ($\boldsymbol{E} \perp \boldsymbol{c}$), known as transverse electric (TE) and that of AlN is parallel to *c*-axis ($\boldsymbol{E} \parallel \boldsymbol{c}$), known as transverse magnetic (TM) [105, 106]. The relative emission intensity of the

preferred/predominant polarization of the emitted light in $Al_xGa_{1-x}N$ compounds also changes significantly with the varied Al composition, shown in Figure 1-5.

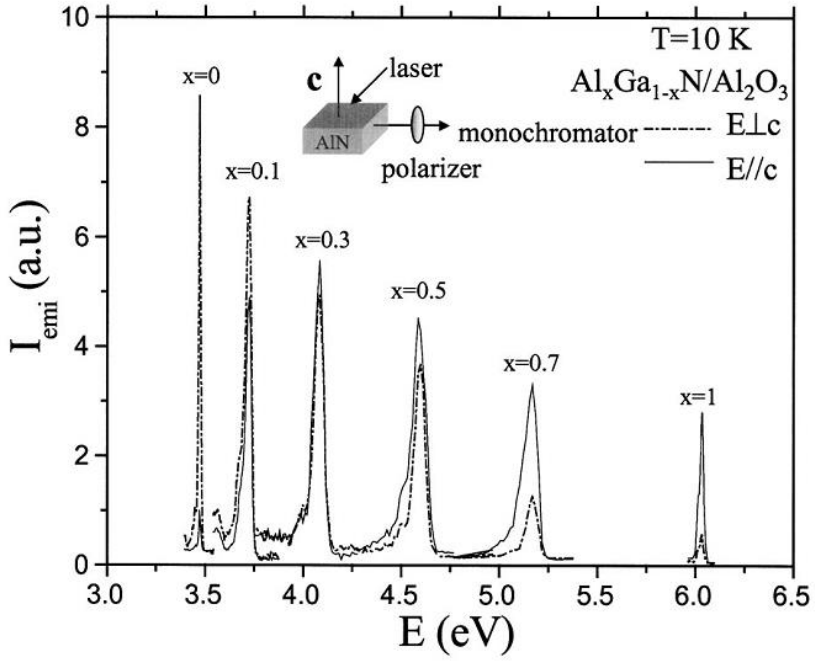

Figure 1-5: Low temperature photoluminescence (PL) spectra of $Al_xGa_{1-x}N$, showing the dependence of the electric field of PL (**E**) on its relative direction to the *c*-axis, i.e. either parallel (∥) or perpendicular (⊥). As seen, the dominant PL emission of GaN ($x = 0$) is with polarization of $\boldsymbol{E} \perp \boldsymbol{c}$ while that of AlN is with polarization of $\boldsymbol{E} \parallel \boldsymbol{c}$.

The unique light polarization property of $Al_xGa_{1-x}N$ prevents the light extraction from the top surface of conventional *c*-plane Al-rich AlGaN UV LEDs, which drastically degrades the performance of LEDs. Illustrated in Figure 1-6 is a summary of reported EQE for UV LEDs operating at different wavelength regions, in the range of 230 nm – 400 nm [107]. As can be seen, for the devices emitting in UV-C range, the EQE is on the order of ~0.1% and the output power of a few tens of nW for AlN LEDs, which are not suitable for practical applications.

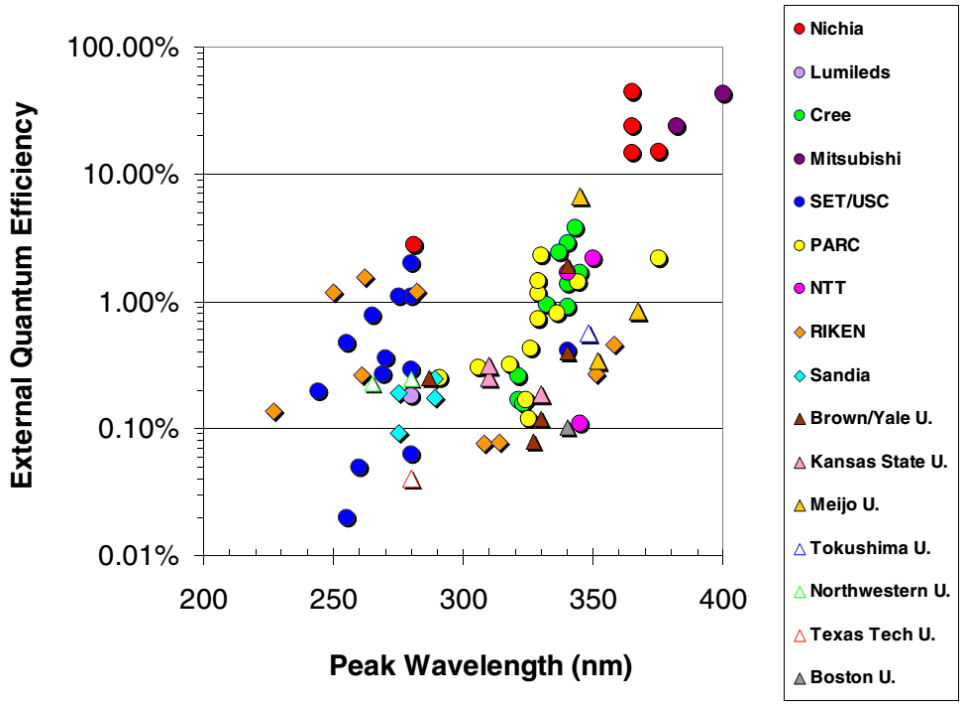

Figure 1-6: The summary of EQE for UV LEDs operating from ~230 nm to 400 nm. As seen, EQE decreases drastically for devices operating at shorter wavelengths.

To date, *large densities of defects and dislocations*, *inefficient p-doping, and* strong *polarization fields* are three major challenges of AlGaN-based UV LEDs, which have severely limited practical applications.

1.2. III-Nitride Nanowire Heterostructures: Promises and Challenges

The afore-mentioned fundamental challenges of III-nitride semiconductors can be partly alleviated by using nanowire structures due to the highly efficient strain relaxation to nanowire lateral surface [108]. So far, research studies have shown that it is possible to grow dislocation-free III-nitride nanowires (NWs) on various crystalline and amorphous substrates, including Si, sapphire, SiO_2 with significantly reduced dislocation densities [43, 108-115]. This redirects the worldwide research interest to develop III-nitride nanowire heterostructures. In what follows, a

brief overview of the recent development as well as current challenges of III-nitride nanowires prior to this thesis work is provided.

1.2.1. InN nanowires

1.2.1.1. Current status of nondoped InN nanowires

Given the afore-mentioned advantages of InN and nanowire structures, tremendous efforts have been devoted to grow InN nanowires as well as improve nanowire quality. To date, InN nanowires have been grown by using either the vapor-liquid-solid process or the spontaneous formation under nitrogen-rich conditions [53, 60, 113, 116-118]. Recently, both CVD and MBE have become the most popular techniques to grow InN nanowires/nanorods [53, 60, 113, 117]. The grown nanowires, however, generally exhibit tapered morphology with poor optical and electrical properties, including extremely broad PL linewidth, high background electron density and low electron mobility. For instance, illustrated in Figure 1-7 is the typical photoluminescence spectra of nondoped InN nanowires grown on Si (111) substrate by MBE [59].

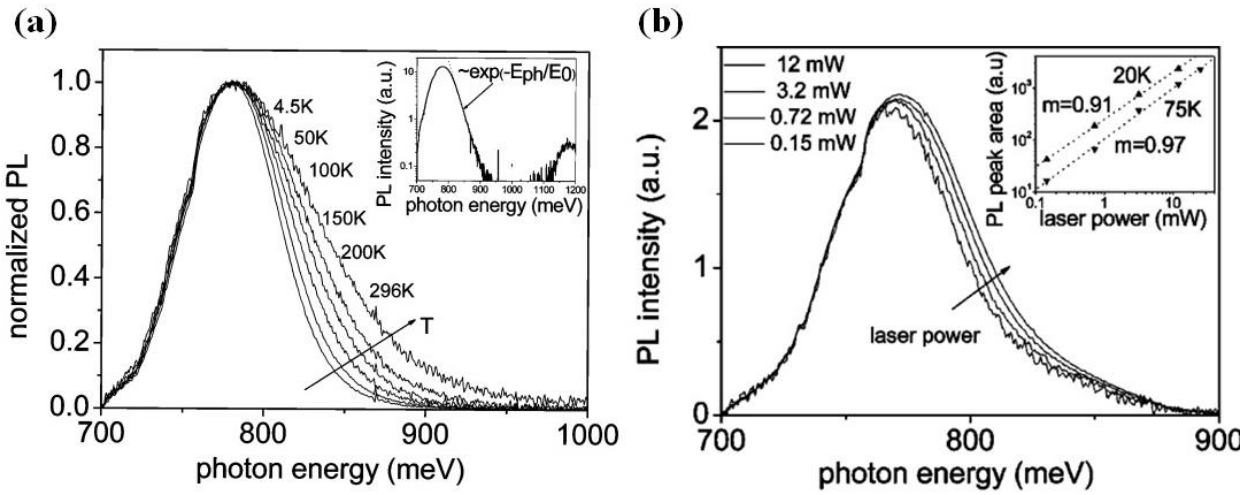

Figure 1-7: (a) Temperature-dependent and (b) excitation power-dependent photoluminescence spectra of nominally non-doped InN nanowires [59].

It can be seen that the full-width-at-half-maximum (FWHM) of PL spectra is very broad, i.e. ~ 80 –100 meV and the PL peak energies are noticeably higher than the bandgap energy of InN (~650 –700 meV). More importantly, the peak energies did not show dependences in both temperature and excitation power, which is largely due to the dominance of a very high background electron concentration. Moreover, the background electron concentration of nominally non-doped InN nanowires is normally in the order of 10^{18} cm^{-3} or even higher, and the electron mobility measured at room-temperature is in range of 100–470 $cm^2/V{\cdot}s$, which is much lower than theoretical calculation [53, 59, 109, 113, 118]. Increasing efforts have been devoted to further optimize InN nanowire quality and very recently by using an improved MBE growth process with carefully controlled growth parameters, non-tapered and nearly homogeneous intrinsic InN nanowires have been grown successfully for the first time [43]. The improved MBE growth includes the deposition of a thin *in situ* In seeding layer (~0.6 nm) prior to the growth initiation. At elevated temperature, it will from nanoscale droplets, which will promote the nucleation and nanowire formation later on. By utilizing this approach, nuclei size is much more well-controlled than the spontaneous formation in which the nuclei size is random. A scanning electron microscope (SEM) image of non-doped InN nanowires grown on Si substrate by this MBE process is shown in Figure 1-8.

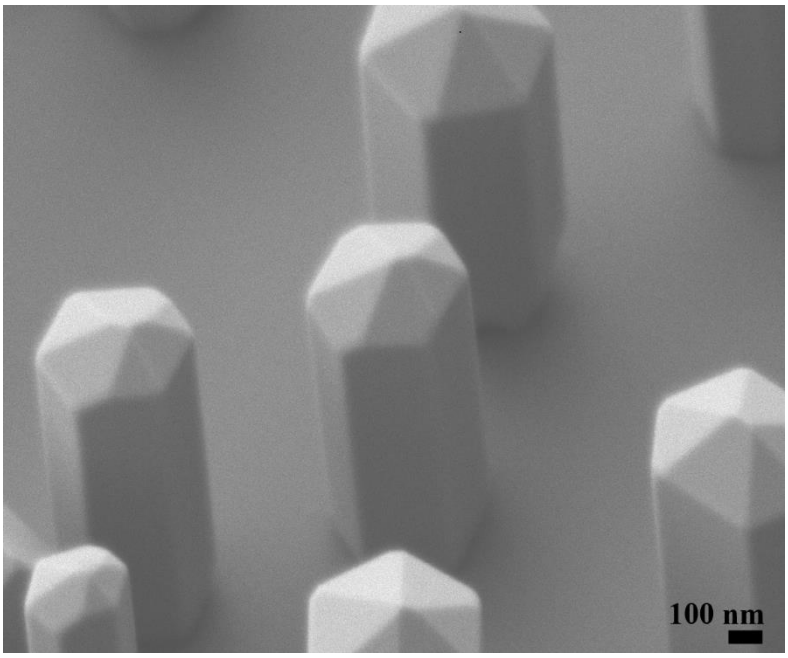

Figure 1-8: An 45°-titled SEM image of intrinsic InN nanowire grown by improve MBE technique. It is seen that the nanowires exhibit nontapperd hexagonal structure.

As seen, the nanowires exhibit nearly perfect hexagonal structure with identical top and bottom size. It is also important to mention that the direct growth of InN on Si substrate, which is the most suitable substrate in terms of lattice and thermal mismatches, is not straightforward because of the initial formation of a thin amorphous SiN_x layer [43, 119]. Detailed high-resolution transmission electron microscope (TEM) studies suggested that there is no dislocation or stacking fault in the nanowire structure. Those intrinsic InN nanowires grown by improved MBE process exhibit excellent optical and electrical properties, including extremely narrow PL linewidth of ~9 meV [120-122]. For such narrow linewidths the residual electron densities are estimated to be in range of 10^{15} cm^{-3} [121], nearly two or three orders of magnitude lower than commonly reported values for InN nanowires and thin films. The band filling effect has been clearly observed for these nanowires (Figure 1-9).

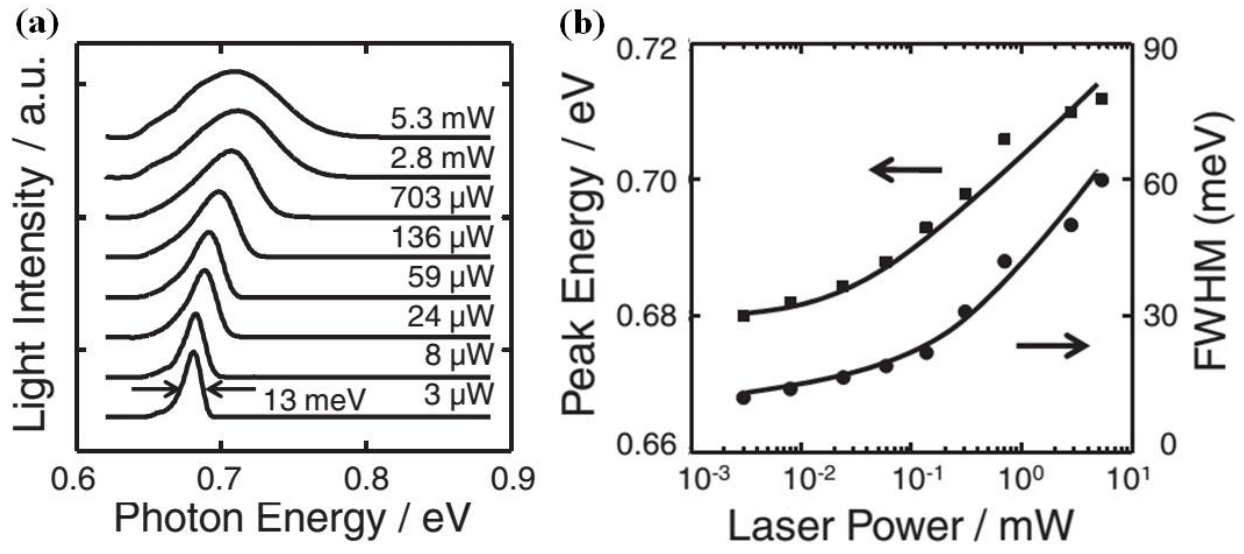

Figure 1-9: (a) Power-dependent PL spectra of a single non-doped InN nanowire measured at 5 K. (b) PL spectral linewidth and peak energy as a function of laser power at 5 K [120].

These non-doped InN nanowires grown by the improved MBE technique also show superior electrical transport properties measured by using nanoprobe technique , including room-temperature electron concentration and mobility of 10^{13} cm^{-3} and 12000 $cm^2/V{\cdot}s$, respectively [123]. The achievement of intrinsic InN nanowires with very low background electron concentration and the elimination of electron accumulation at grown surfaces are of utmost importance for InN studies, which paves the way for a direct detection of *p*-type conduction in InN and the demonstration of InN-based optoelectronic devices.

1.2.1.2. *p*-Type InN Nanowires: State of The Art and Major Challenges

As discussed in previous Sections, the recent discovery of InN with a narrow bandgap of ~0.65eV [40, 41] has generated tremendous interest for III-nitride based near-infrared optoelectronic and high speed electronic devices [124-127]. To date, however, the realization of any practical devices has been fundamentally limited by the poor material quality of conventional

InN, which generally exhibits very large background electron concentration (~10^{18} cm^{-3} or higher) [53, 55]. Moreover, surface electron accumulation has been near-universally measured on the grown surfaces of InN [51, 53, 55]. Consequently, the direct measurement of *p*-type conduction is greatly overwhelmed by the presence of an electron accumulation layer, severely limiting their practical device applications [52, 94]. To date, Mg is the most popular and effective dopant in *p*-type doping of InN although other dopants such as manganese (Mn) and zinc (Zn) have also been suggested [52, 128-132]. This is because Mg has no *d* electron and turns out to be sufficiently shallow for *p*-type doping. However, the direct achievement *p*-type conduction of Mg-doped InN has remained elusive. For example, in Mg-doped InN, hole mobility and concentration can only be estimated through *indirect* measurements, including thermoelectric-power studies and a combination of electrolyte capacitance voltage (ECV) and sheet conductivity measurements [133, 134]. The resulting hole mobility (~10 to 60 $cm^2/V \cdot s$) is also significantly smaller than that predicted for high quality InN [135]. As the result, the realization of electroluminescence (EL) emission from InN *p*-*i*-*n* diodes has not been possible.

Another issue related to the progress of *p*-type InN is associated with surface Fermi-level pinning. Recent theoretical studies suggested that the Fermi-level can be unpinned on reconstructed non-polar InN surfaces [136], and such an unpinned Fermi-level was experimentally confirmed at the *in situ* cleaved non-polar surfaces [62]. On the *grown* surfaces of InN, however, electron accumulation has been commonly measured [51, 53]. To date, these InN structures generally exhibit large densities of defects and/or dislocations, with the background electron concentration on the order of 10^{18} cm^{-3}, or higher. As a consequence, little attention has been paid to the impact of defects and impurity dopant incorporation on Fermi-level pinning and surface charge properties of InN.

As described in Section 1.2.1.1, with the afore-mentioned molecular beam epitaxial growth process, superior quality InN nanowire structures can be achieved directly on Si substrate recently [43]. In this catalyst-free growth process, the formation of surface defects and dislocations is greatly minimized [121, 122, 137]. The residual electron density can be as low as low-to-mid 10^{13} cm^{-3} for nominally non-doped InN, and the room-temperature electron mobility can reach 12000 $cm^2/V{\cdot}s$, approaching the theoretical prediction [123, 138]. More importantly, it was measured that the nanowire grown surfaces were free of surface electron accumulation for both non-doped and Mg-doped InN nanowires, which has led to the direct measurement of *p*-type conduction in Mg-doped InN [137, 139]. With the incorporation of Si dopant, however, such nanowires show clear evidence of Fermi-level pinning [121]. These studies have further added heat to the ongoing debate of the surface charge properties of InN.

1.2.2. Al(Ga)N Nanowires

As describe in previous Section, while tremendous progress has been made in Al(GaN)-planar based devices, the performance and operation of such devices are, however, fundamentally limited by the presence of large densities of defects and dislocations, the strong polarization fields, and the inefficient *p*-doping in AlGaN materials. These critical challenges can be potentially alleviated with the use of nanowire structures. Recently, with the use of nanowire structures, high efficiency LEDs have been demonstrated in the visible range [140, 141]. It has been recently showed that compared to conventional planar structure, III-nitride nanowires can be largely free of dislocations and piezoelectric polarization field [142]. Shown in Figure 1-10 is PL spectra of AlGaN nanowires, tuning from UV-A to UV-C range. In fact, nanowire structures can offer several fundamental advantages, including low defect densities, much reduced strain-induced polarization fields, and significantly enhanced Mg dopant incorporation.

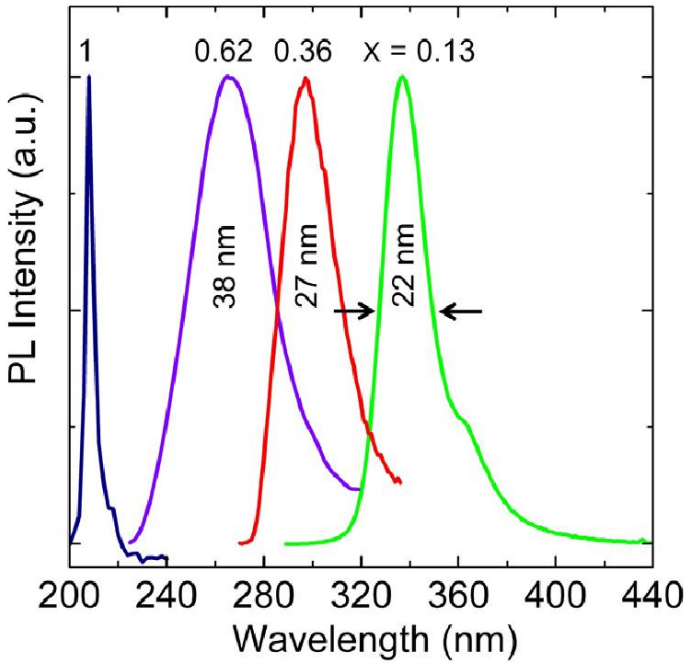

Figure 1-10: Room-temperature PL spectra of $Al_xGa_{1-x}N$ nanowires grown on Si (111) substrate by MBE with various Al composition to tune emission wavelength [143].

For example, recently, highly efficient $Al_xGa_{1-x}N$ nanowire based double heterostructure LEDs operating at ~340 nm were grown by MBE under nitrogen-rich condition. The nanowire-based devices exhibited superior electrical and optical properties, including an IQE of ~59% measured at room-temperature [144]. After that, Zhao *et al.* successfully demonstrated nearly defect-free AlN nanowires. The fabricated LEDs exhibit high efficiency DUV emission with IQE at room-temperature of ~70-80% [145], which is nearly an order of magnitude higher than planar AlN devices [77]. Moreover, as above-mentioned, emitted light of conventional *c*-plane AlN-based planar LEDs can only be extracted from the side wall because of the intrinsic TM polarization in AlN. In contrast, it has been recently shown that the dominant light emission can be from nanowire top surface along the *c*-axis due to the strong light scattering and coupling effects among the nanowires with optimized diameter and spacing [146].

Obviously, III-nitride nanowire structure offers many advantages, and have emerged as a promising candidate to achieve efficient LEDs operating in wide range emission from DUV to NIR. However, the realization of efficient nanowire LEDs operating in the DUV wavelength range has been still limited. To realize high efficiency AlGaN nanowire LEDs, any optical scattering loss related to variations of nanowire size, density, and spacing should be substantially reduced. Therefore, the epitaxial growth and structural properties of such nanowire arrays need to be carefully controlled and engineered and these issues will be experimentally solved and discussed in this thesis.

1.3. Summary of the Contribution and the Organization of this Dissertation

This thesis work has further contributed to fundamental understandings of InN nanowires by utilizing improved molecular epitaxial growth technique. By investigating the transport characteristics of InN nanowire field effect transistor, the direct evident of *p*-type conduction in InN is demonstrated which has not been shown prior to this thesis work. In the research topic, we first aim to provide a unified picture of the variation of surface charge properties of InN by examining, at the individual nanowire level, the correlation between surface Fermi-level tuning and dopant incorporation. It is observed that InN:Mg nanowires can exhibit clear ambipolar transport characteristics at room-temperature, providing unambiguous evidence that the Fermi-level is fundamentally unpinned on the grown surfaces of InN. Such a behavior, however, is not measured in Si-doped InN nanowires, which is explained by Si-donor surface segregation and the resulting electron accumulation. At room-temperature, the derived two-dimension (2D) hole concentration on the nanowire surface can reach ~5.3×10^{10} cm^{-2} in Mg-doped InN nanowires, and the hole mobility is estimated to be ~130 $cm^2/V\cdot s$. This study reveals that Fermi-level pinning is

not a fundamental property of InN, and it can be engineered through controlled dopant incorporation.

In addition, InN *p*-*i*-*n* nanowire structures were grown directly on Si (111) substrate by plasmas-assisted molecular beam epitaxy. Subsequently, such nanowire structures were transferred to SiO_x coated Si substrate for the fabrication of single InN nanowire LEDs. Electroluminescence emission with a peak energy of 0.71 eV (1.75 μm) was observed at 77 K under various injection currents for the first time. The realization of electrically injected InN nanowire LEDs has paved the way for the development of III-nitride based functional optoelectronic devices in the near-infrared wavelength range.

In the research topic on AlGaN nanowires, the thesis mainly focuses on developing AlGaN nanowires grown by selective area epitaxial growth. In this work, we have performed a detailed investigation of the selective area growth of large-area GaN/AlGaN nanowire arrays on *n*–GaN template on *c*–plane sapphire substrate. Such nanowire structures exhibit highly uniform diameter distribution and strong photoluminescence in the wavelength range of ~280 nm (UV-C) and ~340 nm (UV-B). Moreover, with the use of selective area growth technique, we have achieved dislocation-free AlGaN templates through controlled nanowire coalescence. This work demonstrates the use of dislocation-free nanowire arrays as a monolithically integrated architecture to realize high performance planar UV photonic devices. We have also demonstrated, for the first time, electrically injected AlGaN nanowire edge-emitting lasers.

The thesis is organized as follow. Chapter 1 provides a brief overview of III-nitride semiconductors including their advantages and challenges for device applications for both epilayer and nanowire structures. In this chapter, the progress to achieve intrinsic and *p*-type InN nanowires is reviewed, and the key factors that limit the performance of practical InN-based devices are also

discussed. Furthermore, we provide an overview on the recent developments and major challenges of Al-rich AlGaN epilayer and nanowire structures.

In Chapter 2, growth techniques of III-nitride nanowires, including vapor-liquid-solid, spontaneous nanowire formation in nitrogen-rich condition, and selective area epitaxial growth techniques will be discussed.

In Chapter 3, the first demonstration of *p*-type InN nanowires will be presented. In this chapter, the growth mechanism as well as transport properties of Si-/Mg-doped InN nanowires are discussed. The first observation of electroluminescence of InN nanowire-based devices will be presented, which also provides unambiguous evidence for the realization of *p*-type conduction in Mg-doped InN nanowires.

In Chapter 4, selective area epitaxial growth of $Al_xGa_{1-x}N$ nanowires by MBE is reviewed. In this chapter, we have performed a detailed investigation of the SAG of large-area ternary $Al_xGa_{1-x}N$ nanowire arrays on *n*–GaN template on *c*–plane sapphire substrate. The photoluminescence spectra of ternary AlGaN nanowires array can be tuned from 210 nm to 327 nm by varying Al content.

In Chapter 5, we present the controlled coalescence of AlGaN nanowire arrays and the demonstration of nearly dislocation-free semipolar AlGaN templates on sapphire substrate. The achievement of high efficiency semipolar AlGaN UV LEDs through controlled nanowire coalescence is also discussed.

In Chapter 6, we report on the first demonstration of electrically pumped nanowire edge-emitting laser operating in the UV spectral range. The design, epitaxy, fabrication, and performance characteristics are thoroughly discussed.

Finally, conclusion and future work are presented in Chapter 7. The future work includes in the development of AlGaN dot-in-nanowire heterostructures, the demonstration of nanowall deep UV LEDs and lasers for high power operation, and the achievement of ultralow threshold electrically pumped deep UV plasmonic lasers.

Chapter 2: Molecular Beam Epitaxial Growth of III-Nitride Nanowire Heterostructures

2.1. Introduction

Given the afore-mentioned potential advantages of III-nitride nanowire structure, tremendous efforts have been devoted to growing these materials. Many different techniques for the forming/growth/synthesis III-nitride nanowires have been developed and commonly used such as top-down dry etching, direct reaction of Ga/In metals with NH_3, chemical vapor deposition, MBE, chemical beam epitaxy (CBE), and hydride vapor phase epitaxy (HVPE). The underlying growth mechanisms have been extensively studied, involving the use of metallic catalysts in the vapor-liquid-solid (VLS) growth process, the spontaneous nanowire formation under nitrogen-rich conditions or the selective area epitaxial growth on patterned substrates. In this Chapter, an overview of the development as well as major challenges of conventional spontaneous nanowire and selective area epitaxial growth techniques will be discussed in Section 2.1 and 2.2, respectively.

2.2. Spontaneous Nanowire Formation and the Issues

As discussed in the previous Section, III-nitride nanowires have attracted tremendous attention for advanced use in future nanometer-scale electron and optical devices. Freestanding vertical nanowires/nanocolumns on substrate are increasingly attractive to III-V optoelectronic devices because of their unique properties, including dislocation-free, highly efficient light extraction, and strain relaxation properties. In the past, the common growth/synthesis techniques of III-nitride nanowires included top-down dry etching [147-149], chemical vapor deposition, VLS

[150], molecular beam epitaxy [43, 151, 152], chemical beam epitaxy [153], and hydride vapor phase epitaxy [154]. Amongst these growth processes, VLS and spontaneous nanowire formation under nitrogen-rich conditions have been extensively studied.

2.2.1. Vapor-Liquid-Solid Growth

In the early 1960s, the main approach to grow Si whiskers based on vapor-liquid-solid mechanism using catalysts and the liquid phase underneath metal particles for crystallization was pioneered by Wagner and Ellis [155]. Since then, VLS has become exceedingly common and has been used to synthesize almost all semiconductor NWs through simple procedures. In this growth process, metallic particles such as Au, Ni and Fe were used as catalyst, serve as nucleation centers and assist NWs formation. Illustrated in Figure 2-1 is the schematic diagram of VLS growth process of GaAs nanowires, which consists of 3 major steps: (i) deposition of metallic particles, followed by a formation of liquid-alloy particles when reacting with vapor source materials; (ii) crystal nucleation; (iii) axial nanowire growth when excess material dissolved in its precipitate resulting in a form of single solid nanowire at the bottom of one particle [156]. The diameter and position of nanowires grown by VLS are defined by size and position of metallic particles as well as other growth parameters, including pressure and temperature. With this technique, it has been reported that it is feasible to tailor the composition of nanowires in both axial and radial growth directions. Steps involved in the VLS growth mechanism are also presented in Figure 2-1.

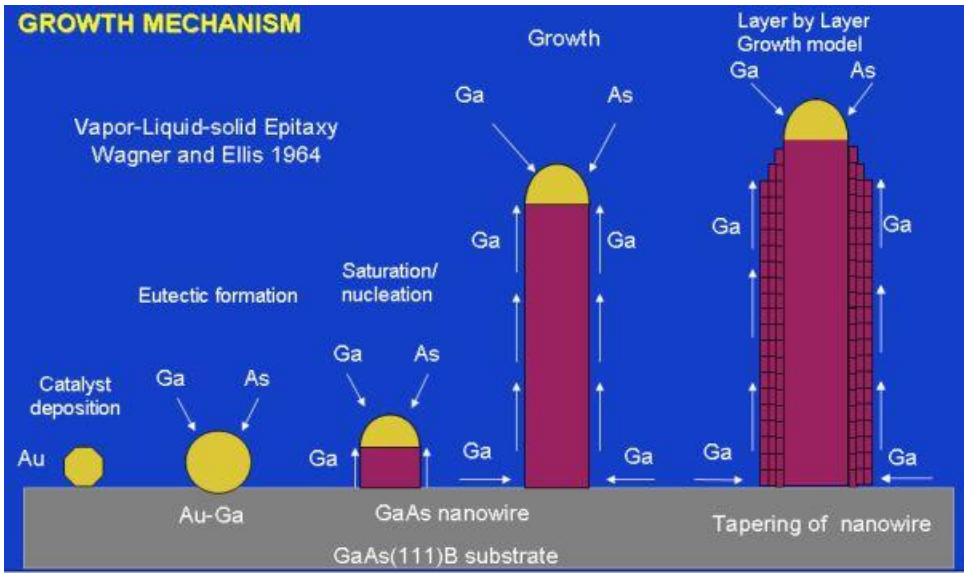

Figure 2-1: Schematic diagram of GaAs nanowire grown by VLS approach, showing entire evolution of nanowire formation [157].

The nanowire length is determined by growth rate and growth time. The growth rate mainly depends on the supersaturation of the vapor, which is affected by both source concentration and substrate temperature. As a result, the growth kinetics determine the nanowire orientation, morphology, and other structural properties [158]. III-nitride nanowire structures grown by VLS technique has been reported by using different methods, for examples, a quartz tube furnace [159], low-pressure metal-organic vapor epitaxy [160], and thermal chemical vapor deposition [161]. At that time, the VLS-like mechanism was believed to be the underlying mechanism for the directional GaN nanowire growth. Kang *et al.* reported the achievement of highly uniform and vertically aligned GaN nanowires on *c*-plane sapphire substrate by using thermal chemical vapor deposition with Ni catalysts [162].

However, the major issue of the VLS growth process is that after growth the metal catalyst which assisted nanowire formation still remains on the tip of nanowires. The metal catalysts during

the growth often diffuse into the nanowires and act as unintentional impurities and defects inside the NWs, which often degrades the optical and electrical properties [163, 164].

2.2.2. Molecular Beam Epitaxy Growth

In addition to the VLS technique, wherein the nanowires formation is through a supersaturation process, group III-nitride nanowires can also be grown spontaneously under nitrogen-rich conditions without using any foreign metal catalysts [108, 112, 151, 152]. In this growth process, the metal catalysts are not used and thus there is no catalyst droplets at the top of nanowires after growth. The MBE technique has been commonly used for the spontaneous III-nitride nanowire growth. Early observations of GaN nanowires grown by MBE were ascribed to self-catalyst mechanism, wherein Ga droplets served as metallic catalyst in VLS-like growth mechanism to assist the nanowire formation [165]. However, later studies of the spontaneous growth of GaN nanowires on Si (111) substrates by MBE has clearly proved/suggested that the growth mechanism is not related to VLS mechanism and there is no experimental observation of Ga droplets on GaN nanocolumn tips [108]. The GaN nanowires growth in MBE occurs by a distinctly different process, which is mainly due to the differences between the sticking coefficients of the group III atoms on the nanowire tip and on the *m*-plane nanowire sidewalls [152].

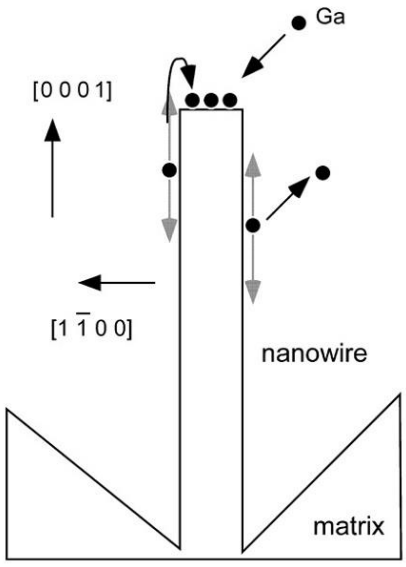

Figure 2-2: Schematic illustration of differential sticking coefficient mechanism in spontaneous nanowire formation process by using MBE. The relevant processes such as incorporation, desorption, diffusion and nucleation are included [152].

Illustrated in Figure 2-2 is the growth mechanism of GaN nanowires in MBE, in which the nanowire growth is initiated by the differences in surface energies, adatom diffusion length, sticking coefficients on different crystal planes. The sticking coefficient on the tip of nanowires is much larger than that on the sidewalls, and as a consequence, Ga atoms that impinge directly on the tip of NWs or within a surface diffusion length will be incorporated on the NWs tip, contributing to the nanowire axial growth. Meanwhile, the adatoms travelling farther down the sidewalls are likely to desorb rather than incorporate into nanowire growth. The diffusion-induced explanation agrees well with experimental observation that the vertical growth rate of nanowires increases quickly with the increase of substrate temperature, which can be ascribed to the significantly enhanced adatom migration on nanowire surfaces[151]. The radio-frequency plasma-assisted Veeco GENxplor MBE system, shown in Figure 2-3a, is used primarily for the growth

experiments presented in this thesis. Figure 2-3b shows a SEM image of GaN nanowires grown by MBE under nitrogen-rich conditions.

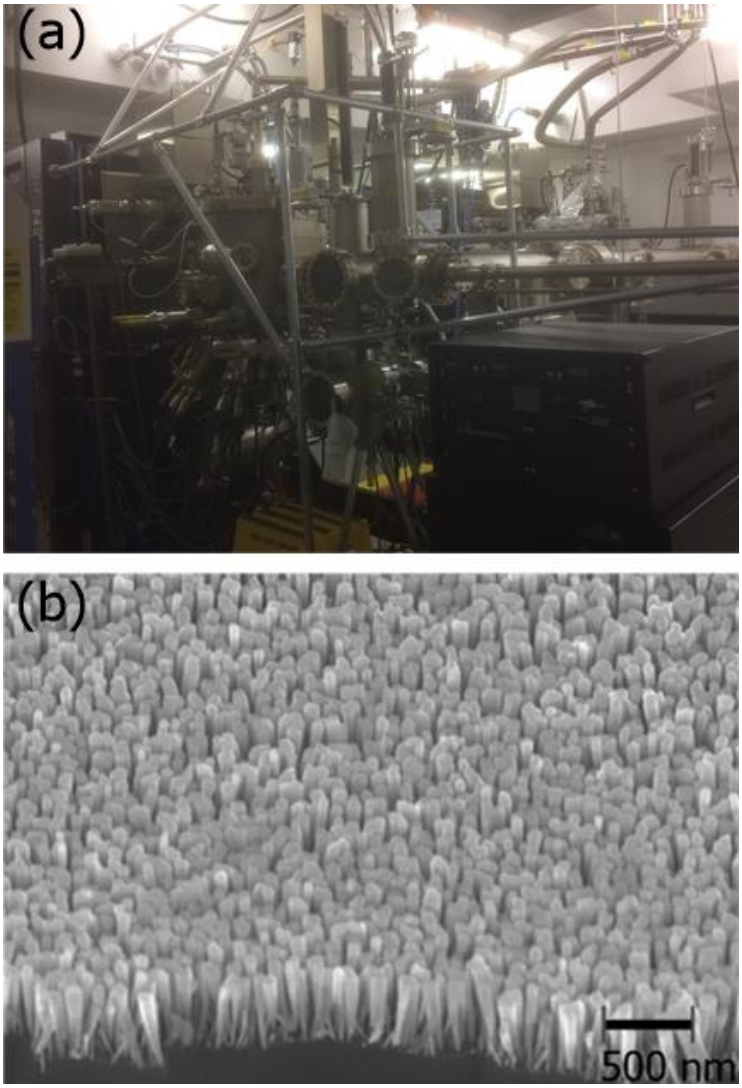

Figure 2-3: (a) GENxplor molecular beam epitaxial growth system. (b) 45°-tilted view SEM image of GaN nanowires grown by MBE.

Both VLS and self-organized spontaneous nanowire growth by MBE, however, have the following major limitations which severely hinder the practical device performance. First, the nanowire density, orientation and morphology are strongly influenced by the buffer layers and initial growth conditions, including growth pressure, substrate temperature, III/V flux ratio, growth

rate, etc. For spontaneously formed nanowires, the nanowires are often grown with high densities of ~10^{10} cm^{-2} which can result in random coalescence between neighboring wires [152, 166-168]. Due to the lack of control over their size, height, morphology, and twist/tilt in crystal orientation, [166, 167, 169, 170] however, the coalescence of such randomly mis-oriented nanowires generally leads to the presence of strain, inversion domains, low-angle grain boundaries and networks of structural defects including dislocations at the coalescence boundary [171-173].

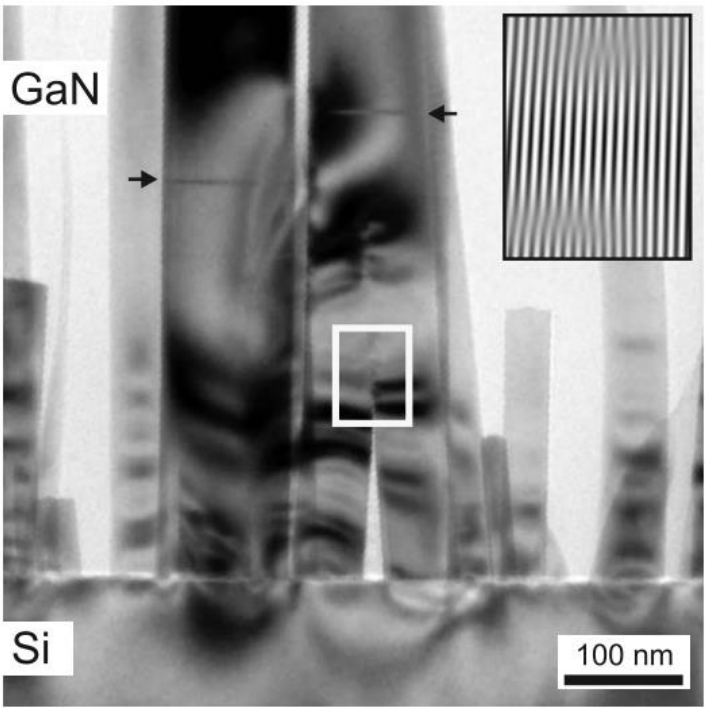

Figure 2-4: Cross-sessional STEM image of coalesced GaN nanowires. The network of structural defects including stacking faults and dislocations at the coalesced boundary are indicated by black arrows and white box.

Secondly, the performance of III-nitride optoelectronic devices fabricated from spontaneous nanowires is strongly limited by the extremely low light extraction efficiency which is mainly due to random nanowire morphology including nanowire diameter, height, density and spacing, especially for devices operating in ultraviolet spectral range. Recent studies have shown

that an unprecedentedly enhanced light extraction efficiency can be achieved by carefully controlling the nanowire morphology, including size, position and density [174].

2.3. Selective Area Growth: Importance and Challenges

The selective area growth (SAG) technique was developed in the early 1960s and was first used for Si-integrated circuit [175]. Then, Tausch *et al.* and Rai-Choudhury *et al.* were the pioneers to investigate the SAG of GaAs by using a metal-organic source [176, 177]. Later on, in 1987, Jones and Lau reported the SAG of GaAs with native oxide mask defined by a standard lithography process [178]. In these processes, nanowires were selectively grown on pre-patterned substrates, i.e., under optimal conditions, nanowires are grown only within the openings while avoiding any growth on the mask. Various SAG masks, including SiN_x, SiO_2, Ti, Al and Au templates, have been utilized [179-183]. As a well-controlled growth approach over the nanowire position, size and aspect ratio, the SAG has been developed extensively using different growth techniques, including metal-organic vapor-phase epitaxy (MOVPE) [184], metal-organic chemical vapor deposition (MOCVD) using SiNx mask [185], and plasma-assisted MBE using Ti mask [182, 186, 187]. In these studies, nanowire growth is mainly determined by adatom migration, the differences in adatom sticking coefficients between the mask and the openings [183], desorption/absorption as well as masked region, which can be controlled by pattern design and optimizing growth conditions including substrate temperature and III/V flux ratios. Recently, the Ti-mask SAG technology on GaN has been relatively well developed, which has led to the demonstration of nanowires with tunable emission wavelength by controlling nanowire diameters [188], the monolithic integration of nanocolumn-based LEDs with various emission colors [189], and green and red emitting nanowire LEDs [190, 191]. Very recently, the first demonstration of multicolor single nanowire LEDs simultaneously grown on the same substrate using selective area epitaxy

has been reported [192]. Such LEDs exhibited superior performance, paving the way for the realization of ultra-small and efficient projection displays, smart lighting and on-chip spectrometers, etc. Shown in Figure 2-5 is a SEM image of GaN nanowire arrays, exhibiting a high degree of size uniformity and are vertically aligned along the *c*-axis. Each nanowire has a well-defined hexagonal pyramid morphology comprised of six semipolar top facets.

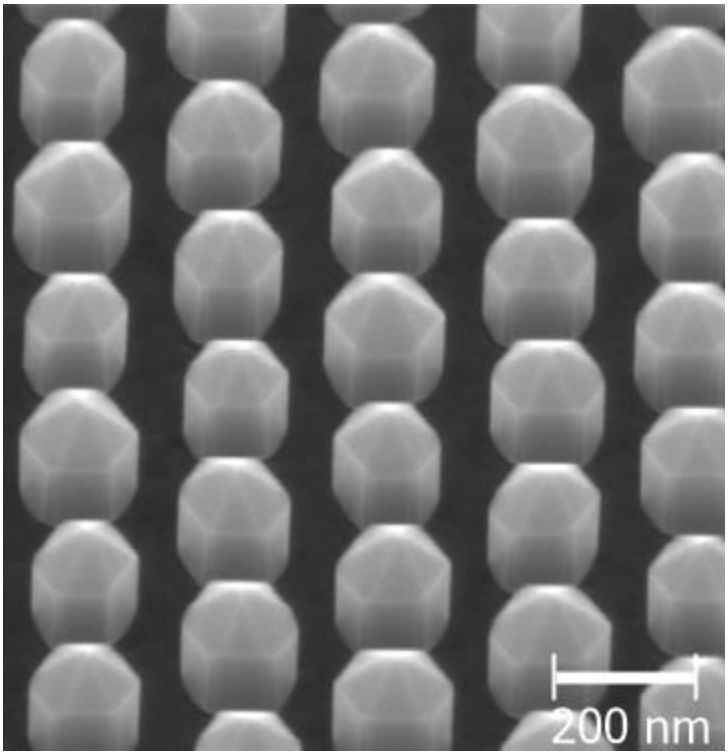

Figure 2-5: 45°-tilted view SEM image showing GaN nanowire arrays selectively grown in the opening apertures using SAG technique.

2.3.1. Ultraviolet Light Emitting Diodes Using Selective Area Epitaxy: Current Status and Challenges

III-nitride based light emitting diodes with operation wavelength in the UV spectral region are of importance for a wide range of applications in lighting, display, air-water purification, disinfection, chemical and biochemical sensors, and white-light generation via phosphor excitation [65-67]. However, the poor performance of such devices with increasing Al content is

fundamentally limited by the presence of large densities of defects and dislocations, the strong polarization fields, and the inefficient *p*-doping in AlGaN materials [70-72] . Recently, with the use of nanowire structures, high efficiency LEDs have been demonstrated in the visible range [140, 141]. Nanowire structures can offer several fundamental advantages, including low defect densities, much reduced strain-induced polarization fields, and significantly enhanced dopant incorporation. However, the realization of efficient nanowire LEDs operating in the DUV wavelength range has been very limited. To realize high efficiency AlGaN nanowire LEDs, any optical scattering loss related to variations of nanowire size, density, and spacing should be substantially reduced. Therefore, the epitaxial growth and structural properties of such nanowire arrays need to be carefully controlled and engineered. In the VLS or spontaneous formation process, III-nitride nanowire arrays generally exhibit random distribution in position and a high degree of non-uniformity in size and height distribution [144]. Such issues can be potentially addressed by using the SAG technique [193, 194]. In this process, the nanowire formation and nucleation is directly controlled by the nanoscale apertures created on a substrate using the well-defined top-down process. To date, however, SAG AlGaN nanowire LEDs with emission wavelengths covering entire UV spectral range have not been demonstrated which is ascribed to short diffusion length of Al adatom on Ti mask surface in the presence of N_2. In addition, the direct formation of high quality AlGaN nanowires by this growth process has remained elusive. Shown in Figure 2-6 is the recently demonstration of wavelength tunability of AlGaN nanowires selectively grown on Ti mask by MBE technique [195]. It can be seen from the plot of wavelength as a function of Al composition, the experimental data exhibit a discrete distribution, indicating the current challenges of selective area growth technique.

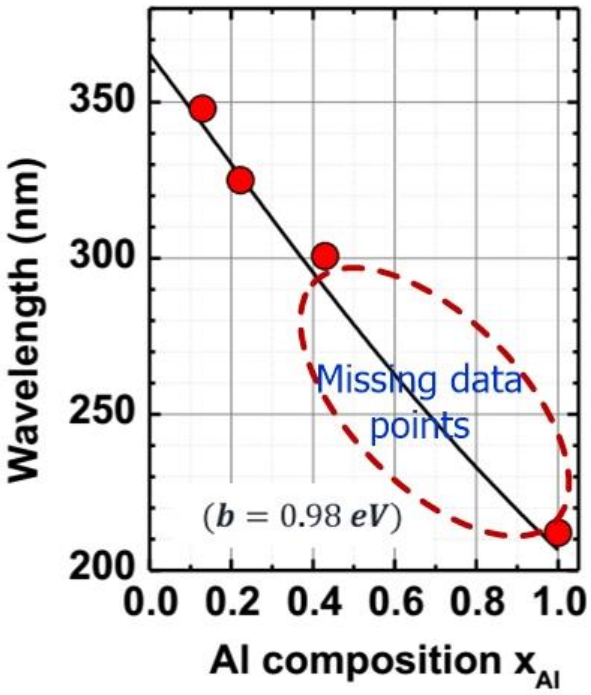

Figure 2-6: Peak wavelength of SAG AlGaN nanowires as a function of Al content.

Intriguingly, Mehrdard *et al.* has recently reported that by using periodic arrays of nanowire LEDs, in principle, an unprecedentedly enhanced light extraction efficiency of ~72% can be achieved by carefully optimizing the nanowire size, density, etc [174]. In this thesis work, we have performed a detailed investigation of SAG of large-area GaN/AlGaN nanowire arrays on *n*–GaN template on *c*–plane sapphire substrate. Such nanowire structures exhibit highly uniform morphology distribution and high luminescence efficiency in the wavelength range of ~280 nm and 340 nm. The nanowire UV LED devices exhibit excellent optical and electrical properties, including high IQE, excellent current-voltage characteristics, and high light output power, as described in the following sections.

2.3.2. Photonic and Plasmonic UV Laser by Using Selective Area Epitaxy

We have demonstrated GaN/AlGaN nanowire edge emitting lasers that can operate in the ultraviolet spectral range. To date, the performance of GaN-based lasers degrades considerably with increasing Al content, i.e. decreasing operation wavelength [78]. For example, the currently reported Ga(Al)N UV edge emitting lasers generally exhibit threshold current density ~10 kA/cm^2, or higher [78, 196-199]. The shortest wavelength that has ever been reported for such edge emitting lasers is ~336 nm [199]. The poor performance of such devices is fundamentally limited by the presence of large densities of defects and dislocations, the strong polarization fields, and the inefficient p-doping in AlGaN materials (see Section 1.1.2). With potential advantages, including low defect density, much reduced strain-induced polarization fields, and significantly enhanced dopant incorporation, nanowires become a great candidate for UV laser application. However, the realization of efficient nanowire lasers in the UV wavelength range has been very limited. For practical applications, it is of significant interest in developing electrically injected edge emitting lasers by using such defect-free nanowire structures. To realize nanowire edge emitting lasers, any optical scattering loss related to variations of nanowire size, density, and spacing should be substantially reduced. Therefore, the epitaxial growth and structural properties of such nanowire arrays need to be carefully controlled and engineered. In the vapor-liquid-solid or spontaneous formation process, III-nitride nanowire arrays generally exhibit random distribution in position and a high degree of nonuniformity in size and height distribution. Such issues can be addressed by using the special technique, i.e.SAG. In this process, the nanowire formation and nucleation is directly controlled by the nanoscale apertures created on a substrate using the well-defined top-down process.

In parallel, we have also developed low threshold plasmonic Al(Ga)N nanostripe based laser in the deep UV spectral range. To date, the size reduction of photonic components down to nanometer scale, for example, nano-LEDs and nano-lasers, is highly desirable for on-chip communication and computation technologies. However, the diffraction limit of light when the dimensions of optical components approach the wavelength of light severely limits the fabrication process. One of the most promising methods to address these challenges is to utilize surface plasmons, which is able to confine light to very small dimensions at the interface of metal-dielectric [200]. To date, little attention has been paid to nano-/micro-scale plasmonic laser in DUV range which is mainly due to the bottleneck of achieving high quality Al-rich AlGaN nanostructure and metal layer, which limits surface plasmons coupling efficiency. In this context, we have investigated the MBE growth, fabrication, and characterization AlGaN stripe based plasmonic lasers. Devices under electrical injection have been realized. In addition, stripe plasmonic lasers will be demonstrated to achieve high output power. These laser arrays can be individually addressed and can be designed as suitable light sources for future high resolution projection systems.

Chapter 3: Demonstration of *p*-Type InN Nanowires

3.1. Introduction: Challenges of Direct Measurement of *p*-Type Conduction in InN

To date, the evidence and/or possibilities of *p*-type doping in InN has not been demonstrated prior to this thesis work. In previous studies, the hole mobility and concentration can only be estimated through indirect measurements [94, 131, 133, 201-206]. For example, ambipolar carrier diffusion in *n*-type InN films analyzed by time-resolved transient grating technique has shown hole mobility values of 39 and 26 $cm^2/V \cdot s$ near the surface of InN and the interface between InN and GaN buffer layers, respectively. Another hole mobility value of 50 cm^2/V s has been estimated in quantitative mobility spectrum analysis. Wang *et al.* reported hole mobility values of 17 – 36 $cm^2/V \cdot s$ for hole concentrations of 1.4 – 3.0 × 10^{18} cm^{-3} by a combination of electrolyte capacitance voltage (ECV) and sheet conductivity measurements on different thickness Mg-doped InN epilayers [207]. ECV combined with thermopower measurements have been very recently used to estimate hole mobility values of 15 – 66 $cm^2/V \cdot s$ and hole concentrations of 1.0 – 2.8 × 10^{18} cm^{-3}, respectively [133]. The highest theoretical hole mobility studied by ensemble Monte Carlo method reaches to 220 $cm^2/V \cdot s$ for very high quality InN, wherein the transport is limited by phonon scattering only. However, when sample quality was taken into account, the value was largely suppressed to 20 – 70 $cm^2/V \cdot s$ [135]. The extreme difficulties in the demonstration of p-type InN is largely due to the presence of electron accumulation layer on grown surfaces of InN epilayers, which greatly overwhelms *p*-type conduction and results in surface Fermi level pinning deep in the conduction band [201] as well as the formation of a surface inversion layer. A large downward band bending ~0.6 – 0.7 eV was experimentally observed, associated with donor-type

surface states density of ~ 2.5±0.2 × 10^{13} cm^{-2}, and a surface Fermi level (E_F) of about 1.6±0.1 eV above the valence band maximum (VBM, E_V) [208]. Essentially, such a Fermi level E_F pinning well above the conduction band minimum was commonly measured on both polar and non-polar planes in nominally non-doped and *n*-type InN which is theoretically considered to be an intrinsic property because of the high charge neutrality energy level and the low conduction band edge of InN [50, 209]. Recently, by using the first principles calculations, Segev and Van de Walle suggested that the microscopic origin of donor-type surface states leading to surface electron accumulation is mostly associated with In-In bonding states on the InN surfaces with In adlayers [57]. Furthermore, they theoretically predicted the surface Fermi level can be unpinned on reconstructed nonpolar InN surfaces [136] and it was only experimentally confirmed at the *in situ* cleaved non-polar surfaces [62]. Additionally, recent experiments suggested that the Fermi level could be possibly unpinned on polar planes [55, 210] which are in direct contrast to many theoretical predictions. Therefore, at present, it is of utmost importance for InN studies to eliminate the existence of accumulation layer at grown surfaces in order to pave the way for a direct detection of *p*-type conduction and high hole mobility.

The origin of the electron accumulation at the InN surfaces has been theoretically explained by the unusual position of branch point energy (also known as the Fermi stabilization energy or charge neutrality level) located high in the conduction band (~0.9 eV above conduction band edge) [211] and unintentionally doped impurities and native defects (nitrogen vacancy tend to be dominant donor-like defects in InN.). This explains the extreme *n*-type activity and difficulties of *p*-type doping in InN. Recently, by improving the MBE process significantly [43], intrinsic InN nanowires with the absence of electron accumulation on the non-polar grown surface (*m*-planes), have been achieved [121, 122]. A removal of surface electron accumulation by minimizing the

formation of surface defects during catalyst-free growth process together with utilizing an in situ deposited In seeding layer to enhance nucleation and nanowire formation, results in extremely low residual electron density, ~10^{13} – 10^{15} cm^{-3}. The progress has paved the way for the realization of *p*-type InN [137].

In the first Section of this Chapter, the observation of ambipolar transport characteristics of InN:Mg nanowires at room-temperature will be reported, providing unambiguous evidence that Fermi-level is fundamentally unpinned on the grown surfaces of InN. Such a behavior, however, is not measured in Si-doped InN nanowires, which is explained by Si-dopant surface segregation and the resulting electron accumulation. It is further suggested that defect and impurity incorporation on the grown surfaces of InN are the primary causes for the commonly measured electron accumulation and Fermi-level pinning.

In the second Section of this Chapter, the realization of electroluminescence emission of single InN *p-i-n* nanowire devices will be presented. Electroluminescence emission with a peak energy of 0.71 eV (1.75 μm) was observed at 77 K. The measurement of near-bandgap electroluminescence provides unambiguous evidence for the achievement of p-type conduction of InN.

3.2. Electrical Transport Properties of Single Mg-/Si-Doped Single InN Nanowires

3.2.1. Molecular Beam Epitaxial Growth of Mg-doped InN Nanowires

In this experiment, catalyst-free Mg-doped InN nanowires were grown on Si(111) substrate by RF-MBE under nitrogen-rich condition. Prior to loading into the MBE system, the Si substrates were chemically treated by standard solvent solutions and hydrofluoric acid. The surface oxide

was then thermally desorbed at ~675ºC. In contrast to conventional InN spontaneous growths under nitrogen-rich conditions, an *in situ* In seeding layer (thickness of ~6Å) was first deposited on Si substrate prior to introducing nitrogen [43, 120]. At elevated temperature, nanoscale droplets subsequently form, which subsequently promote the nucleation process of InN nanowires. The growth conditions for InN nanowires consist of: a substrate temperature of 478ºC, an In beam flux of ~6 $\times 10^{-8}$ Torr, a nitrogen flow rate of ~1.0 sccm (sccm denotes cubic centimeter per minute at STP), a radio frequency (RF) plasma forward power of ~350W and a growth duration of ~3 hours. Mg cell temperatures of 220ºC, 230°C (associated with Mg flux of ~4 $\times 10^{-10}$ Torr, ~ 9 $\times 10^{-9}$ Torr, respectively) and Si cell temperature of ~1300ºC for Mg-/Si-doped InN wires respectively. Under optimal growth conditions, the resulting InN nanowires exhibit non-tapered, nearly perfect hexagonal structure with identical top and bottom sizes shown in Figure 3-1. The secondary ion mass spectroscopy (SIMS) studies on Mg-doped InN epilayers grown by MBE with Mg cell temperatures of 220ºC and 230°C indicate that Mg doping concentrations are ~2.3 $\times 10^{19}$ and ~5.5 $\times 10^{19}$ cm^{-3}, respectively [133]. However, it is of importance to note that Mg doping concentration in nanowires may be lower than that in planar structures. The difficulties of Mg dopant incorporation in nanowires is mainly due to high Mg desorption rate on the nanowire surfaces at the growth temperature. Because of shadow effect of adjacent nanowires in the MBE growth process, the desorbed Mg atom cannot be compensated by impinging ones which does not occur during epilayer growth process even under similar growth conditions. In addition, the presence of natural donor defects is attributed to reduce the free hole density by compensating free holes. On the other hand, Si-doped nanowires with Si cell temperature of ~1300ºC corresponds to the approximately average doping concentration of ~10^{18} cm^{-3} measured by secondary ion mas spectroscopy [122].

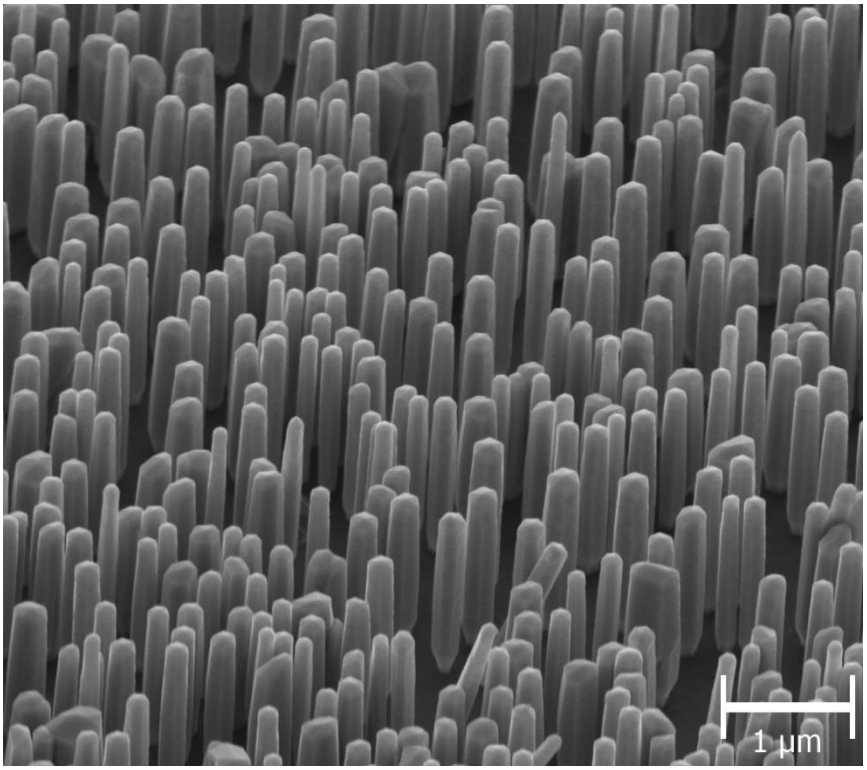

Figure 3-1: 45º-tilted SEM images of Mg-doped InN grown on Si (111) substrate with Mg cell temperature of 230 ºC.

3.2.2. Characterization and Discussion

InN nanowires with the separate incorporation of Mg and Si dopants were grown and studied. Given afore-described growth conditions, the resulting InN nanowires exhibit non-tapered, near-perfect hexagonal structure with approximately identical top and bottom sizes [43]. The nanowire orientation is along the *c*-axis [136], with the sidewalls being non-polar *m*-planes. Detailed transmission electron microscopy (TEM) analysis confirmed that the nanowires are of wurtzite crystal structure and nearly free of structural defects and misfit dislocations [43, 120, 121]. X-ray photoelectron spectroscopy (XPS) studies shown in Figure 3-2 confirm that, on the grown surfaces of such InN nanowire ensembles, the Fermi-level can vary from below the conduction band minimum (CBM) to well above the CBM [121, 137], depending on the dopant incorporation.

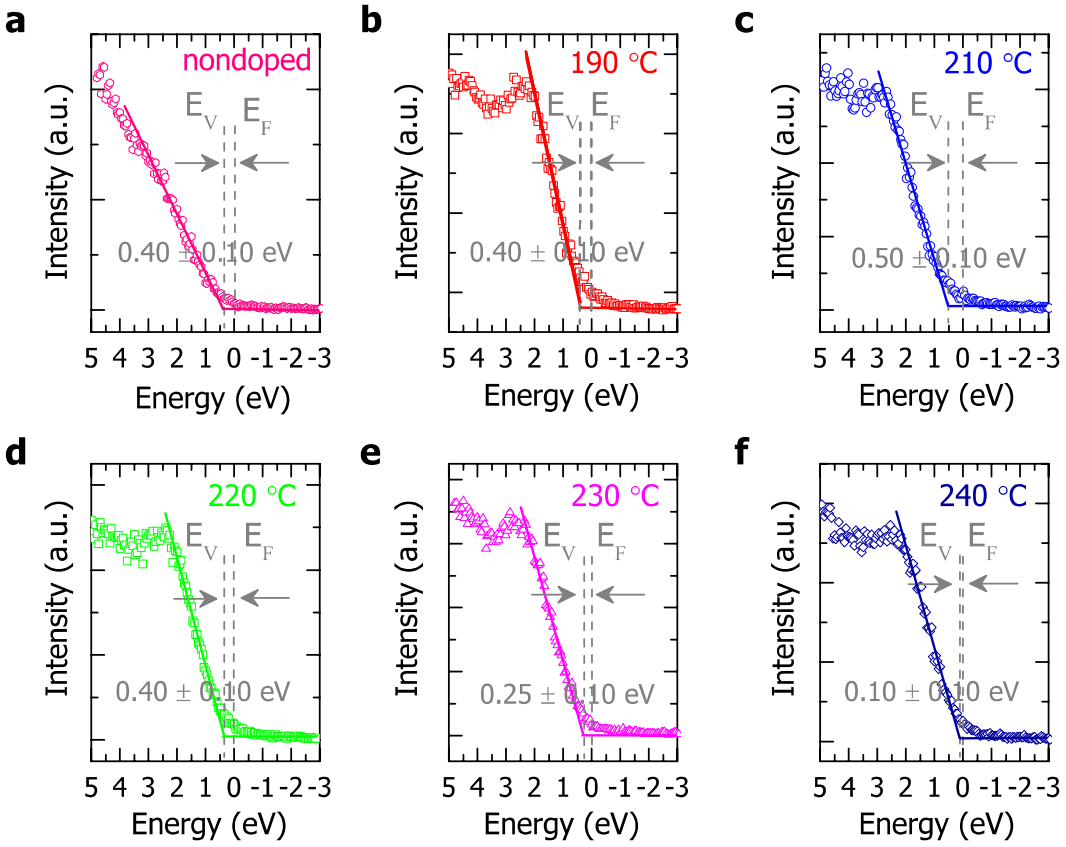

Figure 3-2: XPS studies of non-doped (a) and Mg-doped InN nanowires with different Mg doping concentrations, i.e. (b) – (f) correspond to Mg cell temperatures of 190°C – 240°C, respectively [137].

In this work, in order to study the impact of dopant incorporation on the charge carrier transport and surface properties, single nanowire field effect transistors (FET) were fabricated and characterized. First, as-grown InN nanowires were dispersed onto pre-patterned Si substrates using scratching approach, i.e. as-grown samples were placed face-to-face to substrate. As a result, Van der Waals force will hold the nanowires on the surface. In this experiment, pre-patterned substrates were coated with a dry thermal SiO_x dielectric layer (~100 nm) and the coordinate system on the substrate were made with standard photolithography, metallization processes with a coordinate system to locate nanowire position precisely during subsequent e-beam lithography process.

Subsequently, the nanowires were individually contacted by multilayer metal electrode (Ni/Au/Ni/Al/Ni/Au) using e-beam lithography and metallization techniques, followed by annealing at 400ºC in N_2 ambient. Single InN nanowire-based FET in a 3-terminal configuration is schematically shown in Figure 3-3a. Three metal contacts were carefully designed with the similar width of ~20-30 nm. In this work, we focus on two types of Mg-doped In nanowires, samples A and B, with corresponding Mg doping concentrations of ~10^{19} and 5×10^{19} cm^{-3}, respectively [133]. In addition, Si-doped InN nanowires (Sample C), with Si doping level ~10^{18} cm^{-3}, were also studied for comparison. An SEM image of a single nanowire transistor device is shown in Figure 3-3b.

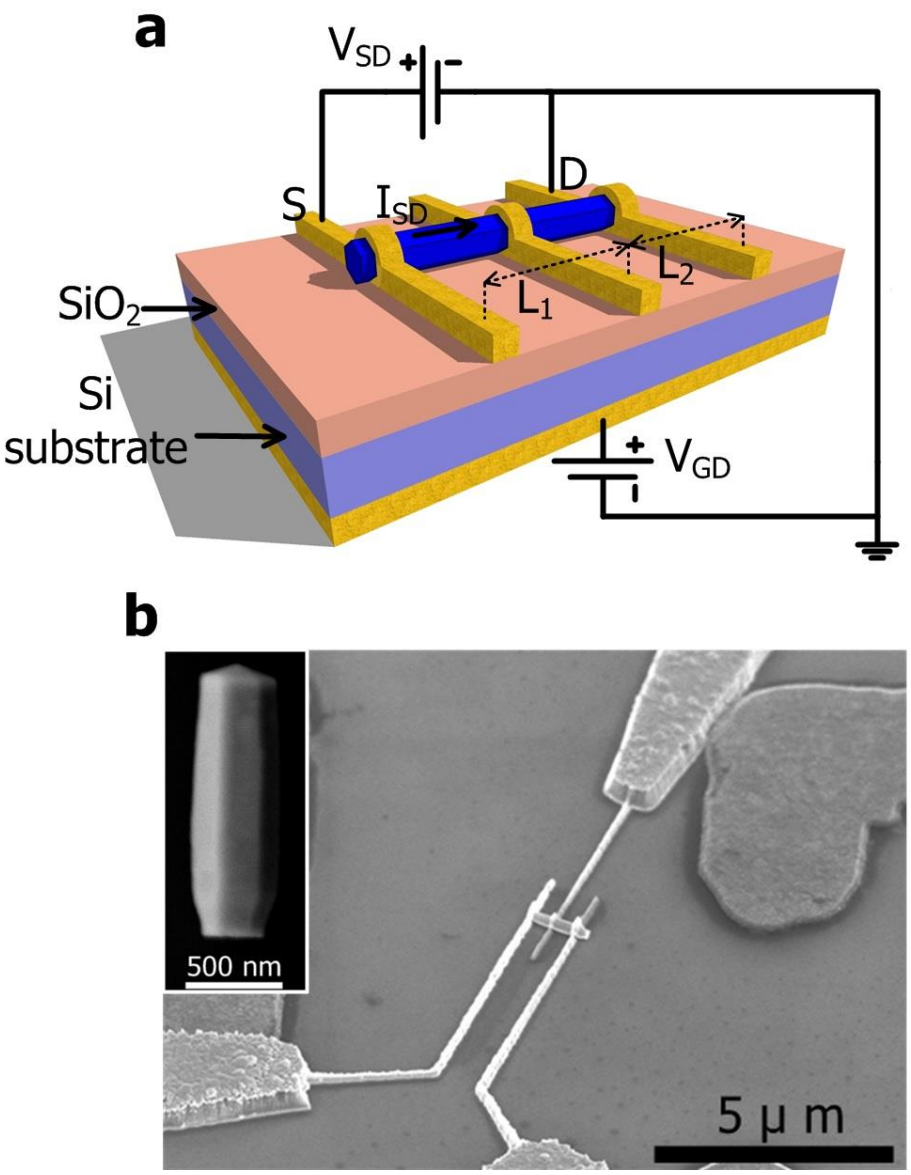

Figure 3-3: (a) A schematic plot of InN nanowire-based field effect transistor in the 3-terminal configuration, to derive metal-semiconductor contact resistance; (b) A SEM image of a single Mg-doped InN nanowire device. Inset: single Mg-doped InN dispersed onto pre-patterned substrate.

The devices were measured under a direct current bias in vacuum. The characterization of the moderately Mg-doped InN nanowire (sample A) is first described. The nanowire diameter is ~240 nm, with a length of ~1.3 μm. Shown in Figure 3-3a, the source-drain current I_{SD} increases linearly with source-drain voltage V_{SD}, indicating the Ohmic contact formation. Assuming that the

nanowire-metal contact resistance (R_C) is distributed equally for all 3 contacts, R_C was estimated from the 3-contact configuration, schematically shown in Figure 3-3a, by the following equation.

$$R_C = 0.5\,(R_T - (R_1 - R_2)(L_1 + L_2)/(L_1 - L_2)) \qquad \text{Eq.}\,(3-1)$$

where R_T is the resistance between the two outer contacts, and R_1 and R_2 are the resistance for segments L_1 and L_2, respectively. The contact resistance was estimated to be ~ 50% of the total resistance at zero gate voltage. Shown in Figure 3-4a, gate voltages V_{GD} from -1 V to 0.5 V modulate the nanowire resistance by field effect. With increasingly more negative back-gate voltage (V_{GD} < 0), the device conductance I_{SD}/V_{SD} is increased correspondingly, providing unambiguous evidence for *p*-type conduction in Mg-doped InN nanowires [212, 213]. The direct detection of *p*-type conduction by field effect in Mg-doped InN has been measured in more than five devices. Figure 3-4b illustrates the typical corresponding transfer characteristics I_{SD} as a function of V_{GD} at V_{SD} = 30 and 50 mV at room-temperature. At negative gate voltage V_{GD} < -0.8V, the nanowire current I_{SD} saturates which can be ascribed to the predominance of contact resistance over channel resistance. The minimum I_{SD} occurs at a small positive V_{GD} (~ 0.1 V), at which point the free holes are depleted completely. Interestingly, at V_{GD} > 0, the device shows evidence of electron transport by which I_{SD} increases as gate voltage V_{GD} increases. The valley formed by a minimum in device conductance as a function of gate voltage clearly indicates ambipolar transport characteristics of the Mg-doped InN nanowires. Such *p*-type conductance and ambipolar transport characteristics have also been observed in Mg doped InN nanowires with different diameters. This observation of ambipolar field effect characteristics provides clear evidence that the surface Fermi-level of Mg-doped InN nanowires is fundamentally unpinned, which is in agreement with previously reported XPS studies on ensemble InN nanowires [137]. The energy band diagram is schematically plotted in Figure 3-4c.

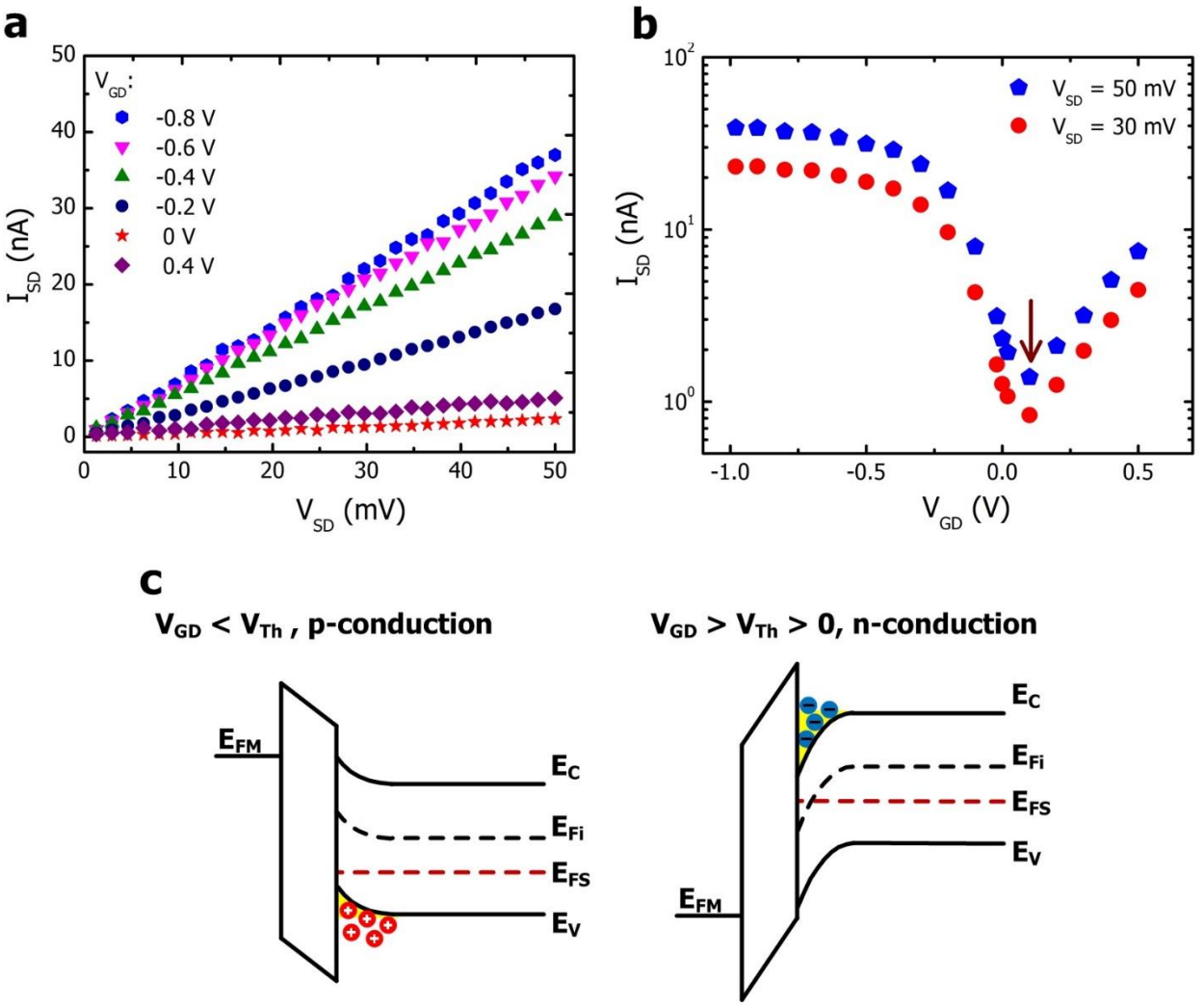

Figure 3-4: The FET characteristics of Mg-doped InN wires (sample A) at room temperature. (a) I_{SD}-V_{SD} characteristics. (b) I_{SD}-V_{GD} dependence under V_{SD} = 30 and 50 mV, indicating ambipolar transport. The arrow denotes the minimum I_{SD} position. (c) Schematic band diagrams showing carrier density on wire surfaces: hole accumulation layer at $V_{GD} < V_{Th}$ (left) and inversion layer at $V_{GD} > V_{Th} > 0$ (right).

The gate dependent hole concentration is derived using the metal-oxide-semiconductor field-effect transistor (MOSFET) model. The transconductance $g_m = \partial I_{SD}/\partial V_{GD}$ is determined from the best linear fit to channel current versus gate voltage. The field-effect mobility μ, in turn, is determined from the transconductance with the following equation:

$$\mu = \left(\frac{\mathrm{C}}{\mathrm{L}^2}\mathrm{V_{SD}}\right)^{-1} \left.\frac{\partial I_{SD}}{\partial V_{GD}}\right|_{\mathrm{V_{SD}}} \qquad \text{Eq. } (3-2)$$

Using the cylinder-on-plate model, the total capacitance *C* is given by [212],

$$C = \frac{2\pi\varepsilon\varepsilon_0 L}{cosh^{-1}(1 + t_{ox}/r)} \qquad \text{Eq. } (3-3)$$

where ε is the relative dielectric constant of SiO_2 and *L* is the distance between source and drain contacts, *r* is the radius of the nanowire, and t_{ox} is the thickness of the gate oxide. With t_{ox} = 100 nm, *r* = 120 nm, *L* = 1.3 μm and hole transconductance g_m^h = 0.0895 μS derived from the p-type conduction, the field-effect hole mobility, μ_h, is ~130 $cm^{-2}/V{\cdot}s$. The depletion of the nanowire at the pinch-off voltage (~0.1V) induces a charge *Q* that is related to the threshold gate voltage V_{Th} via the total capacitance $C = Q/V_{Th}$. In the ideal case, the induced charge *Q* corresponds to the two-dimensional (2D) charge density n_{2D} in the accumulation layer at the nanowire nonpolar surface:

$$Q = eAn_{2D}, \qquad \text{Eq. } (3-4)$$

where *A* is the nanowire surface area in contact with the gate oxide. The derived 2D hole concentration on the nanowire surface is ~5.3×10^{10} cm^{-2} at V_{GD} = 0 V. This value is smaller than that estimated from equivalent planar structures because the enhanced Mg adatom desorption at the elevated growth temperature outweighs dopant segregation for nanowires [137].

Compared to the hole transport, the transfer curve of sample A exhibits a small asymmetric I_{SD} - V_{GD} characteristics at positive gate voltages in the electron conductivity, which has been commonly observed in InAs nanowire, carbon nanotube and organic semiconductor-based FETs [209, 214-216]. The origin of the asymmetry may arise from a variety of effects, including the different metal-semiconductor contact resistances for hole injection into the channel and electron injection into the channel, as well as charge trapping at the SiO_2 dielectric layer that is typical of

back-gated FETs [216, 217]. The field effect electron mobility and concentration of ambipolar conduction are estimated to be ~50 $cm^2/V{\cdot}s$ and ~10^{10} cm^{-2}, respectively. The estimated electron mobility is smaller than the measured hole mobility in *p*-type InN nanowires, possibly because of impurity scattering [123] or suppression of electron conduction as a result of charge trapping at the SiO_2 surface which is commonly observed in other semiconductor FETs [216, 217]. Finally, the relatively low on/off current ratio is limited by the intrinsic conduction of narrow-bandgap InN nanowires. The estimated concentration of both intrinsic bulk electrons and holes is ~10^{15} cm^{-3}, and with an average field-effect mobility ~120±10 $cm^2/V{\cdot}s$ derived from measured devices, the intrinsic resistance of typical InN wires is estimated to be ~15 MΩ. The estimated off-state current of ~3.3 nA at a bias of V_{SD} = 50 mV is in good agreement with the measured value.

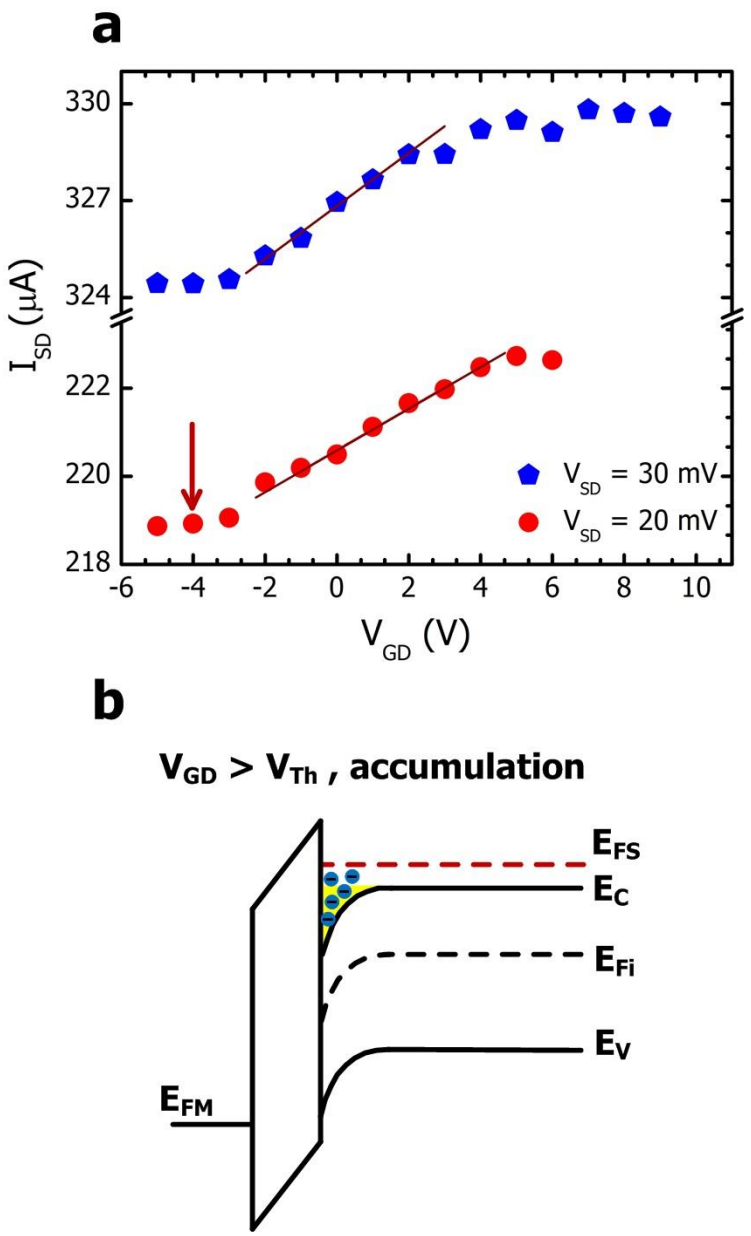

Figure 3-5: (a) Electrical transport of Si-doped InN nanowire-based FET (sample B) measured at room-temperature. I_{SD} as a function of V_{GD} at given V_{SD} of 20 and 30 mV. The arrow indicates threshold gate voltage V_{Th} and solid brown lines are linear fits. (b) Schematic band diagram showing the electron accumulation layer of Si-doped InN nanowire-based field effect transistors at $V_{GD} > V_{Th}$, indicating near surface Fermi level pinning deep in conduction band.

Unlike Mg-dopant, the surface desorption of Si atoms during the growth of InN nanowires is essentially negligible. Therefore, the surface charge properties of InN nanowires may be dominated by Si-donor segregation, which may lead to surface electron accumulation and Fermi-level pinning in the conduction band. In order to verify this effect, electrical transport properties of Si-doped InN nanowires were studied. Figure 3-5 illustrates the transfer characteristics of I_{SD} as a function of V_{GD} at V_{SD} = 20 and 30 mV. The increase in I_{SD} with increasing V_{GD} has been commonly observed in *n*-type nanowire FETs [53, 214]. From the measurements shown in Figure 3-5, an electron transconductance g_m^e of 0.808 μS was extracted at V_{SD} = 30 mV, resulting in mobility μ_n of ~2030 $cm^2/V{\cdot}s$. Unlike InN:Mg nanowire transistors wherein ambipolar conduction can be clearly measured, InN:Si nanowire transistors are dominated by electron conduction and the presence of holes is not measured over a large range of gate voltages. This suggests the presence of surface electron accumulation on Si-doped InN nanowires, schematically illustrated in Figure 3-5b. The derived n_{2D} was ~6×10^{12} cm^{-2}, which agrees with the downward surface band bending of the surface band and electron accumulation measured by XPS on such InN:Si nanowires in previous studies [121, 122]. It is therefore evident that the presence of surface electron accumulation and Fermi-level pinning of Si-doped InN nanowires can be explained by the donor surface segregation effect. The nonuniform dopant incorporation is further supported by XPS and photoluminescence studies of intrinsic and Si-doped InN nanowires [121, 122].

Previous studies have shown the energy for the formation of various defects, including nitrogen vacancies, is also significantly smaller in the near-surface region of InN than in the bulk region [50, 121, 208]. Such defects generally serve as donors because of the extremely large electron affinity of InN [50, 56]. Therefore, the enhanced donor incorporation in the near-surface

region of InN, caused by either dopant (Si) segregation or defect formation, explains the commonly measured Fermi-level pinning and electron accumulation of the grown surfaces of InN.

3.3.The realization of electroluminescence of *p-i-n* InN nanowires

In the previous Section, it is demonstrated, for the first time, that *p*-type InN nanowires can be realized by direct Mg doping. The presence of *p*-type conduction was clearly measured from nanowire field effect transistors.

In the second Section of this chapter, we report on the achievement of electroluminescence emission of single InN *p-i-n* nanowire devices. InN *p-i-n* nanowire structures were grown directly on Si substrate by the MBE system and subsequently transferred to foreign substrate for the fabrication of single nanowire light emitting diodes. Electroluminescence emission with a peak energy of 0.71 eV (1.75μm) was observed at 77 K. The measurement of near-bandgap electroluminescence provides unambiguous evidence for the achievement of p-type conduction of InN.

In this experiment, the nanowire structure consists of 0.7 μm InN:Si, 0.2 μm non-doped InN, and 0.7 μm InN:Mg layers, schematically shown in Figure 3-6a. The growth conditions for *p-i-n* InN nanowires included a substrate temperature of 480°C, an In beam equivalent pressure of ~6×10^{-8} Torr, a nitrogen flow rate of 1.0 sccm, and a plasma forward power of 350 W. The Si and Mg cell temperatures were 1250°C and 240°C, respectively. The Si and Mg dopant concentrations in equivalent planar structures are estimated to be ~5×10^{17} cm^{-3} and ~9.5×10^{19} cm^{-3} based on secondary ion mass spectroscopy analysis, respectively [122, 218, 219]. However, the dopant concentration in nanowire structures may vary, due to the non-planar growth process. Shown in Figure 3-6b is a typical 45°-tilted SEM image of *p-i-n* InN nanowires grown on Si (111) substrate. The wire length is around 1.6 μm and the diameters vary from 200 to 500 nm. As seen, the InN

nanowires exhibit non-tapered surface morphology with a nearly perfect hexagonal structure. Detailed TEM studies further confirm that such wires are nearly free of structural defects such as stacking faults and misfit dislocations [43, 137].

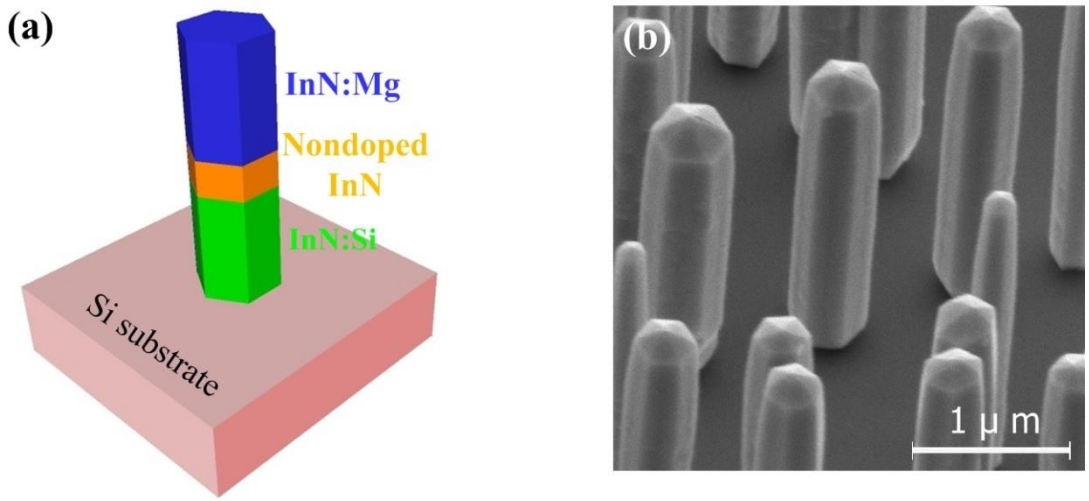

Figure 3-6: (a) Schematic plot of *p-i-n* InN nanowire structure grown on Si (111) substrate. (b) An SEM image of as-grown *p-i-n* InN nanowires on Si (111) substrate taken with a 45º angle.

Optical properties of the as-grown InN nanowire *p-i-n* structures on Si were first studied using temperature variable micro-photoluminescence (μ-PL) spectroscopy. The nanowire was optically excited using a semiconductor laser diode (λ = 635 nm) with a 100× objective lens, with a defocused beam size of ~5 μm^2. The emission was collected and analyzed by a high resolution spectrometer equipped with a liquid nitrogen (N_2) cooled InGaAs photodetector with lock-in amplification. The detector has a cut-off wavelength of 2.2 μm. Illustrated in Figure 3-7 is the PL spectrum (solid brown curve) of InN *p-i-n* structure measured at 77 K under an excitation power of 8 mW. The PL spectra of nominally non-doped, Si-doped (Si cell temperature of 1250°C), and Mg-doped (Mg cell temperature of 210°C) InN nanowires grown on Si substrate measured under similar conditions are also shown for comparison. For the non-doped InN nanowires, the PL peak

energy is ~0.69 eV, which is consistent with the band-to-band transition of InN under high excitation conditions [122]. For the Mg-doped InN nanowires with relatively high dopant incorporation, the PL peak energy is measured at ~0.59 eV, which corresponds to the Mg acceptor energy level(s) related transitions [219]. With the incorporation of Si dopant, the PL peak energy of InN is measured at ~ 0.74 eV. The blueshift compared to the PL emission of non-doped InN nanowires is attributed to the Burstein-Moss effect commonly measured in *n*-type degenerate InN nanowires and thin films [43, 122]. The PL peak energy of ~0.71 eV measured from the InN nanowire *p-i-n* structures thus can be ascribed to the emission largely from the non-doped as well as the Si-doped region.

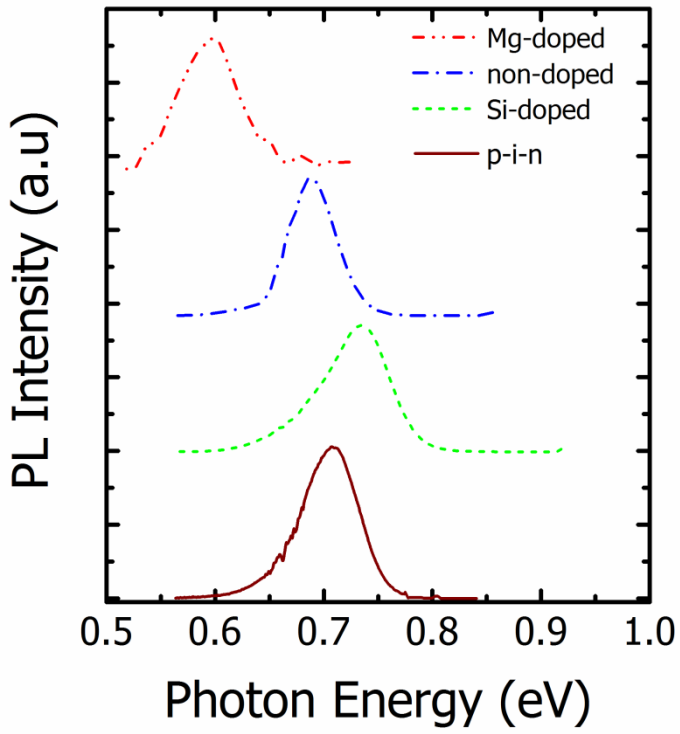

Figure 3-7: The PL spectrum of a single *p-i-n* InN wire measured at 77 K under 8 mW excitation. Also shown in the figure are the normalized PL spectra of non-doped and Si-/Mg-doped InN nanowires grown on Si substrate with Si and Mg cell temperatures of 1250°C and 210°C, respectively.

Subsequently, single InN nanowire-based LED devices were fabricated. As grown *p*-*i*-*n* InN nanowires were first dispersed onto pre-patterned, SiO_2 coated Si substrate. Ni/Au Metal contacts were then deposited on the *p*- and *n*-InN segments by standard e-beam lithography, thermal evaporation, and liftoff process, followed by rapid thermal annealing at 400ºC in N_2 ambient. Prior to metal deposition, the nanowire surface was cleaned in hydrochloric acid for 30 s. Schematic plot and scanning electron microscope image of a single *p*-*i*-*n* InN nanowire-based LED in a 2-terminal configuration are shown in Figures. 3-8a and b, respectively. Current voltage (I-V) characteristics of such single InN nanowire-based device were measured at 77 K in vacuum, clearly showing rectification characteristics, illustrated in Figure 3-8c. The measured currents at applied voltages of -0.5 V and +0.5 are -0.83μA and 3.5μA, respectively. The non-negligible current under reverse bias is largely related to the surface recombination and leakage, due to the presence of surface states/defects and the lateral growth of InN:Mg surrounding the entire nanowire structures.

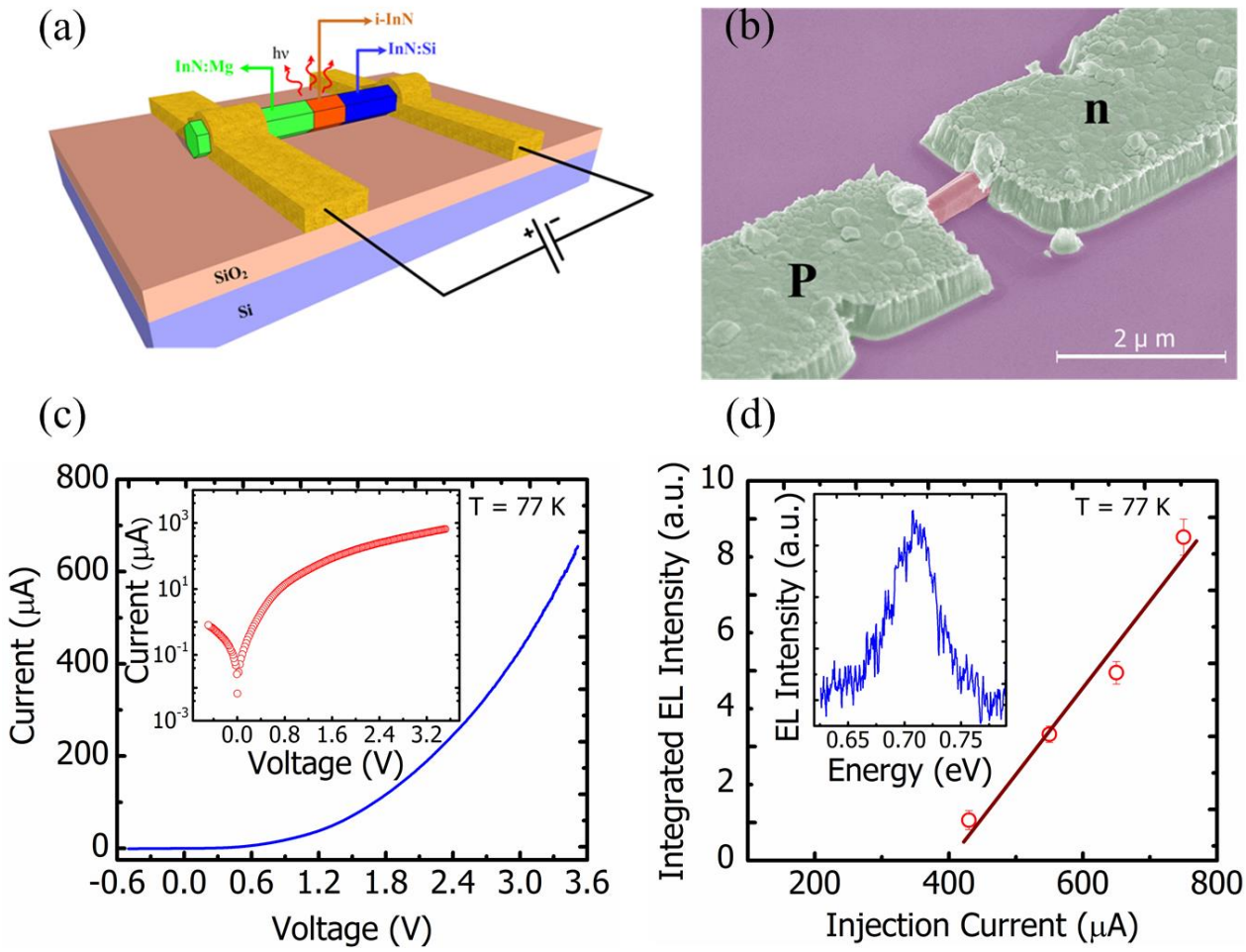

Figure 3-8: (a) Schematic illustration of single InN *p-i-n* nanowire LED on Si substrate. (b) An SEM image of the fabricated single *p-i-n* InN LED. (c) I-V characteristics measured at 77 K of single InN nanowire-based LED device. Inset: I-V characteristics of the device under forward and reverse bias in semi-log scale. (d) Integrated EL intensity as a function of injection current measured at 77 K. Inset: electroluminescence spectra measured at 750 μA.

Electroluminescence emission was subsequently measured. The single nanowire devices were biased under continuous wave (CW) conditions at 77 K. Electroluminescence emission was collected through a 100× objective lens and then directed to a high resolution spectrometer equipped with a liquid nitrogen (N_2) cooled InGaAs photodetector with lock-in amplification. Shown in the inset of Figure 3-8d, electroluminescence emission can be clearly observed. The

peak energy is 0.71 eV, corresponding to a wavelength of 1.75 μm, which is in agreement with the photoluminescence emission measured from the as grown InN nanowires on Si, shown in Figure 3-7. The spectral linewidth is ~120 nm. From the Einstein relation, the diffusion coefficient (D) for electrons and holes is given by following equations:

$$D_e = \mu_e \frac{\mathrm{kT}}{\mathrm{e}} \qquad \text{Eq. (3−5)}$$

$$D_h = \mu_h \frac{\mathrm{kT}}{\mathrm{q}} \qquad \text{Eq. (3−6)}$$

With hole mobility μ_h ~100 $cm^2/V{\cdot}s$ (ref. 137) and electron mobility μ_e ~1000 $cm^2/V{\cdot}s$ [116], the diffusion coefficients for holes and electrons at 300 K are derived to be D_h ~2.585 cm^2/s and D_e ~25.85 cm^2/s, respectively. The carrier diffusion length $L = \sqrt{D * \tau}$, wherein τ is the carrier lifetime, for holes and electrons are ~508 nm and ~1.6 μm, respectively. Given the relatively small diameters (~400 nm) of InN nanowires, the current density is estimated to be $J = 3.1 \times 10^5$ A/cm^2, which is rather high. At this injection current, the carrier density (N) is derived by the following equation,

$$N = \frac{\tau J}{qL} \qquad \text{Eq. (3−7)}$$

wherein L is the minority carrier diffusion length, and τ is the carrier lifetime (~0.5 ns). The carrier density is estimated to be in the range of 10^{19} cm^{-3}. Previous studies have confirmed that, for such high carrier concentrations, the Fermi-level is shifted above the conduction band edge, leading to luminescence emission peaks in the range of 0.7 to 0.8 eV, which is consistent with our measured results [120, 122]. Variations of the integrated light intensity vs. injection current are shown in Figure 3-8d. It is seen that the electroluminescence intensity increases near-linearly with injection current. The device performance can be further improved by employing InN/InGaN core-shell nanowire structures to provide strong carrier confinement and thus reduce nonradiative surface

recombination [140]. The realization of electroluminescence emission from InN *p-i-n* nanowire structures provide unambiguous evidence for the *p*-type conduction of InN and further suggests the absence of surface electron accumulation on the grown surfaces on InN, which are in excellent agreement with recent studies [137, 139].

3.4. Conclusion

In summary, we have addressed two critical challenges of InN, including p-type conduction and electroluminescence emission. The presence of ambipolar characteristics in InN:Mg nanowires confirms that Fermi-level pinning is *not* an intrinsic property of the InN grown surfaces. It is further suggested that defect and impurity incorporation on the grown surfaces of InN is the primary causes for the commonly measured electron accumulation and Fermi-level pinning. Secondly, we have fabricated InN *p-i-n* nanowire LEDs, and near-bandedge electroluminescence emission was clearly measured. The measurement of near-bandgap electroluminescence provides unambiguous evidence for the achievement of *p*-type conduction of InN. The realization of functional InN nanowire devices will significantly advance the development of InN-based nanoscale optoelectronic devices and integrated photonic circuits on Si platform for the emerging chip-level optical communications.

Chapter 4: Ultraviolet GaN/AlGaN Light Emitting Diodes Operating at 279 nm by Selective Area Epitaxial Growth

4.1. Introduction

Light emitting diodes with emission wavelengths in the ultraviolet spectral region (200-365 nm) have been developed using Al(In)GaN based semiconductors. They are of tremendous importance for a wide range of applications in lighting, display, air-water purification, disinfection, chemical and biochemical sensors, and white-light generation via phosphor excitation [65-67]. To date, however, the performance of such devices degrades considerably with increasing Al content, i.e. decreasing operation wavelength [70-72]. For example, the currently reported maximum light output powers for AlGaN MQW DUV LEDs for the peak wavelengths of 241 nm, 256 nm and 284 nm are 1.1 mW, 4.0 mW and 10.6 mW, respectively [71]. The highest reported EQE of 281 nm and 279 nm emission are 3.45% and 7%, respectively [73-75]. The poor performance of such devices is fundamentally limited by the presence of large densities of defects and dislocations, the strong polarization fields, and the inefficient *p*-doping in $A_xlGa_{1-x}N$ materials. Recently, with the use of nanowire structures, high efficiency LEDs have been demonstrated in the visible range [140, 141]. Nanowire structures can offer several fundamental advantages, including low defect densities, much reduced strain-induced polarization fields, and significantly enhanced dopant incorporation. However, the realization of efficient nanowire LEDs operating in the DUV wavelength range has been very limited. To realize high efficiency $A_xlGa_{1-x}N$ nanowire LEDs, any optical scattering loss related to variations of nanowire size, density, and spacing should be substantially reduced. Therefore, the epitaxial growth and structural properties of such nanowire arrays need to be carefully controlled and engineered. In the VLS or spontaneous formation

process, III-nitride nanowire arrays generally exhibit random distribution in position and a high degree of non-uniformity in size and height distribution [144, 220-223]. Such issues can be largely addressed by using the special technique of selective area epitaxial growth [193, 194]. In this process, the nanowire formation and nucleation is directly controlled by the nanoscale apertures created on a substrate using the well-defined top-down process. To date, however, $A_xlGa_{1-x}N$ based nanowire DUV LEDs with the SAG process have not been demonstrated. In addition, the direct formation of high quality $A_xlGa_{1-x}N$ nanowires by this growth process has remained elusive. In this work, we have performed a detailed investigation of the selective area growth of large area GaN/AlGaN nanowire arrays on *n*–GaN template on *c*–plane sapphire substrate. Such nanowire structures exhibit highly uniform diameter distribution and strong photoluminescence emission in the wavelength range of ~280 nm. The nanowire UV LED devices exhibit high internal quantum efficiency (IQE) of ~ 45% at 280 nm.

4.2. $Al_xGa_{1-x}N$ Nanowire Arrays by Selective Area Epitaxial Growth

Illustrated in Figure 4-1 is the selective area epitaxial growth of GaN/AlGaN nanowire arrays which takes place on two-dimensional GaN template on *c*–plane sapphire substrate by employing a thin Ti layer (~10 nm) as the growth mask. Nanoscale hexagonal patterns with a lateral size *d* of ~250 nm and a center-to-center lattice spacing *a* of ~400 nm arranged in a triangular lattice were created using standard e–beam lithography and reactive ion etching techniques. Sizes of the nanohole arrays were varied in the range of tens and hundreds of μm for the fabrication of large area nanowire based LED structure. Two metal layers consist of 1 μm Mo and 500 nm Ti were deposited on the back surface of the sapphire substrate for a uniform and efficient heat transfer from the heater to substrate. Prior to loading into the growth chamber, the patterns were carefully cleaned by standard solvents. The Ti layer was then nitridized in the reaction chamber at ~400ºC

to prevent crack and degradation during the growth process [186, 224]. Subsequently, vertically aligned GaN/$Al_xGa_{1-x}N$ nanowire arrays were grown using Veeco Genxplore plasma–assisted molecular beam epitaxial system [225]. The growth condition will be described in the subsequent section.

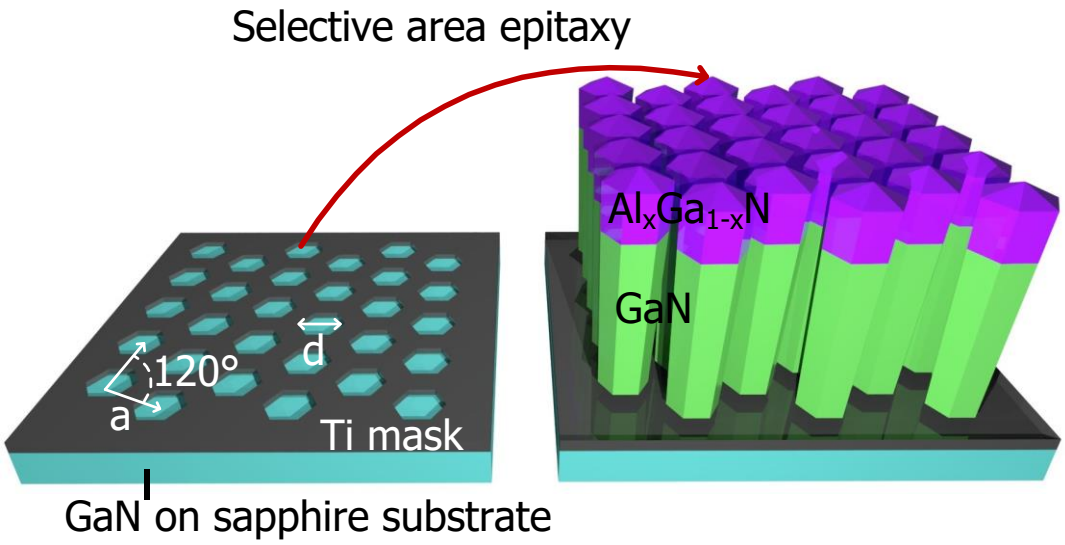

Figure 4-1: Left: Nanoscale hole arrays defined by typical electron beam lithography process on 10 nm Ti mask on planar GaN template on *c*-plane sapphire substrates. Right: Schematic of the selective area epitaxy of GaN/AlGaN nanowire arrays on 2D GaN template on *c*–plane sapphire substrate.

Shown in Figure 4-2 is a SEM image of GaN/AlGaN nanowire arrays selectively grown in the opening apertures, exhibiting a well-defined hexagonal morphology. It is also seen that the nanowires exhibit a very high degree of size uniformity and are vertically aligned along *c*-axis. Each nanowire has a well-defined pyramid top with sixfold side facets, assigned to be semipolar crystal planes.

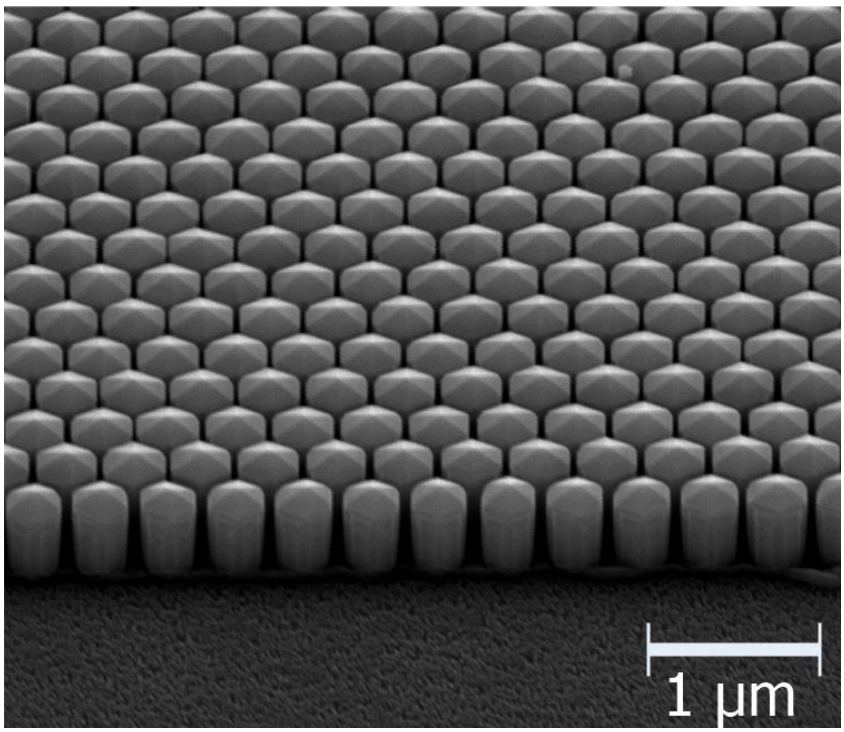

Figure 4-2: A 45°-tilted angle SEM image showing GaN/AlGaN nanowire arrays selectively grown in the opening apertures.

As an excellent method of controlling position, size and orientation of nanowires, SAG of (Al)GaN has been extensively developed using both metal-organic chemical vapor deposition (MOCVD) and MBE techniques with various mask materials (SiN_x, SiO2, Ti,) [182, 183, 185, 226]. However, short diffusion length of Al adatoms in the presence of nitrogen severely results in non-controllable spontaneous nucleation of $A_xlGa_{1-x}N$ nanowires on Ti mask surface. As a consequence, SAG of AlGaN nanowires at the openings with increasing Al composition has not been possible [195]. To date, there have been no reports of AlGaN nanowires grown by selective area epitaxy emitting at wavelengths shorter than 290 nm. In this regard, we have performed a detailed investigation of the selective area growth of large area GaN/AlGaN nanowire arrays on 2D GaN template grown on *c*-plane sapphire substrate with varied Al composition x_{Al}. Such nanowire structures exhibit strong PL emission in the ultraviolet C (UV-C) (< 280 nm), ultraviolet B (UV-B) (280 nm – 320 nm) and

ultraviolet AII (UV-AII) (~320 nm – 340 nm) bands. Photoluminescence spectra of AlGaN nanowire arrays were measured at room-temperature under excitation using a 193 nm ArF_2 excimer laser (pulse width: 8 ns and repetition rate: 470 Hz). The emitted light was collected and spectrally resolved by a high-resolution spectrometer and detected by a liquid nitrogen cooled charge coupled device (CCD). Shown in Figure 4-3, single-speak PL spectra of $A_xlGa_{1-x}N$ nanowire arrays were tuned from ~210 nm to ~327 nm, corresponding to Al composition (x_{Al}) from ~1 to ~0.2. The Al composition x_{Al} of $Al_xGa_{1-x}N$ nanowires can be estimated by the following equation[195]

$$E_g = 6.015x + 3.39(1-x) - 0.98x(1-x) \qquad \text{Eq. (4−1)}$$

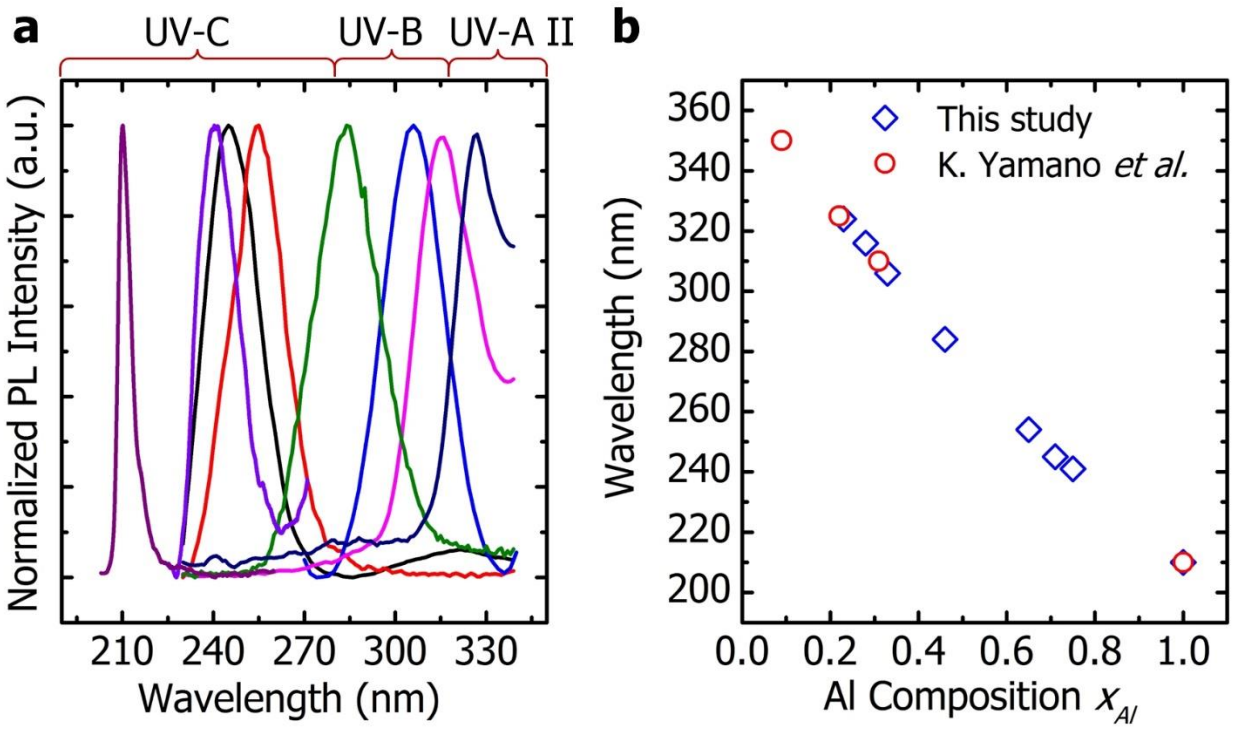

Figure 4-3: (a) Tunable photoluminescence spectra of $Al_xGa_{1-x}N$ nanowire arrays measured at room-temperature under excitation power of ~ 50 mW; (b) $Al_xGa_{1-x}N$ peak wavelength as a function of Al composition x_{Al}.

As can be seen from Figure 4-3, the PL peak emission wavelength decreases linearly with increasing x_{Al}, covering the entire UV spectral range including UV-AII, UV-B and UV-C, which was not possible in previous studies [195]. There are several factors that limit the tunability of the wavelength emission of SAG $Al_xGa_{1-x}N$ nanowire arrays especially in DUV range. The first major challenge is associated with growth temperature. Compared to conventional spontaneous $Al_xGa_{1-x}N$ nanowires grown by MBE technique, the nanowires grown by SAG technique are extremely sensitive to growth temperature variation, which is typically above 900°C. The high growth temperature is crucial to achieve $Al_xGa_{1-x}N$ with higher crystal quality. However, the high temperature will lead to desorption of GaN nanowire templates. The primary driving force for the selective nucleation of III-nitride nanowires is the difference in Al/Ga/In sticking coefficients between the mask and the openings. If a relatively low growth temperature is used, $Al_xGa_{1-x}N$ also forms on the mask and therefore reduces the growth selectivity as shown in Figure 4-4 [195, 227].

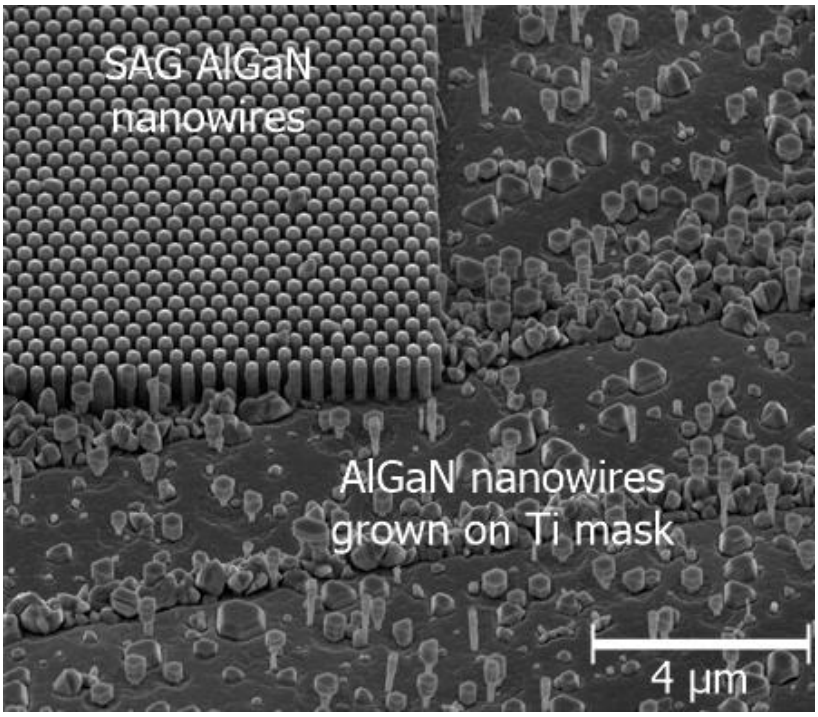

Figure 4-4: A SEM image of AlGaN nanowires grown both in openings and on Ti mask, indicating low growth selectivity.

4.3. Demonstration of Deep Ultraviolet $Al_xGa_{1-x}N$ Nanowire LEDs Operating at 279 nm by Selective Area Epitaxial Growth

4.3.1. $Al_xGa_{1-x}N$ Grown by Selective Area Epitaxy

The realization of tunable wavelength emission of AlGaN nanowire arrays grown by SAG technique provides a distinct opportunity to demonstrate LEDs operating in the DUV wavelength range. Illustrated in Figure 4-5 is the schematic diagram of AlGaN double heterostructure (DH) nanowires grown on *c*-plane sapphire substrate, which consists of a 400-nm Si-doped GaN, 70-nm Si-doped $Al_{0.6}Ga_{0.4}N$, 30-nm undoped $Al_{0.48}Ga_{0.52}N$ active region, and 70-nm Mg-doped $Al_{0.6}Ga_{0.4}N$ segment. The growth conditions for GaN/AlGaN DH nanowires included the following steps. *n*-Type GaN nanowire arrays were first grown with a substrate temperature of 955°C, nitrogen flow rate of 0.55 sccm, and Ga flux of ~3.71×10^{-7} Torr. Subsequently, the *n*- and *p*-type AlxGa1-xN cladding layers were grown at substrate temperature of 1025°C, and Ga and Al beam fluxes of ~3.71×10^{-7} Torr and ~3.73×10^{-8} Torr, respectively. The *i*-$Al_yGa_{1-y}N$ active layer sandwiched between the *n* and *p*-type cladding layers was grown with a nitrogen flow rate of 0.55 sccm, substrate temperature of 1025°C, Ga and Al beam fluxes of ~3.71×10^{-7} Torr and ~2.99×10^{-8} Torr, respectively. The substrate temperature mentioned here refers to the thermocouple reading on the backside of the substrate. The real substrate surface temperature is approximately ~100 – 150°C lower, depending on the substrate and sample size. Mg beam equivalent pressure was ~3.2×10^{-9} Torr for the Mg-doped AlGaN layer. During the growth of AlGaN nanowire segments, the lateral growth is significantly enhanced, leading to increased nanowire diameter and very small air gap amongst nanowires. The approximate axial and lateral growth rates are in range of ~3.5 nm/min and ~1 nm/min, respectively. Shown in Figure 4-5b is the SEM image of the nanowire arrays taken with a 45°-angle.

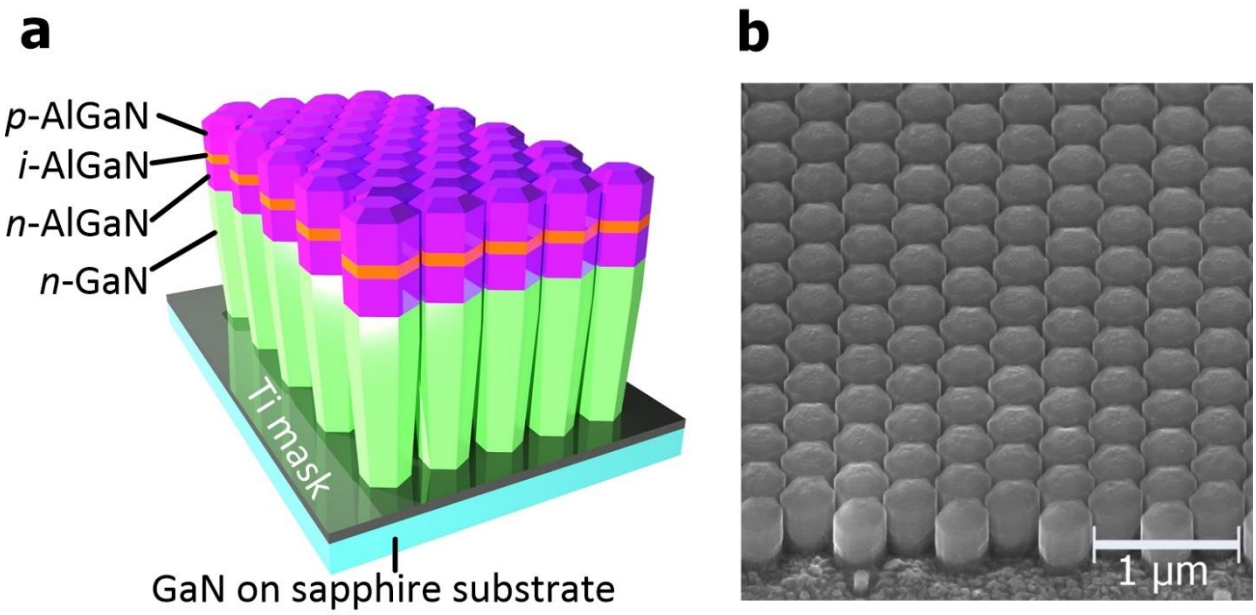

Figure 4-5: (a) Schematic diagram of AlGaN DH nanowire based LED structure. (b) A SEM image of AlGaN DH nanowires taken under 45°-tilted angle.

4.3.2. Characterization

Detailed structural characterization was further performed by an aberration-corrected FEI Titan Cubed 80-300 scanning transmission electron microscope (STEM) operated at 200 kV on a cross-sectional TEM specimen of the nanowire arrays prepared by focused ion beam (FIB) milling using a Zeiss NVision 40 dual-beam system with deposited Pt and C as protection layers as shown in Figure 4-6.

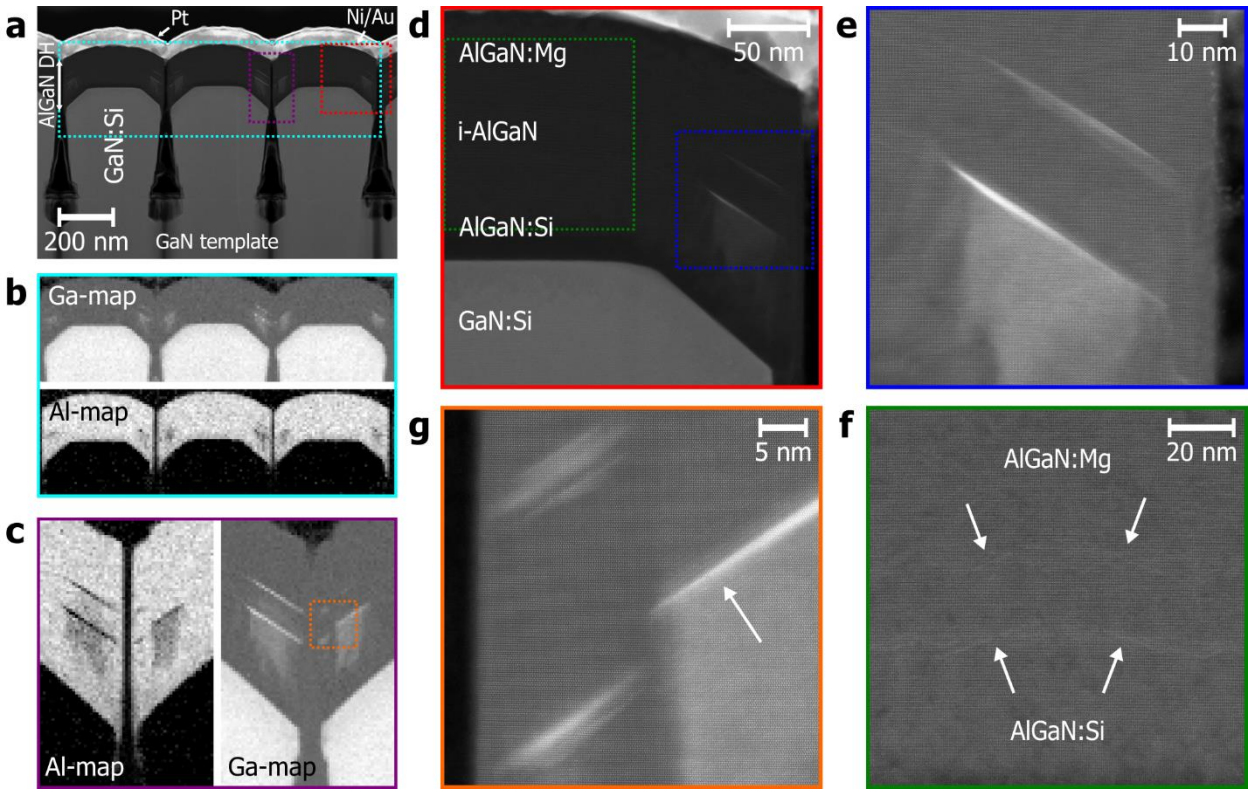

Figure 4-6: (S)TEM studies. (a) STEM-HAADF image of an array of non-coalesced AlGaN nanowires in cross-section along $\{11\bar{2}0\}$ zone-axis, showing the prismatic nature at the sidewalls and c-plane tendencies at the nanowire center. (b, c) Elemental maps from STEM-EELS showing the variations in Ga and Al elemental distribution within the AlGaN heterostructure and the *n*-GaN nanowire template. (d) Detailed image of the AlGaN heterostructure from boxed region in (a). (e, f, g) High-magnification images of the interfacial regions within the AlGaN heterostructure from boxed region in (d) and (c).

Atomic-number sensitive (Z-contrast) high-angle annular dark-field (HAADF) image of an array of AlGaN LED heterostructure nanowires observed in cross-section along the *a*-plane orientation is shown in Figure 4-6a. The brighter intensity regions correspond to the *n*-GaN nanowire template and the darker intensity AlGaN LED heterostructure. Electron energy-loss spectroscopy (EELS) was also carried out for elemental mapping of the AlGaN heterostructure in Figure 4-6b to understand its formation. No distinct continuous layer of changing Ga and Al

distribution was observed that would suggest a lower Al-concentration in the active layer between higher Al-concentration cladding layers, except for the near-surface regions of the nanowires. Further elemental mapping of the AlGaN heterostructure at the near-surface regions in Figure 4-6c details the enrichment of Ga (and corresponding deficiency in Al) along semi-polar interfaces within the AlGaN heterostructure and within the *n*-AlGaN region. A detailed examination was further investigated by atomically-resolved STEM images taken at different boxed regions (red, blue, and orange) corresponding to Figures 4-6d, 4-6e, and 4-6g, respectively. High-magnification view of the AlGaN heterostructure in Figure 4-6d (from the red-boxed region in Figure 4-6a), and other detailed views from different boxed regions at the near-surface region (blue) and nanowire center (green) are also presented in Figures 4-6e and 4-6f, respectively. Seen in Figure 4-6e, the Ga-rich interfaces lie along semi-polar $\{1\bar{1}03\}$ planes near the nanowire sidewalls, but transitions towards higher-order $\{1\bar{1}04\}$ plane closer to the nanowire center. At the center of the nanowire, various *p*-*i*-*n* AlGaN interfaces are not flat along *c*-plane, as expected from the termination of the *n*-GaN nanowire template shown in Figure 4-6d. The Ga-enrichment is minor towards the nanowire center in Figure 4-5f, but they mark zig-zag nano-facets identified as $\{1\bar{1}04\}$ planes, as arrowed along the plane normal. Some minor image intensity modulations also exist along the $\langle 1\bar{1}03 \rangle$ directions arrowed within the Ga-rich *n*-AlGaN region in Figure 4-6g, attributed to chemical ordering observed in similar AlGaN SAG nanowires [225] and spontaneously-formed AlGaN nanowires [228].

Optical properties of the AlGaN DH nanowire LED structures were subsequently studied by using temperature-dependent PL spectroscopy associated with a closed-loop liquid helium compressor. Illustrated in Figure 4-7a is the normalized PL spectra measured at room-temperature

at different excitation powers. At a very low excitation power, i.e., of 4mW, PL emission from active region $Al_{0.48}Ga_{0.52}N$ with a peak at ~283 nm dominates, which is attributed to an effective carrier confinement in the active region. With increasing excitation power, a shorter wavelength ~255 nm peak corresponding to higher Al composition $Al_{0.6}Ga_{0.4}N$ cladding layers is more pronounced. Meanwhile the longer wavelength peak emission ~340 nm likely origins from related-defect radiative recombination in doped AlGaN segments which has been commonly observed in AlGaN MQW UV LEDs. It is also seen that, with increasing excitation power, the emission peak E_1 (~283 nm) becomes broader and exhibit highly stable luminescence characteristics with negligible shifts, shown in Figure 4-7b.

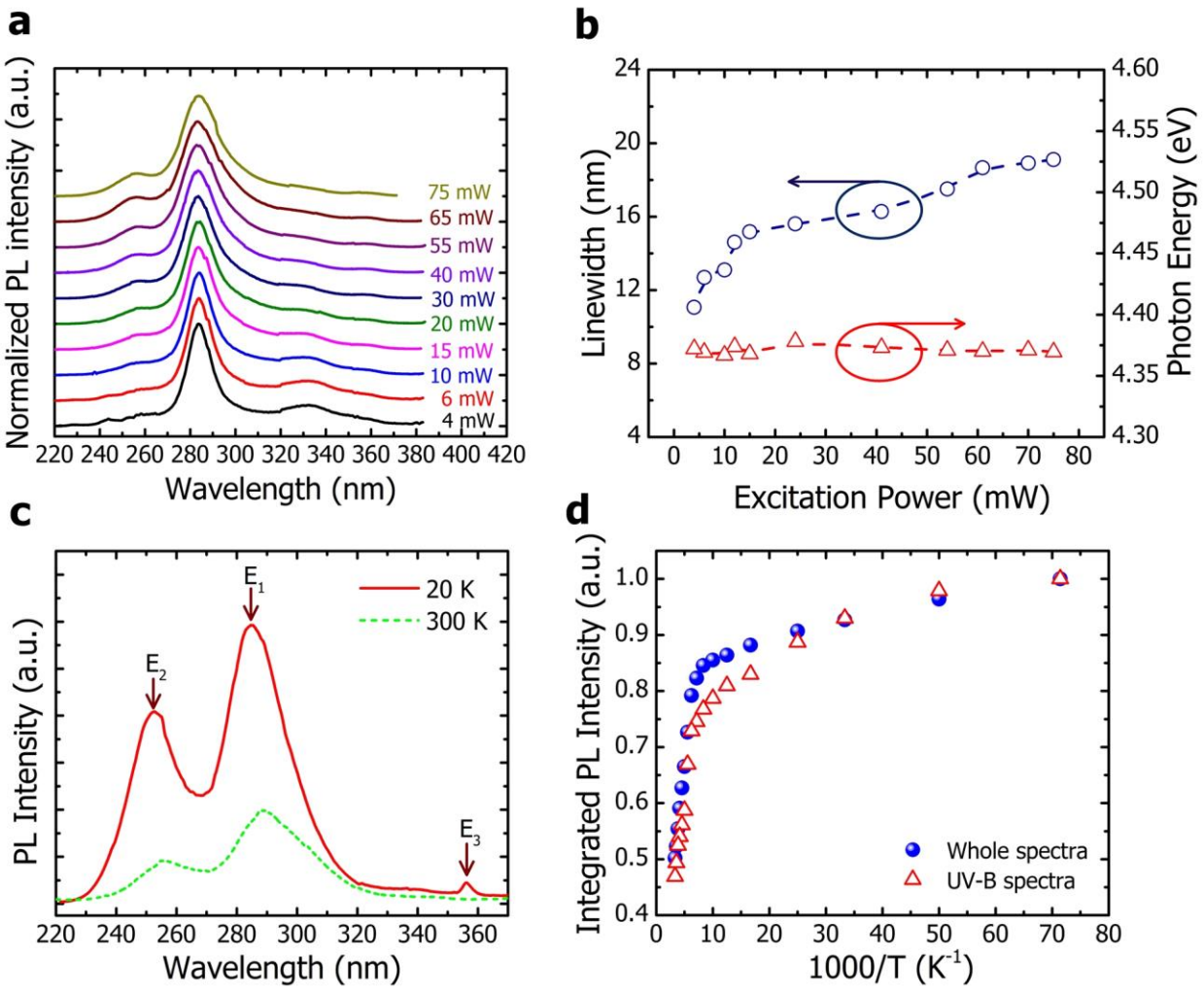

Figure 4-7: (a) Excitation power-dependent PL spectra measured at 300 K. Each spectrum was normalized by its individual peak intensity and shifted vertically for display purpose; (b) PL linewidth and peak energy as functions of excitation power. (c) PL spectra measured at 300 K and 20 K under an excitation power of ~50 mW. E1, E2 and E3 correspond to peak emission from $Al_{0.48}Ga_{0.52}N$ active region, $Al_{0.6}Ga_{0.4}N$ cladding layers and GaN-related, respectively. (d) Arrhenius plots of the integrated PL intensity measured from 20 to 300 K for the active region (E1) emission and the whole spectra.

We further performed temperature dependent PL studies from 20 to 300 K under excitation of a 193 nm laser source. Shown in Figure 4-7c is the PL spectra measured at 20 K and room-temperature under an excitation power of 50 mW. The emission peaks E_1 (~285 nm) and E_2 (~255

nm) correspond to the transitions associated with the $Al_{0.48}Ga_{0.52}N$ active region and $Al_{0.6}Ga_{0.4}N$ cladding layers, respectively. The GaN-related emission (E_3) at ~355 nm is also identified at low temperature. It is also seen that, with decreasing temperature, the emission peak E_1 exhibits a small blue-shift which has been commonly observed in previous studies [144, 229]. The IQE can be approximately estimated by the equation $IQE \sim I_{PL}(RT)/I_{PL}(LT)$, wherein $I_{PL}(RT)$ and $I_{PL}(LT)$ are the integrated PL intensity measured at room and low temperature, respectively. By assuming a near-unity IQE at 20K, Figure 4-7d shows the normalized integrated PL intensities of both whole and active region spectra measured under excitation of 50 mW as a function of temperature in an Arrhenius plot. The IQE of the active region emission (E_1) is derived to be ~45% at room-temperature, which is consistent with previously reported IQE trend for AlGaN multiple quantum wells in the limit of extremely low dislocation densities [81]. The entire device structure showed an IQE value of 50% at room-temperature. The superior IQE is largely attributed to the highly effective carrier confinement in the active regions of extremely uniform and nanowire grown selectively.

The nanowire arrays were subsequently fabricated into UV LED devices, schematically shown in Figure 4-9a. The $Al_xGa_{1-x}N$ nanowire DH based LED fabrication process includes the following steps. At first, polyimide resist served as passivation layer was spin-coated to fully cover the nanowires, followed by a dry etching process to reveal the nanowire top surfaces (Figure 4-8).

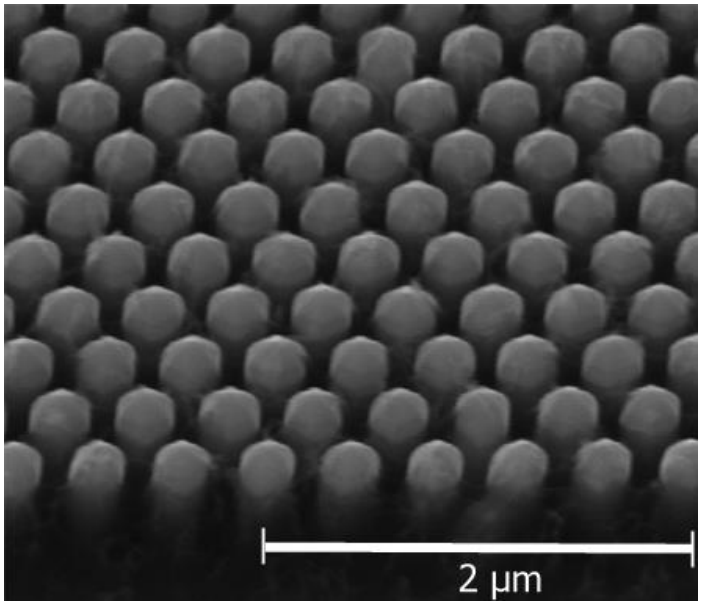

Figure 4-8: A SEM image of AlGaN DH nanowires spin-coated with a polyimide layer. Nanowire top surfaces are revealed by a dry etching process.

To remove any surface oxides, the devices were chemically treated by hydrochloric acid for 30 s immediately preceding metal evaporation. After that, Ni (20 nm)/Au (10 nm) and Ti (20 nm)/Au (100 nm) contact layers were deposited on the device top surface and *n*-GaN template to serve as *p*- and *n*-metal contacts, respectively. An annealing process at 550 ºC was performed in N_2 gas ambient for 1 min. Finally, multiple metal grid patterns were deposited on the device surface to facilitate the hole transport and injection process. The devices exhibit excellent current-voltage (I-V) characteristics.

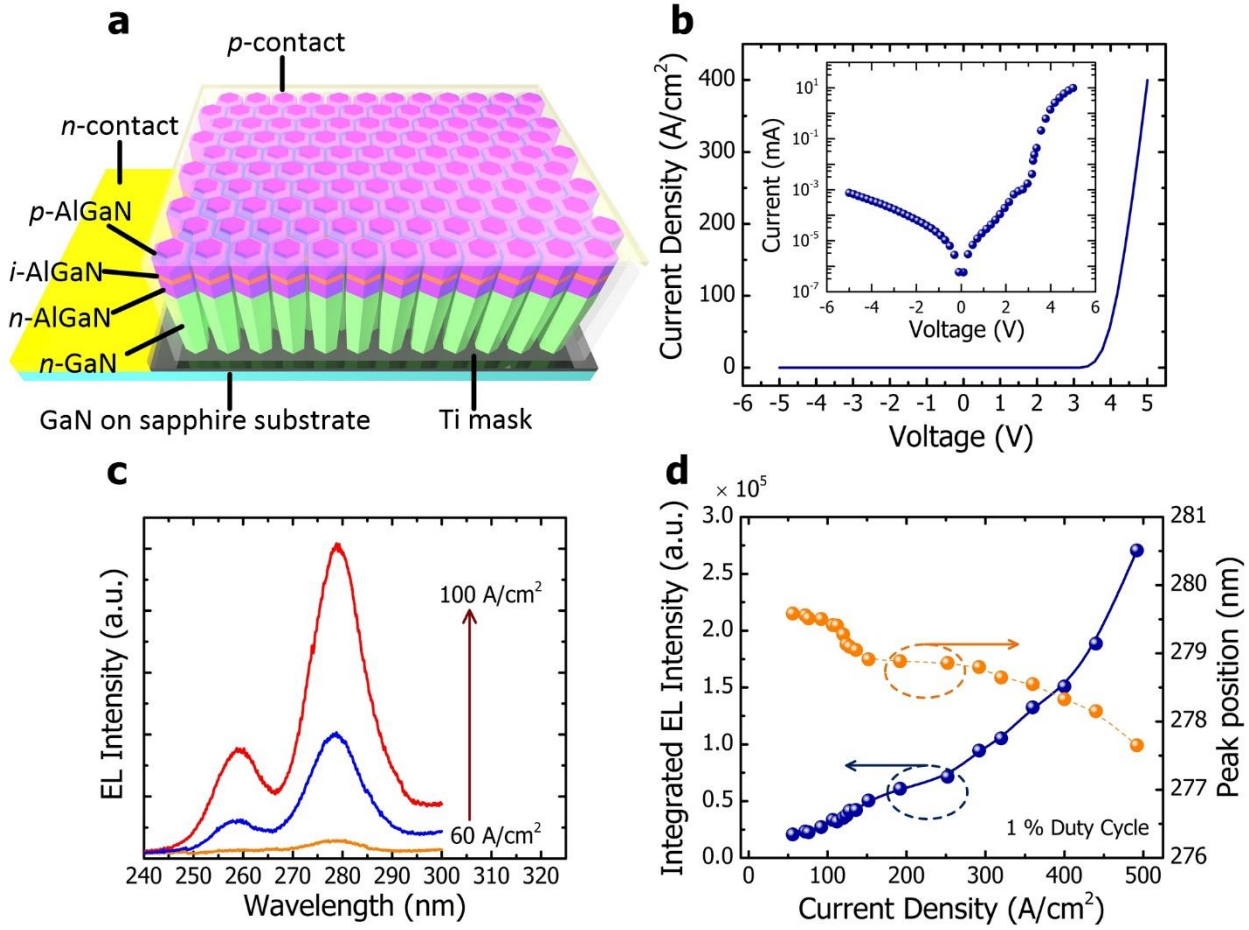

Figure 4-9: (a) Schematic illustration of $Al_xGa_{1-x}N$ LED device with a metal contact; (b)Typical I-V curve of $Al_xGa_{1-x}N$ nanowire DH based LEDs with device size 50 × 50 μm^2. Inset: I-V characteristics of device under forward and reverse bias under semi-log scale; (c) Electroluminescence (EL) spectra of AlGaN DUV LEDs measured under different injection currents. (d) Integrated EL intensity and peak position as a function of current density measured at room-temperature under pulsed biasing conditions (duty cycle of 1%).

Shown in Figure 4-9b is the I-V curve for nanowire-based UV LEDs with areal size 50 × 50 μm^2. The device has a small turn-on voltage of ~3.7 V, and the operation voltage is of ~4.1 V for a current density of 100 A/cm^2, which is much better than AlGaN MQWs LED devices operating at similar wavelength [230]. The room-temperature EL spectra are shown in Figure 4-9c. The devices exhibit strong emission at 279 nm. For such high carrier concentrations, the luminescence emission

peak is typically blue-shifted relative to the energy bandgap of AlGaN. With increasing injection current, the peak emission (E_1) exhibits a small blue-shift, i.e. from 279.6 nm at 50 A/cm^2 to 277.6 nm at 500 A/cm^2, which is related to quantum-confinement Stark effect (Figure 4-9d) [231]. The EL spectral linewidth is ~18 nm. The weaker emission peak at 260 nm is due to electron overflow and emission from the *p*-$Al_{0.6}Ga_{0.4}N$ layer. No other peak emission can be observed in visible wavelength range, which is in contrast to defect-related emissions commonly reported in $Al_xGa_{1-x}N$ MQW UV LEDs because of the deep level defects in $Al_xGa_{1-x}N$ [230]. Illustrated in Figure 4-9d is the integrated EL intensity as a function of injection current. The measurements were performed for current density ranging from 50 A/cm^2 to 500 A/cm^2 with 100 ns pulses at 1% duty cycle to reduce self-heating effect. As seen, the electroluminescence intensity increases near-linearly with increasing injection current. The output power at current density of 500 A/cm^2 is estimated to be ~3.5 W/cm^2. Significantly enhanced light output power is expected by improving carrier injection efficiency and optimizing the light extraction efficiency.

4.4. Conclusion

In summary, we have successfully demonstrated Al-rich $Al_xGa_{1-x}N$ nanowire arrays grown by selective area epitaxial growth technique, covering the entire UV spectral range. The nanowires exhibit high crystal quality confirmed by detailed (S)TEM studies and superior optical property including an IQE of ~45% and a PL linewidth of 11 nm under excitation of 193 nm laser at room-temperature. We also demonstrated for the first time SAG $Al_xGa_{1-x}N$ nanowire based DUV LEDs emitting at 279 nm with superior optical and electrical performance, including a small turn-on voltage of ~3.7V and a light output power of ~3.5W/cm^2 at a current density of 500 A/cm^2. The realization of tunable emission of well-controlled $Al_xGa_{1-x}N$ nanowires grown by SAG technique

as well as superior performance of DUV devices made from such nanowires will provide great potential in optoelectronic applications operating in UV range.

Chapter 5: Controlled Coalescence of AlGaN Nanowire Arrays: An Architecture for Nearly Dislocation-Free Planar Ultraviolet Photonic Device Applications

5.1. Introduction

The performance of GaN-based devices, including LEDs, LDs and transistors depends critically on the material quality. To date, dislocation densities on the order of 10^8 cm^{-2}, or higher have been commonly measured in AlGaN and InGaN heterostructures grown on sapphire, SiC and other foreign substrates [13, 80, 81]. With the use of epitaxial lateral overgrowth, significantly reduced dislocation densities (~10^6 cm^{-2}) have been achieved in GaN film structures [84, 89-91]. A limitation of this approach, however, is that dislocation reduction occurs primarily over the mask regions, instead of the entire film [84, 86]. Another major challenge for achieving high performance LEDs and lasers operating in the deep visible and deep UV spectral ranges is the large polarization fields associated with the conventional *c*-plane of wurtzite III-nitrides [100-104]. Such critical challenges can be potentially addressed by utilizing low-defect density semipolar/nonpolar GaN, AlN, and AlGaN (or InGaN) templates/substrates [67, 78, 232-234]. Progress in this field, however, has been severely hindered by the lack of low-cost, large-area, high-quality semipolar/nonpolar substrates. Alternatively, nearly dislocation-free (Al)GaN, or (In)GaN nanowire heterostructures can be readily achieved on foreign substrates, due to the efficient surface stress relaxation [142, 145, 220, 235]. The use of nanowires for large area deep UV LEDs, however, has been limited by the lack of suitable UV-transparent polymers for surface passivation and planarization. Attempts have been made to form large-area planar structures

through nanowire coalescence [166, 236]. The resulting suspended film can then serve as a virtual template/substrate for the epitaxy of various electronic and photonic devices and eliminate the need of surface passivation and planarization. Previous studies have focused on the use of spontaneously formed nanowires [166-168, 236], schematically illustrated in Figure 5-1a. Due to the lack of control over their size, height, morphology, and twist/tilt in crystal orientation [152, 166, 167, 169-171], the coalescence of such randomly mis-oriented nanowires generally leads to the presence of strain, inversion domains, low-angle grain boundaries and networks of structural defects including dislocations at the coalescence boundary [167, 171-173]. Shown in insets of in Figure 5-1a are schematic diagrams of in-plane and out-of-plane views when two mis-oriented nanowires coalesce at a grain boundary with tilt angle θ, as represented by a simple cubic structure. Such low-angle grain boundaries results in a periodic network of edge dislocations of spacing d with Burgers vector $\boldsymbol{b}$ modeled using the Frank equation [237],

$$d = \frac{\boldsymbol{b}}{2\sin(\frac{\theta}{2})} \qquad \text{Eq. (5-1)}$$

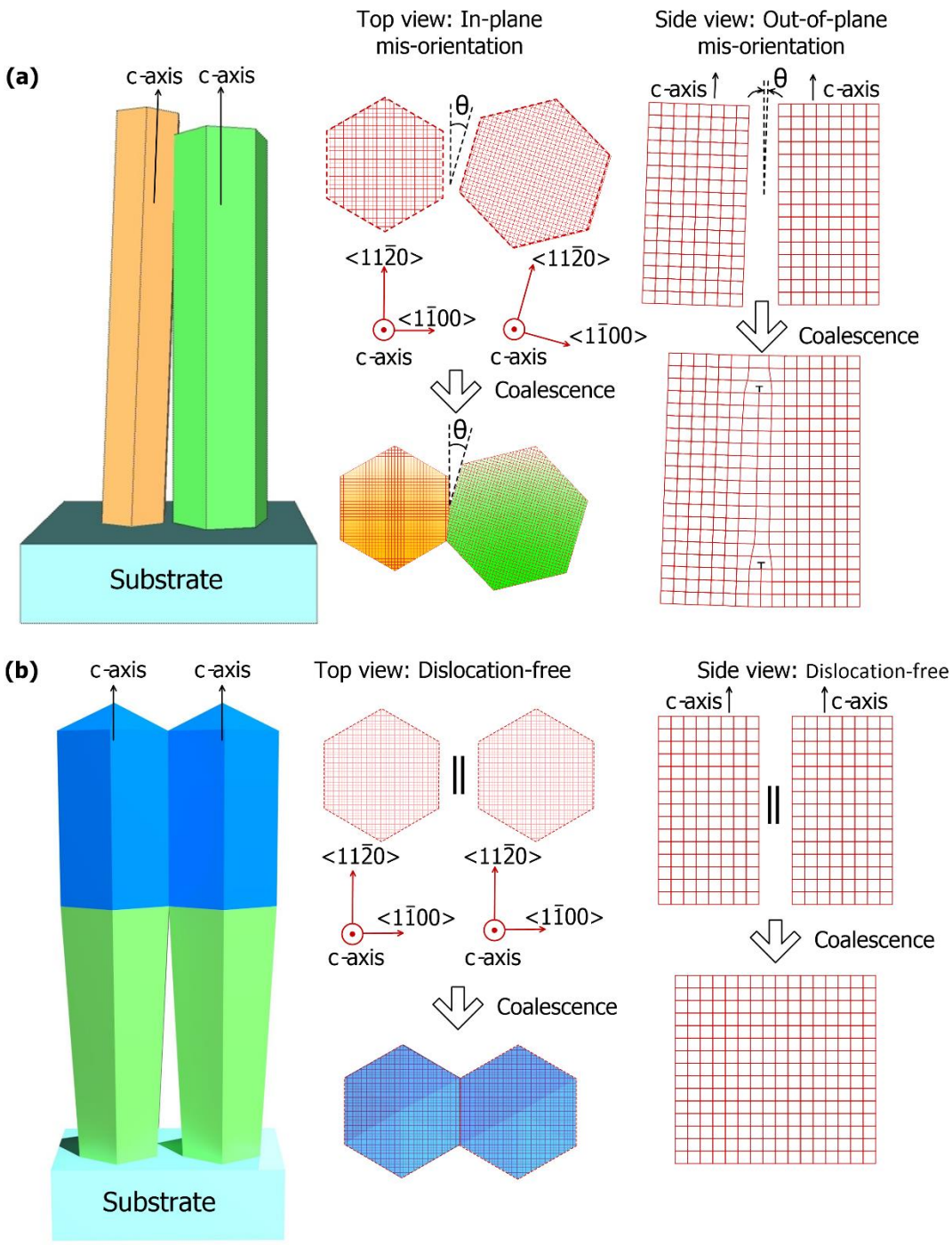

Figure 5-1: (a) Schematic illustration of the coalescence of mis-oriented nanowires, resulting in low-angle grain boundaries represented by a basic grid-like simple cubic structure. Insets: Top and side views showing in-plane and out-of-plane mis-orientations, respectively. (b) Illustration of the absence of dislocations when two nanowires with nearly identical orientations are coalesced. Insets: Top and side views showing dislocation-free structures, respectively.

As a consequence, the realization of any practical devices has not been possible. The formation of dislocations, however, can be largely eliminated, schematically shown in Figure 5-1b, if coalesced nanowires have nearly identical orientation relationship with respect to the substrate, *i.e.* negligible small θ. In the coalescence process, the formation of dislocations is not energetically favorable given the presence of a negligible mis-orientation, such that a very small degree of distortion (bond length and bond angle) can be accommodated. Moreover, the gradual increase of the nanowire diameter allows for a controllable, progressive relaxation towards the bulk state, which minimizes the formation of dislocations upon coalescence, illustrated in Figure 5-1b. By suppressing the formation and propagation of dislocations in both the nanowire growth and coalescence process, defect-free AlGaN (or InGaN) templates can be potentially realized on foreign substrates.

Evidently, critical to achieve such a nearly dislocation-free coalescence process is a precise control of the position, size, and orientation of nanowires. In this context, we have demonstrated, for the first time, nearly dislocation-free AlGaN film structures on sapphire substrate (lattice mismatch ~13-16%) through controlled coalescence of GaN/AlGaN nanowire arrays via selective area epitaxy. Detailed scanning transmission electron microscopy (STEM) studies further show that the coalesced AlGaN film consists of semipolar $\{1\bar{1}03\}$ planes and possess strong chemical ordering, which leads to strong quantum-confinement of charge carriers and reduced polarization field. With the incorporation of Mg-dopant, the coalesced AlGaN film exhibits excellent *p*-type characteristics, including a free hole concentration of ~7.4×10^{18} cm^{-3} and mobility of ~8.85 $cm^2/V\cdot s$ at room-temperature, which are nearly a factor of ten and two times higher than previously reported values, respectively.[34-36] We have further demonstrated semipolar AlGaN LEDs, which operate at ~340 nm and exhibit excellent electrical and optical performance, including an IQE of ~83% and an output power of 15 W/cm^2 for an unpackaged device at an injection current of 90

mA (900 A/cm^2). By forming nearly dislocation-free AlGaN templates through controlled nanowire coalescence, this work provides a viable approach for achieving high efficiency GaN-based semipolar deep UV light emitters, including LEDs and laser diodes directly on sapphire, or other low-cost, large-area substrate.

5.2. Coalesced AlGaN Nanowire Arrays by Selective Area Growth

Schematically shown in Figure 5-2a, the selective area epitaxy of GaN/AlGaN nanowire arrays takes place on 2D GaN template on *c*-plane sapphire substrate by employing a thin (~10 nm) Ti layer as the growth mask (see Section 4.2) [186, 238, 239]. Nanohole arrays were then created on the Ti mask by using the afore-described procedure, including e-beam lithography and reactive ion etching. Hexagonal openings were arranged in a triangular lattice, with a lattice spacing *a* and a lateral size *h* for each opening. The nano-patterned substrate was then cleaned using standard solvent prior to loading into the MBE growth chamber. The Ti layer was nitridized in the reaction chamber at 400ºC to prevent the formation of cracks and degradation at elevated temperature. GaN nanowire arrays (height ~350 nm) were first selectively grown in the opening apertures by using radio frequency plasma-assisted molecular beam epitaxy (MBE), then followed by AlGaN segments. The growth conditions for GaN/AlGaN nanowire heterostructures included the following steps. *n*-Type GaN nanowire arrays were first grown with a substrate temperature of 915 °C, nitrogen flow rate of 0.33 sccm, and Ga flux of ~1.3×10^{-7} Torr. Subsequently, the *n*- and *p*-type AlGaN cladding layers were grown at substrate temperatures of 960 – 980°C, and Ga and Al beam fluxes of ~1.05×10^{-7} Torr and ~3.3×10^{-8} Torr, respectively. The AlGaN active layer was grown with a nitrogen flow rate of 0.33 sccm, substrate temperature of 980°C, Ga and Al beam fluxes of ~1.05×10^{-7} Torr and ~1.86×10^{-8} Torr, respectively. The substrate temperature mentioned here refers to the thermocouple reading on the backside of the substrate. The real substrate surface

temperature is 100 – 150°C lower, depending on the substrate and sample size. Mg beam equivalent pressure was ~2.8×10^{-9} Torr for the Mg-doped AlGaN layer.

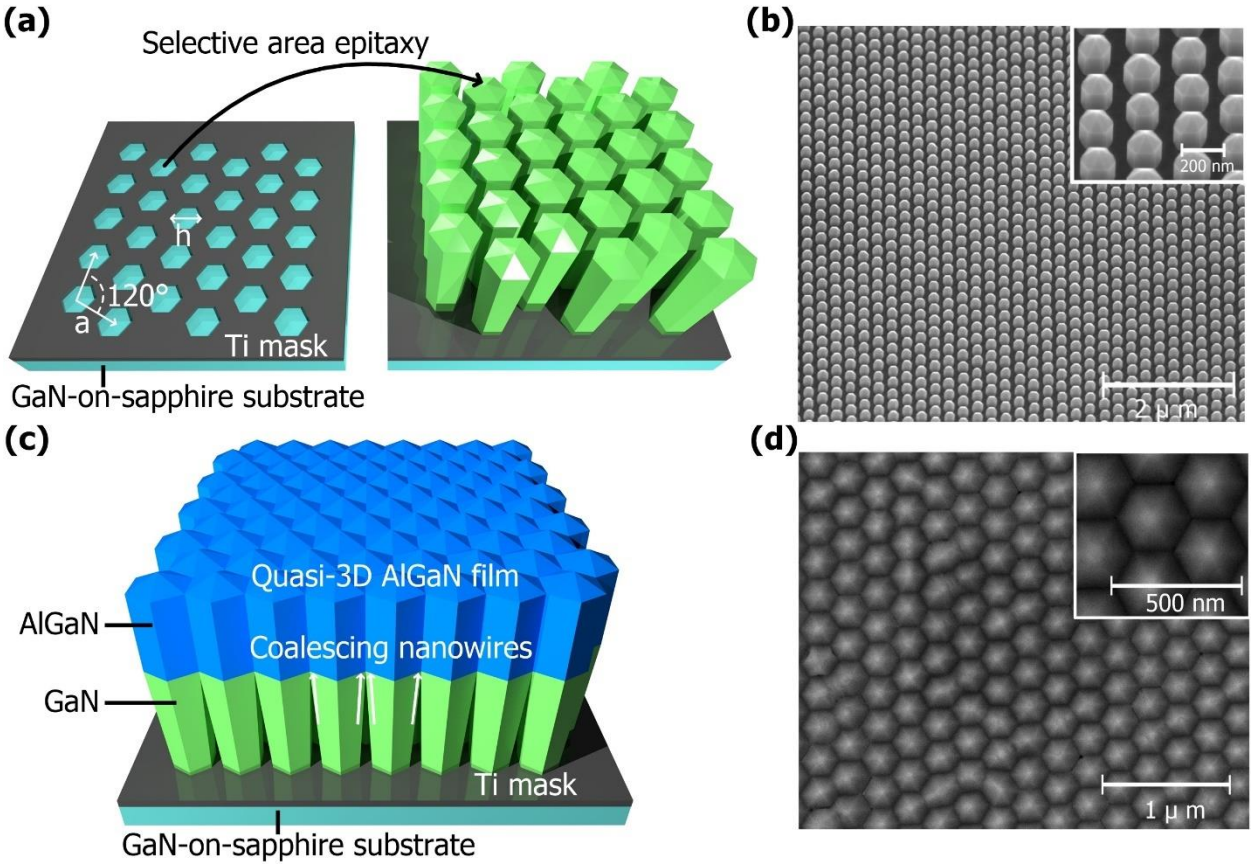

Figure 5-2: (a) Left: Arrays of nanoscale opening apertures defined by e-beam lithography process on a Ti mask on planar GaN template on *c*-plane sapphire substrate. Right: Schematic of the selective area epitaxy of GaN nanowire arrays on the nano-patterned substrate. (b) 45°-tilted view SEM image showing GaN nanowire arrays selectively grown in the opening apertures. Inset: High-magnification SEM image of GaN nanowire arrays. (c) Illustration of the concept of gradual coalescence process that leads to the formation of semipolar AlGaN film structures. (d) Top-view SEM image of the AlGaN film structure formed through controlled coalescence of AlGaN nanowire arrays grown on sapphire substrate with a lattice spacing *a* ~250 nm and a lateral size *h* ~180 nm for each opening. Inset: High-magnification SEM image of coalesced AlGaN nanowire arrays.

Shown in Figure 5-2b is the SEM image of GaN nanowires, which exhibit a high degree of size uniformity and are vertically aligned along the *c*-axis. Each nanowire has a well-defined hexagonal pyramid morphology comprised of six semipolar top facets. Subsequently, AlGaN nanowire segments were grown on top of the GaN nanowire template (see experimental section). The incorporation of Al leads to a small enhancement of the lateral growth, which is estimated to be ~1 nm/min. As a consequence, the spacing between neighboring nanowires is slowly reduced as growth proceeds, leading to a gradual coalescence between neighboring nanowires, illustrated in Figure 5-2c. The top-view SEM image of the resulting AlGaN film structure is shown in Figure 5-2d. Intriguingly, the AlGaN film consists of well-ordered semipolar planes, which was also demonstrated previously in coalesced InGaN nanowire arrays [240]. Such unique quasi-three-dimensional semipolar surface offers several advantages, including reduced polarization fields, enhanced Mg-dopant incorporation [241, 242], and efficient strain relaxation to prevent the formation of dislocations and cracks (described in the subsequent Section).

5.3. Device Characterization

5.3.1. Hall Effect Measurement

For practical device applications, it is essential to demonstrate efficient *p*-type conduction in the coalesced AlGaN layers. In GaN-based materials, the presence of point defects and dislocations generally leads to *n*-type characteristics. The performance of AlGaN-based UV optoelectronic devices has often been limited by poor *p*-type conduction [243, 244]. In this study, the coalesced $Al_{0.35}Ga_{0.65}N$ layers were doped *p*-type with Mg. The Mg doping concentration is estimated to be in the range of 10^{20} cm^{-3}, which was derived based on secondary ion mass spectroscopy

measurements on Mg-doped epilayers grown under similar conditions. *p*-Type conduction was confirmed by Hall effect measurements, schematically shown in Figure 5-3.

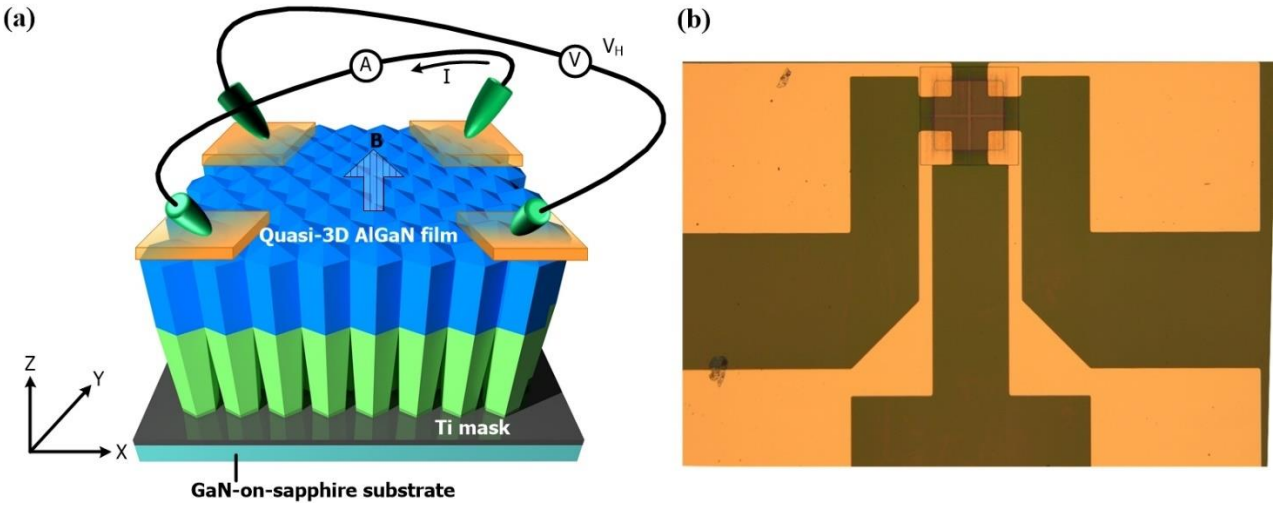

Figure 5-3: (a) Schematic setup of Hall effect measurements of Mg-doped AlGaN layers using standard Van der Pauw configuration. (b) An optical image of fabricated device for Hall effect measurements.

Hall effect measurement was performed at various temperatures to measure the free hole concentration and mobility of Mg-doped AlGaN layers using the standard Van der Pauw configuration. The coalesced AlGaN:Mg film region has an area of 100 × 100 μm^2 and a thickness of 50 nm. The metal contact consists of Ni (20 nm)/Au (100 nm) layers, which were deposited by e-beam evaporator and annealed at 550ºC in N_2 ambient for 1 min to form Ohmic contacts. Below the coalesced AlGaN film are discrete GaN nanowires, which are non-doped and spatially isolated. The magnetic field strength is 3000 Gauss. The sample was mounted in a cryostat for temperature variable Hall effect measurements.

Shown in Figure 5-4a are the variations of Hall mobility (μ_H) and hole concentration (p) in the temperature range of 77 K to 300 K. At room-temperature, the hole mobility and concentration are ~8.85 $cm^2/V{\cdot}s$ and ~7.4 × 10^{18} cm^{-3}, respectively. The coalesced, free-standing AlGaN film

structure exhibits a factor of two enhancement in hole mobility and at least an order of magnitude higher hole concentration, compared to previous studies on *p*-type AlGaN epilayers [92, 245]. Significantly enhanced Mg-dopant incorporation and activation efficiency have also been reported previously for semipolar GaN compared to GaN(0001) [241, 242].

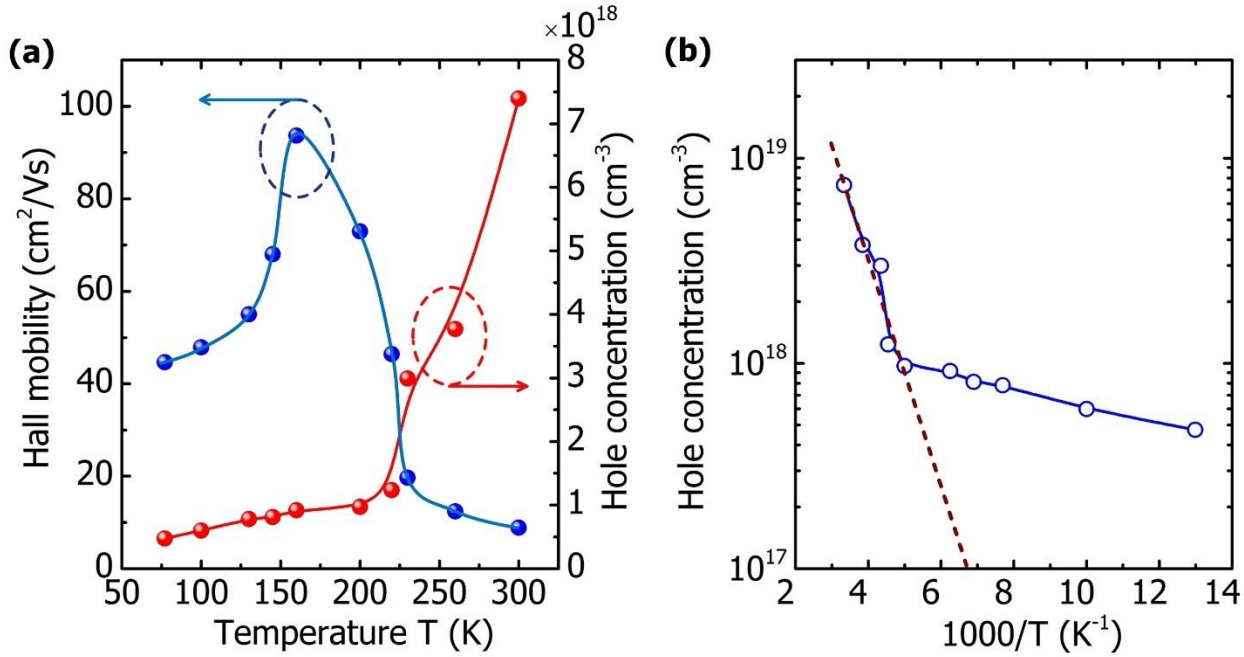

Figure 5-4: (a) Variation of Hall mobility and hole concentration of Mg-doped AlGaN contact layer as a function of temperature. (b) Hole concentration of *p*-AlGaN as a function of reciprocal temperature. Dashed line is the fitting result of the Arrhenius plot.

Shown in Figure 5-4a, the mobility increases with decreasing temperature and reaches a peak value ~94 $cm^2/V{\cdot}s$ at 160 K. With further decreasing temperature, the mobility shows a small decrease. The hole concentration decreases with temperature, due to carrier freeze-out. An Arrhenius plot of the hole concentration as a function of reciprocal temperature is shown in Figure 5-4b. The acceptor activation energy (E_A) can be fitted by the following equation [246],

$$\frac{p(p+N_D)}{N_A-N_D-p} = \frac{N_V}{g}\exp\left(-\frac{E_A}{kT}\right) \qquad \text{Eq. (5-2)}$$

where p, N_A and N_D are the hole, acceptor and donor concentrations, respectively. N_V is the effective density of states, $N_V = 2(2\pi m_h^* kT)^{3/2}/h^3$, and g is the acceptor degeneracy factor which is assumed to be 2. By using a hole effective mass $m_h^* = 1.5m_0$ for $Al_{0.35}Ga_{0.65}N$ [98], E_A is estimated to be ~47 meV, which agrees well with the previously reported values in Mg-doped AlGaN with Al content above 0.3 and is suggested to be related to hole hopping conduction in the Mg impurity band [92, 247]. Recently, excellent current-voltage characteristics have also been measured from AlN *p-i-n* diode in the temperature range of 77 K to 300 K [145].

5.3.2. Structural Characterization

The realization of high-quality *p*-type AlGaN epilayers provides a distinct opportunity to develop a new generation of UV optoelectronic devices. Illustrated in Figure 5-5a is the schematic diagram of coalesced AlGaN LED heterostructure grown on sapphire substrate, which consists of a 400-nm Si-doped GaN, 120-nm Si-doped $Al_{0.35}Ga_{0.65}N$, 30-nm undoped $Al_{0.14}Ga_{0.86}N$ active region, and 80-nm Mg-doped $Al_{0.35}Ga_{0.65}N$ segment. Shown in Figure 5-5b is the SEM image of the coalesced nanowire arrays taken with a 45° angle. Gradual coalescence was initiated during the growth of *n*-GaN layer. The resulting AlGaN film structure exhibits unique quasi 3-D feature consisting of semipolar top facets. Detailed structural characterization at atomic-resolution was performed with a double aberration-corrected FEI Titan Cubed 80-300 scanning transmission electron microscope (STEM) operated at 200 kV. A cross-sectional TEM specimen of the nanowire arrays (across the coalesced sidewalls) was prepared by focused ion beam (FIB) milling using a Zeiss NVision 40 dual-beam system with deposited Pt and C as protection layer. Atomic-number sensitive (Z-contrast) STEM-high-angle annular dark-field (HAADF) images were obtained using a probe semi-angle of 19 mrad and a detector angular range of 63.8-200 mrad. Elemental mapping by electron energy-loss spectroscopy (EELS) in STEM mode was done with

the Ga $L_{2,3}$ and Al K-edges with the spectrum imaging technique. Weighted-principal components analysis (PCA) was applied for noise reduction of the spectrum images using the multivariate statistical analysis (MSA) plugin implemented within DigitalMicrograph by HREM Research Inc.

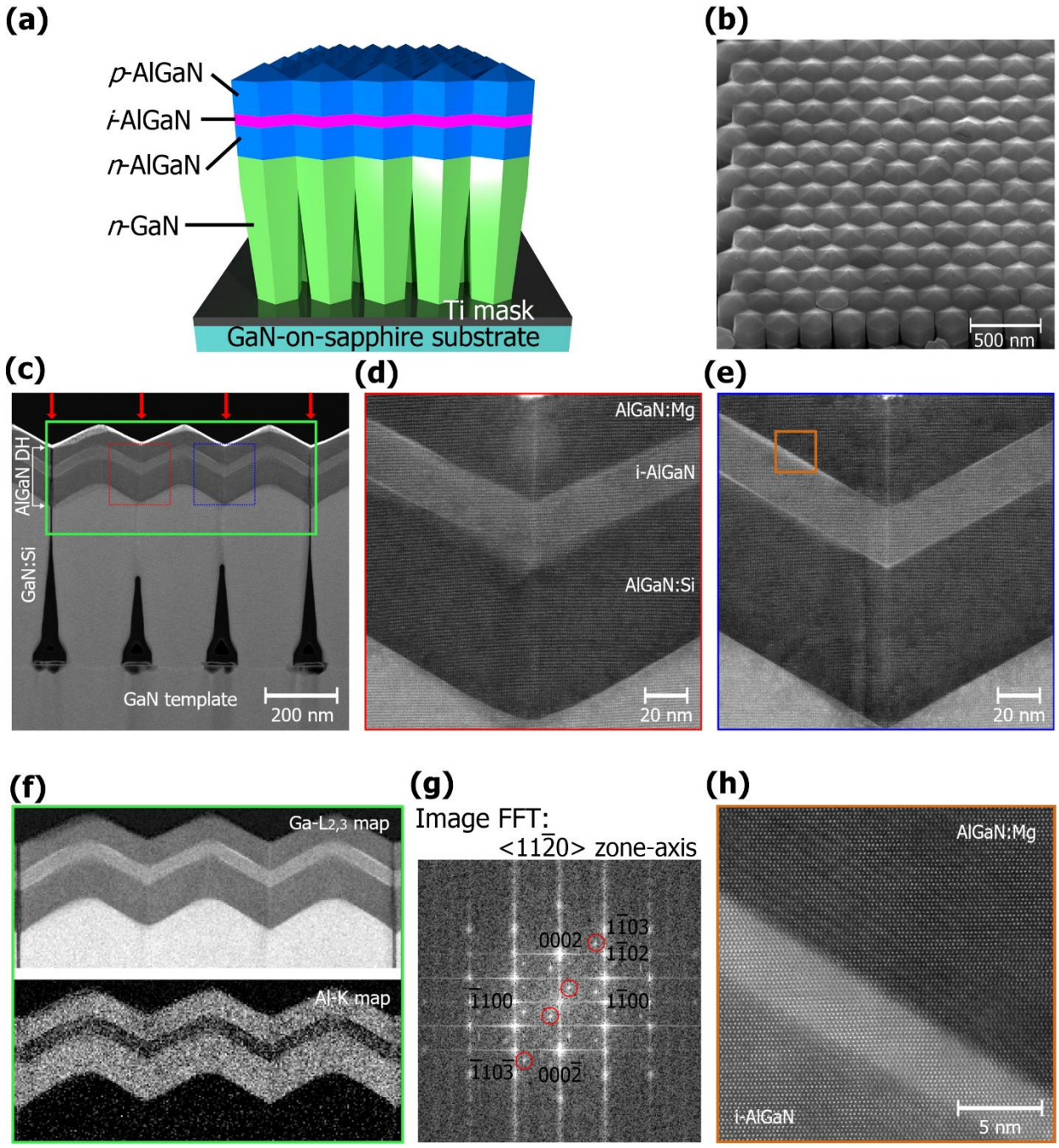

Figure 5-5: (a) Schematic diagram showing AlGaN double heterostructure (DH) LED structure. (b) SEM image of coalesced AlGaN nanowire LED structure. (c) STEM-HAADF image of an array of coalesced AlGaN nanowires in cross-section along $\{11\bar{2}0\}$ zone-axis, showing the apex-like prismatic nature of the nanowires and the coalescence boundaries marked by red arrows. (d)-(e) High-magnification images of the fully coalesced boundaries from boxed region in (c). (f) Elemental maps from STEM-EELS showing the variations in Ga and Al elemental distribution

within the $Al_xGa_{1-x}N$ DH and the *n*-GaN nanowire template. (g) Diffraction pattern from the FFT of the image in (h) indicating the pyramid apex are aligned along the *c*-axis growth direction. The extra satellite reflections (circled in red) with a spacing of $g_{1\bar{1}03}/5$ in the $\langle 1\bar{1}03 \rangle$ direction correspond to the periodicity of the chemical ordering within the AlGaN alloys. (h) High-magnification view of the boxed region in (e) showing the strong image intensity modulations parallel to the faceting along $\langle 1\bar{1}03 \rangle$ in all layers within the AlGaN DH. Bright band at the *i*-AlGaN/AlGaN:Mg interface is attributed to projection effects.

Figure 5-5c is a HAADF image of an array of AlGaN heterostructure nanowires observed in cross-section along the *a*-plane orientation, illustrating the atomic-number sensitive Z-contrast of the imaged material. The brighter regions correspond to the *n*-GaN nanowire template and the AlGaN active region, wherein the Al composition is lower than that of the AlGaN cladding layers. The cross-sectional view confirms *m*-plane termination at the nanowire sidewalls at the AlGaN double heterostructure and top of the *n*-GaN, which are also the coalescence boundary planes. The inclined surfaces in the lower section of the *n*-GaN nanowire template, where the nanowire diameter increases gradually, are composed of $(1\bar{1}00)$ and $(1\bar{1}0\bar{1})$ nano-facets, shown in Figure 5-6. All interfaces in the cross-section show an inclination of ~35°, indicative of semipolar $\{1\bar{1}03\}$ plane termination from the hexagonal pyramidal cap of the *n*-GaN nanowire template, which was relayed to the growth of the subsequent AlGaN heterostructure. Significantly reduced polarization field is therefore expected from such semipolar AlGaN LED active regions, and can be engineered as a function of the inclination angle by altering the surface energies with growth conditions [248]. Moreover, the resulting 3-D surface, compared to a conventional 2-D surface, has shown to be highly effective in strain relaxation during heteroepitaxy [249, 250]. Red arrows are pointed to boundaries where adjacent wires are coalesced in Figure 5-5c. A detailed examination was further

investigated by atomically-resolved STEM images taken at different boxed regions (red, blue, and orange) corresponding to Figure 5-5d, 5-5e, and 5-5h, respectively. No dislocations or stacking faults are observed within the AlGaN double heterostructure in individual wires or at coalescence boundaries, in contrast to the structural defects commonly observed in spontaneous (Al)GaN nanowires [168-170, 173, 251]. A few dislocations were observed in the planar GaN template, but did not propagate into the *n*-GaN nanowire base or they bent towards the nanowire sidewall surface prior to nanowire coalescence as shown in Figure 5-7, similar to patterned AlN nanowire arrays with nanometric air gaps reported previously [252].

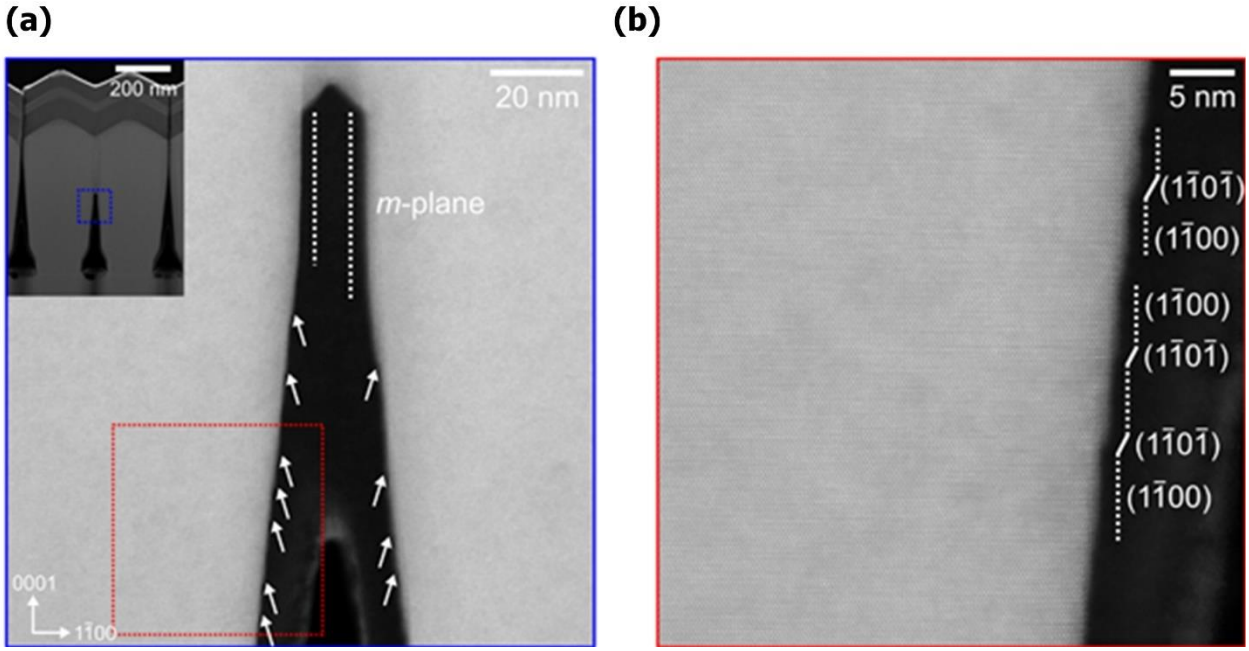

Figure 5-6: STEM-HAADF images of a pair of coalesced AlGaN nanowires in cross-section along $\{11\bar{2}0\}$ zone-axis. (a) High-magnification image of the *n*-GaN nanowire template region at the air-gap below the coalescence boundary. Macroscopic termination of the inclined surface is a $\{4\bar{4}0\,\bar{1}\}$ plane. (b) Detailed view of the red-boxed region in (a), showing atomic-scale nano-facets made up of *m*-plane $(1\bar{1}00)$(dotted lines) and *s*-plane $(1\bar{1}0\bar{1})$ (solid lines) surfaces.

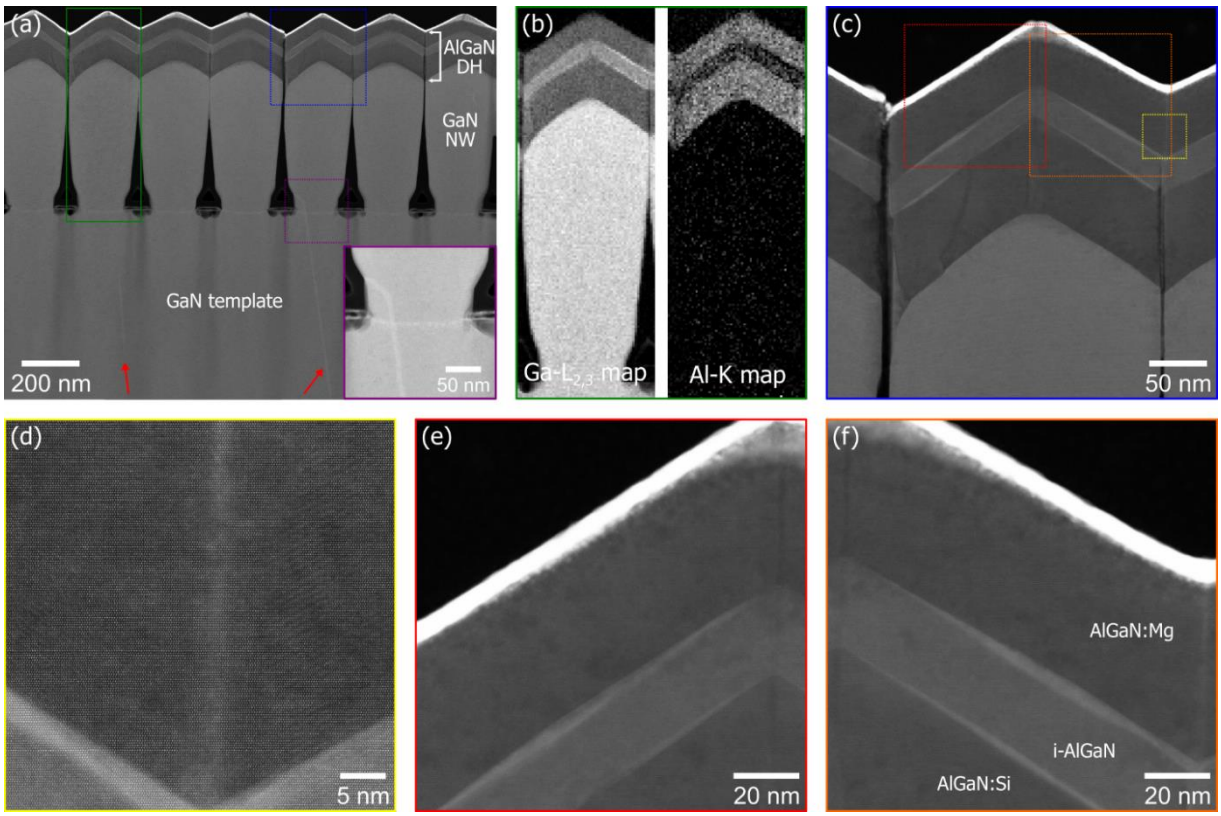

Figure 5-7: (a) STEM-HAADF image of an array of AlGaN nanowires in cross-section along $\{11\bar{2}0\}$ zone-axis with varying degree of coalescence between adjacent nanowires. Two threading dislocations (arrowed in red) in the planar GaN template are also visible; as shown in the inset, one dislocation propagated to the nanowire above and is bent towards the nanowire sidewall. (b) Elemental maps using STEM-EELS from the nanowire boxed in green in (a) showing the variations in Ga and Al elemental distribution within the $Al_xGa_{1-x}N$ DH and the n-GaN nanowire template. Minor segregation of Al at the coalescence boundary on the right is visible. (c) Higher magnification view of the nanowire region boxed in blue in (a). (d)-(e)-(f)**,** various detailed views of regions marked in (c) of the top AlGaN:Mg layer.

Additional diffraction contrast imaging in TEM under weak-beam dark-field conditions (g = 0002 and g = $1\bar{1}00$) further confirmed that the AlGaN nanowires examined are dislocation-free. The image fast Fourier transform (FFT) in Figure 5-5g shows that the apex of the hexagonal pyramid is aligned along [0002]. The crystal lattice is well-aligned and coherent across the coalescence

boundary, and suggests a negligible misalignment in crystal orientation at the boundary of adjacent nanowires (< 0.25° mis-orientation in the zone-axes were observed in the electron diffraction from adjacent nanowires). Assuming edge dislocations with Burgers vector of $\boldsymbol{b} = 1/3 \langle 11\bar{2}0 \rangle$ as in the case of low-angle grain boundaries as depicted schematically in Figure 5-1a, the spacing of any dislocations due to a mis-orientation in adjacent nanowires is estimated using the Frank equation (Equation (5-1)) [237]. A mis-orientation of < 0.25° is estimated to generate dislocations separated by a distance of ~75 nm, which is similar to the TEM cross-section thickness (~65 – 70 nm) and the coalescence boundary in contact along *m*-plane (~90 – 100 nm) between air gaps. As a result, the formation of dislocations is not necessary, nor energetically favorable at the coalescence boundary.

We have further performed EELS elemental mapping of the nanowires and confirmed the formation of AlGaN double heterostructures in Figure 5-5f by changes in the Ga and Al concentrations between the cladding and active layers (see also Supporting Information). High-magnification view of the AlGaN double heterostructure reveals strong STEM-HAADF image intensity modulations along the $\langle 1\bar{1}03 \rangle$ directions within both the AlGaN cladding and AlGaN active regions (see Figure 5-5h), which can lead to strong quantum-confinement of charge carriers. Such image intensity modulations have a periodicity of ~7.4 Å (5 times the $\{1\bar{1}03\}$ plane d-spacing from satellite reflections in Figure 5-5g), and can be attributed to chemical ordering (alternating Al-rich/Ga-rich planes) within the AlGaN alloys [253]. Similar compositional fluctuations have been previously documented in self-organized AlGaN nanowires both along the *c*-plane and inclined from the *c*-axis on semipolar planes [228]. The semipolar plane faceting of various interfaces suggests that the growth front progressed along such pyramidal planes, leading

to the kinetically driven modulation of Ga- and Al-incorporation that results in spontaneous chemical ordering at the growth surface [228, 253].

5.3.3. Optical and Electrical Characterization

Optical properties of the semipolar AlGaN LED heterostructures were studied using temperature-dependent PL spectroscopy. PL measurements were carried out using a 266 nm diode-pumped solid-state (DPSS) laser. A UV neutral density filter was used to adjust the laser excitation power. The emitted light was collected and spectrally resolved by a high-resolution spectrometer and detected by a liquid nitrogen cooled CCD. A long pass filter (> 270 nm) was placed in front of the spectrometer to eliminate scattered light from the laser beam. Temperature dependent PL measurements were performed by using a helium closed-loop cryostat with temperature varying in range of 20 K to 300 K.

Illustrated in Figure 5-8a is the PL spectra measured at 20 K and room-temperature under an excitation power of 4 mW. The emission peaks E_1 (~340 nm) and E_2 (~304 nm) correspond to the transitions associated with the $Al_{0.14}Ga_{0.86}N$ active region and $Al_{0.35}Ga_{0.65}N$ cladding layers, respectively. The GaN-related emission at ~358 nm (E_3) is also identified. Figure 4b shows the normalized integrated PL intensity of the active region and the entire device as a function of temperature in an Arrhenius plot. The IQE is estimated by $I_{PL}(RT)/I_{PL}(20\ K)$, wherein $I_{PL}(RT)$ and $I_{PL}(20\ K)$ are the integrated PL intensity measured at room-temperature and 20 K, respectively, assuming a near-unity IQE at 20K.

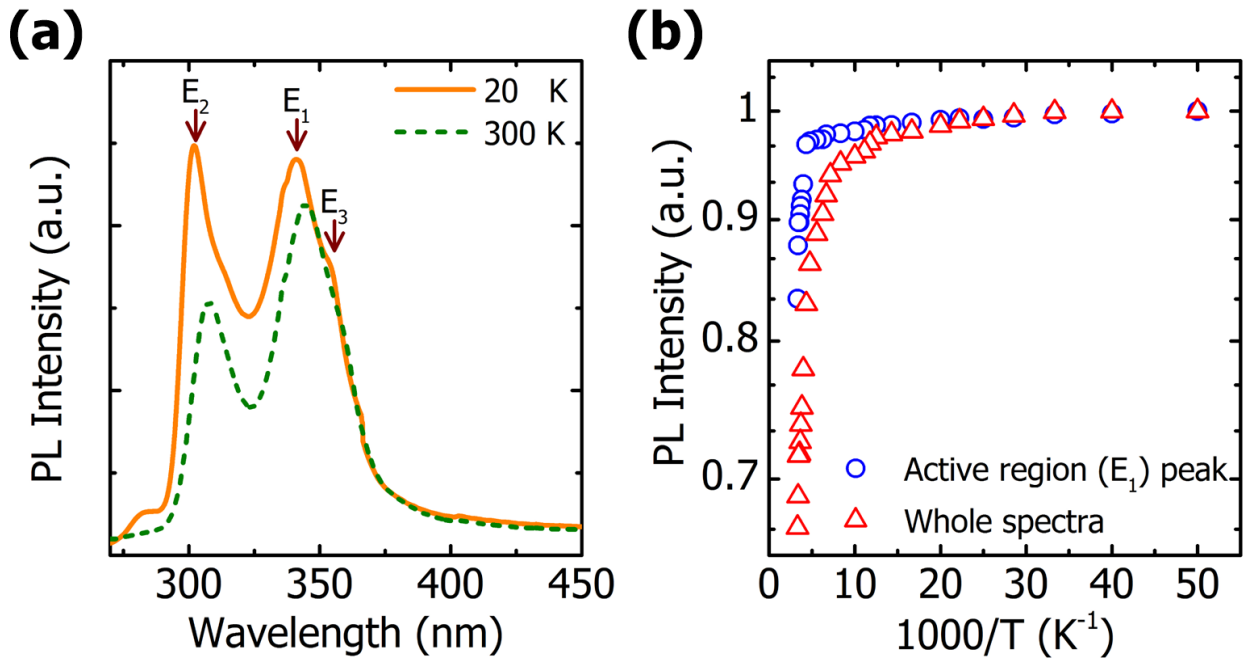

Figure 5-8: (a) Photoluminescence (PL) spectra measured at 300 K and 20 K under an excitation power of 4 mW. E_1, E_2 and E_3 correspond to peak emission from $Al_{0.14}Ga_{0.86}N$ active region, $Al_{0.35}Ga_{0.65}N$ cladding layers and GaN, respectively. (b) Variations of the integrated PL intensity vs. inverse temperature for the active region (E_1) emission and the whole spectra.

The IQE of the active region emission (E_1) is derived to be ~83% at room-temperature, which is consistent with previously reported IQE trend for AlGaN multiple quantum wells in the limit of extremely low dislocation densities [81]. The entire device structure showed an IQE value of 65% at room-temperature, which is also significantly better than AlGaN ternary nanowires measured under similar conditions [144]. The superior optical performance is consistent with the suppression of dislocations in the coalesced film structures demonstrated by (S)TEM studies. Moreover, the quantum-confinement of charge carriers and the reduced polarization field, due to the presence of the extensive periodic chemical ordering in the active region and the semipolar surfaces, respectively, also contribute to the extremely high luminescence efficiency.

Schematically shown in Figure 5-9a, semipolar AlGaN LEDs were subsequently fabricated and characterized. The fabrication of semipolar AlGaN LED devices included the following steps. Ni (20 nm)/Au (10 nm) and Ti (20 nm)/Au (100 nm) contact layers were deposited on the device top surface and *n*-GaN template to serve as the *p*- and *n*-metal contacts, respectively. Prior to metal deposition, the sample was soaked in hydrochloric acid for 30 s to remove any surface oxides. An annealing process was performed at 550ºC in N_2 gas ambient for 1 min. Multiple metal grid patterns were then deposited on the device surface to facilitate the hole transport and injection process. The current-voltage characteristics of semipolar AlGaN LEDs were measured using a source meter Keithley SMU 2400. The emitted light was collected and spectrally resolved by a high-resolution spectrometer and detected by a CCD. For a given injection current, the output power of semipolar AlGaN LEDs was measured by an optical power meter.

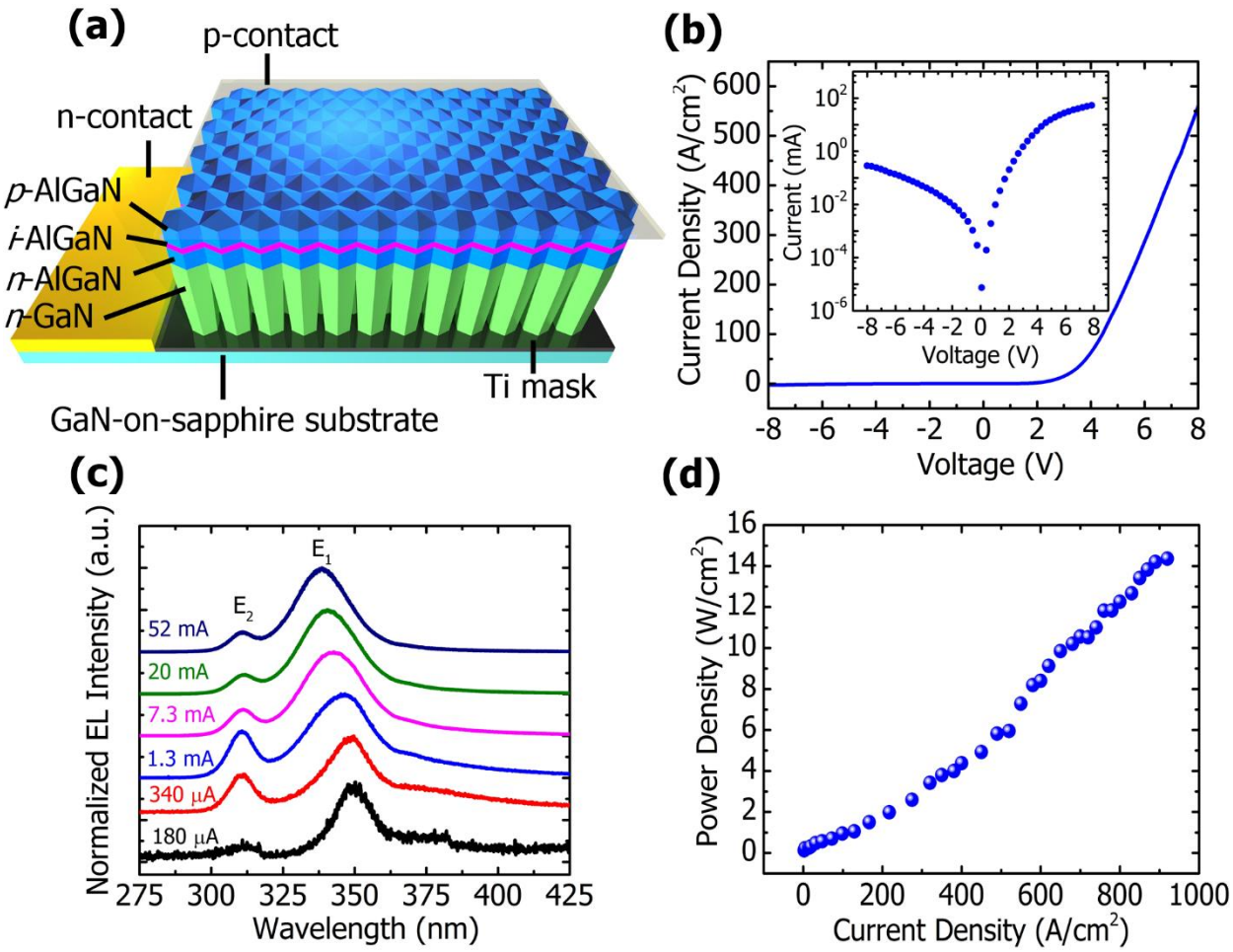

Figure 5-9: (a) Schematic illustration of semipolar AlGaN LED device with metal contacts. (b) Typical I-V curve of AlGaN semipolar LEDs with device size 100×100 μm^2. Inset: *I-V* characteristics plotted in semi-log scale. (c) Electroluminescence (EL) spectra of semipolar AlGaN LEDs measured under different injection currents. (d) Light output power vs. current density measured at room-temperature under pulsed biasing conditions (duty cycle of 1%).

The devices exhibit relatively good current-voltage characteristics. Shown in Figure 5-9b is the I-V curve for a device with an area size of 100 × 100 μm^2. The device has a small turn-on voltage ~3.3 V, and the operation voltage is ~4.4 V for a current density of 100 A/cm^2, which is comparable to, or better than AlGaN MQW based LED devices operating at similar wavelengths [254-257]. The leakage current measured under reverse bias is likely through any non-coalesced nanowires

in the large area device, since no surface passivation or planarization layer was used during the device fabrication. The EL spectra measured at room-temperature are shown in Figure 5-9c. The devices exhibit strong emission at 340 nm, which agrees well with the PL measurements. The very weak emission peak at 310 nm is due to electron overflow and emission from the *p*-AlGaN layer. No other defect-related emission is observed in the visible wavelength range. For comparison, such defect-related emission has been commonly reported in AlGaN quantum well UV LEDs, due to the presence of deep level defects in conventional AlGaN epilayers [230]. This further confirms the superior quality semipolar AlGaN film structures formed by controlled nanowire coalescence. It is also seen that, with increasing current, the emission peak (E_1) exhibits a small blue-shift, which is related to the filling of the Ga-rich regions, due to the presence of extensive chemical ordering, and is also partly induced by the quantum-confined Stark effect [231]. The spectral linewidth (full-width-at-half-maximum) increases from 18 nm at 1.7 A/cm^2 to 25 nm at 80 A/cm^2 and then remains constant with further increasing current. Illustrated in Figure 5-9d is the measured output power vs. current for the semipolar AlGaN LEDs. It is seen that the output power increases near-linearly with injection current, and an output power of ~15 W/cm^2 was measured at room-temperature at current density of 900 A/cm^2. Significantly enhanced output power is expected by optimizing the light extraction efficiency.

5.4. Conclusion

In summary, in this Chapter, we have demonstrated semipolar AlGaN templates through controlled nanowire coalescence on sapphire substrate. Detailed (S)TEM studies confirmed that such unique AlGaN quasi 3-D film structures are nearly free of dislocations, which is unequivocally supported by the extremely high room-temperature luminescence efficiency, superior charge carrier transport properties, and excellent electrical and optical performance of UV LED devices made from such

coalesced film structures. The presence of negligible levels of defects and dislocations is unprecedented for any AlGaN film structures grown on sapphire substrate (lattice mismatch ~13-16%) [258]. Such a remarkable achievement is attributed to the use of: i) small size GaN nanowires to eliminate the propagation of dislocations from the underlying substrate, ii) selective area epitaxy to achieve a precise control of nanowire size, position, and orientation, iii) gradual and controllable coalescence to suppress the formation of dislocations, and iv) quasi 3-D surface structure to further relax strain and prevent dislocation and crack formation. As demonstrated in this work, high efficiency planar deep UV photonic devices, including LEDs, lasers, and photodetectors can be achieved by using such a unique nanowire-based architecture on virtually any substrate. Moreover, this concept can be extended for the scaled up manufacturing of large-area, dislocation-free semipolar GaN, AlN, and/or AlGaN free-standing templates/substrates that were not previously possible.

Chapter 6: Ultralow Threshold GaN/AlGaN Nanowire Edge Emitting Ultraviolet Lasers

6.1. Introduction

In this Chapter, we will investigate the epitaxial growth, fabrication, and characterization of AlGaN nanowire semiconductor lasers that can operate in the UV spectral range. GaN-based semiconductor ultraviolet lasers are of tremendous importance for applications in lighting, display, water purification, disinfection, chemical and biochemical sensors, and medical diagnostics. To date, the performance of GaN-based lasers degrades considerably with increasing Al content, i.e. decreasing operation wavelength. For example, the currently reported Ga(Al)N UV edge emitting lasers generally exhibit threshold current density ~10 kA/cm^2, or higher [78, 79, 196, 198, 199]. The shortest wavelength that has ever been reported for such edge emitting lasers is ~336 nm [199]. The poor performance of such devices is fundamentally limited by the presence of large densities of defects and dislocations, the strong polarization fields, and the inefficient *p*-doping in AlGaN materials (see Section 1.1.2). Recently, with the use of nanowire structures, high efficiency light emitting diodes and lasers have been demonstrated in the visible range. Nanowire structures can offer several fundamental advantages, including low defect density, much reduced strain-induced polarization fields, and significantly enhanced dopant incorporation (see Section 1.2.2). However, the realization of efficient nanowire lasers in the UV wavelength range has been very limited. Previous studies generally focus on single wire devices under optical pumping [259-263]. For practical applications, it is of significant interest in developing electrically injected edge

emitting lasers by using such defect-free nanowire structures. It is also highly desirable that such devices can be grown directly on low cost, large area substrates such as Si.

To realize nanowire edge emitting lasers, any optical scattering loss related to variations of nanowire size, density, and spacing should be substantially reduced. Therefore, the epitaxial growth and structural properties of such nanowire arrays need to be carefully controlled and engineered. In the conventional nanowire formation process, III-nitride nanowire arrays generally exhibit random distribution in position and a high degree of non-uniformity in size and height distribution (see Section 2.2.2). As discussed in Section 2.3, such issues can be well-addressed by using SAG technique. To date, however, an electrically injected semiconductor nanowire laser with the selective area growth process has not been demonstrated. In addition, the direct formation of high quality AlGaN nanowires by this growth process has remained elusive.

In this work, we have performed a detailed investigation of large-area GaN/AlGaN nanowire arrays using SAG technique on *n*-GaN template on sapphire substrate. Such nanowire structures exhibit nearly identical size distribution and strong PL emission in the wavelength rang of ~370 nm. The nanowire arrays are then fabricated into edge emitting lasers. The devices exhibit ultralow threshold current (~10 mA) under continuous wave operation at room-temperature. The spectral linewidth is as narrow as ~0.2 nm. Detailed polarization measurements further confirm the emission is predominantly TE polarized, further confirming the achievement of lasing. This is the first demonstration of electrically injected semiconductor lasers with the use of selectively area grown nanowire arrays. The laser threshold current is nearly 2 orders of magnitude lower, compared to conventional GaN quantum well lasers in this wavelength range [79, 264, 265]. The measured laser threshold also compares favorably with the threshold power (~120 kW/cm^2) of single GaN nanowire devices under optical pumping [260, 266].

6.2. GaN/AlGaN Nanowire Edge Emitting Laser by Selective Area Growth and Device Fabrication

The selective area growth takes place on *n*-GaN templates on sapphire by using a thin Ti layer (~10 nm) as the growth mask. Nanoscale patterns with a hole diameter of 300 nm and a center-to-center spacing of 400 nm arranged in a rectangular lattice were created using standard e-beam lithography and reactive ion etching techniques. Sizes of the nanohole arrays were varied in the range of tens to hundreds of μm for the fabrication of large area nanowire edge emitting lasers. Prior to loading into the growth chamber, the patterns were carefully cleaned by standard solvents. The Ti layer was nitridized in the reaction chamber at ~400ºC. Subsequently, vertically aligned GaN/$Al_xGa_{1-x}N$ (x = ~0.1‑0.15) nanowire arrays were grown using a Veeco Gen-II plasma-assisted MBE system. Illustrated in the inset of Figure 6-1a, from bottom to top the device heterostructure consists of *n*-Ga contact, *n*-AlGaN, MQWs active region, *p*-AlGaN, and *p*-GaN contact layers. Five GaN (2 nm) /AlGaN (4 nm) QWs are incorporated as the gain medium. The growth conditions of GaN/AlGaN MQW nanowire structures include the following steps. *n*-type GaN nanowire arrays were first grown with a substrate temperature of ~920°C, a nitrogen flow rate of 0.3 sccm, a RF plasma forward power of 350 W, and a Ga beam flux of ~3.69×10^{-7} Torr. Subsequently, the *n*- and *p*-type $Al_xGa_{1-x}N$ cladding and guiding layers were grown at substrate temperature of 940°C, and Ga and Al beam fluxes of ~3.7×10^{-7} Torr and ~2.1×10^{-8} Torr, ~8.4×10^{-9} Torr, respectively. The MQWs active layer sandwiched between the *n*- and *p*-type guiding layers was grown with a nitrogen flow rate of 0.3 sccm, substrate temperature of 920°C, Ga and Al beam fluxes of ~3.71×10^{-7} Torr and ~8.4×10^{-9} Torr, respectively. The nanowire edge emitting laser is illustrated in Figure 6-1a. During the growth of AlGaN nanowire segment, the lateral growth is significantly enhanced, leading to increased nanowire diameter and very small air gap amongst

nanowires. Shown in Figure 6-1b is a SEM image of the nanowire arrays. It is seen that the nanowires exhibit a high level of size uniformity. Due to the small air gap between adjacent nanowires, optical scattering loss can be substantially reduced. Optical properties of the AlGaN MQW nanowires were subsequently studied by using temperature-dependent PL spectroscopy associated with a closed-loop liquid helium compressor. The nanowires exhibit strong PL emission in the wavelength rang of ~370 nm at room-temperature as shown in Figure 6-1c. The nanowire edge emitting laser fabrication process includes the following steps. At first, to create clean contact-nanowire interfaces, the devices were chemically treated by *h*ydrochloric acid for 30 s immediately preceding metal evaporation. Then Ni(20 nm)/Au(100 nm) and Ti(20 nm)/Au (100 nm) metal layers were deposited on the nanowire top surfaces and *n*-GaN template to serve as *p*- and *n*-metal contacts, respectively. Subsequently, an annealing process at 550 ºC was performed in N_2 ambient for 1 min. The nanowire laser facets were then carefully polished by focused ion beam etching to remove any surface roughness and to enhance reflectivity. Multiple pairs of SiO_2/air distributed Bragg reflectors (DBRs) were then deposited near the front and back facets, schematically shown in Figure 6-1a. Illustrated in Figure 6-1d., a SEM image of the fabricated laser device together with the presence of DBRs.

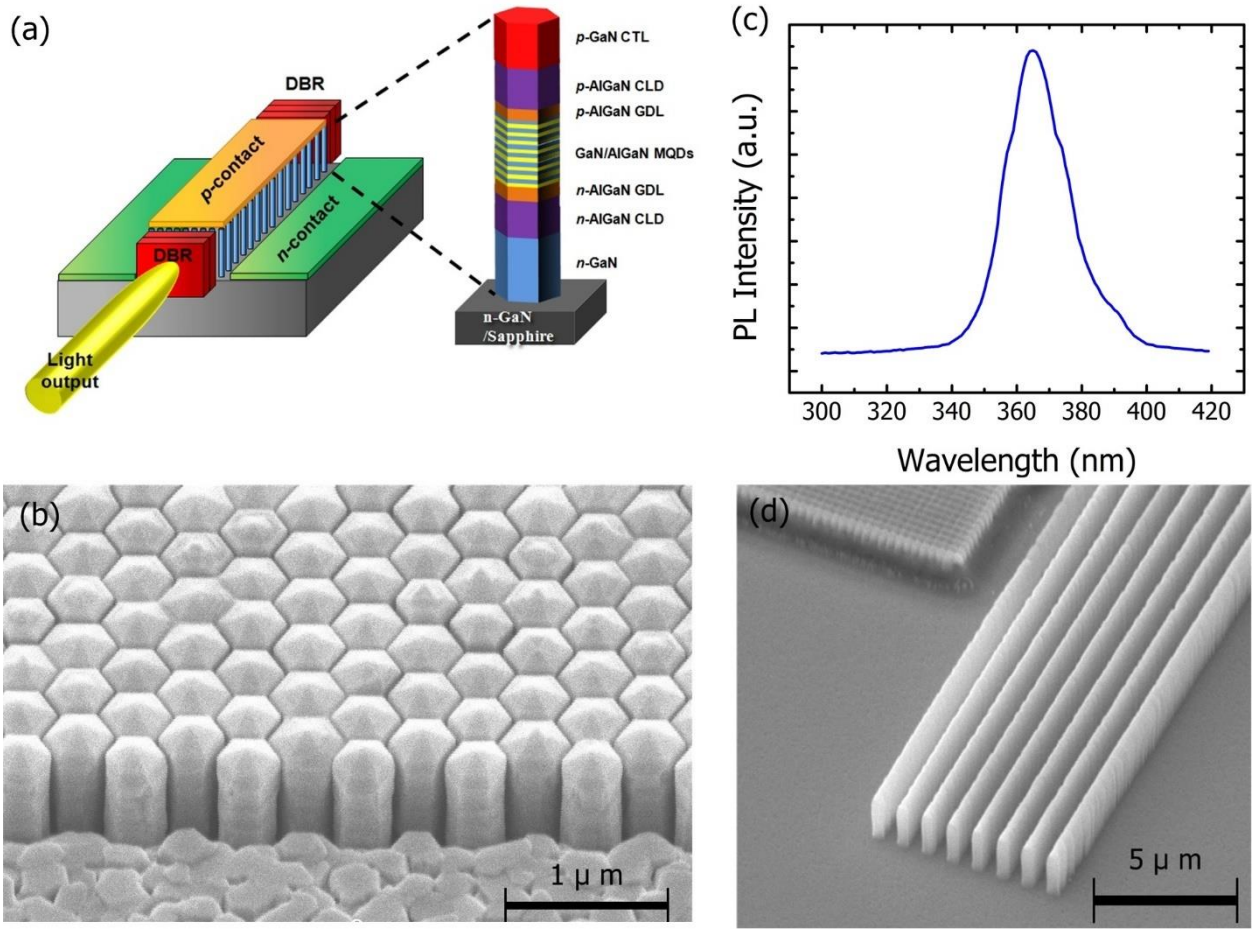

Figure 6-1: (a) Schematic illustrations of GaN/$Al_xGa_{1-x}N$ MQW nanowire heterostructures grown on sapphire substrate and complete edge emtting laser device. (b) A SEM image of SAG MQW nanowire heterostructures on Ti mask pre-patterned substrate. (c) Room-temperature PL spectrum of nanowire heterostructures. (d) SiO2/Air Distributed Bragg reflectors.

6.3. Device Characterization and Discussion

The fabricated nanowire edge emitting lasers exhibit relatively good I-V characteristics. Illustrated in Figure 6-2a is the I-V curve measured at room-temperature. The device shows a relatively low turn on voltage of ~3.5 V and exhibit small leakage current under reverse bias (inset of Figure 6-2a). Room-temperature EL spectra were collected using an optical fiber and analyzed by a high resolution spectrometer equipped with a photomultiplier tube (PMT).

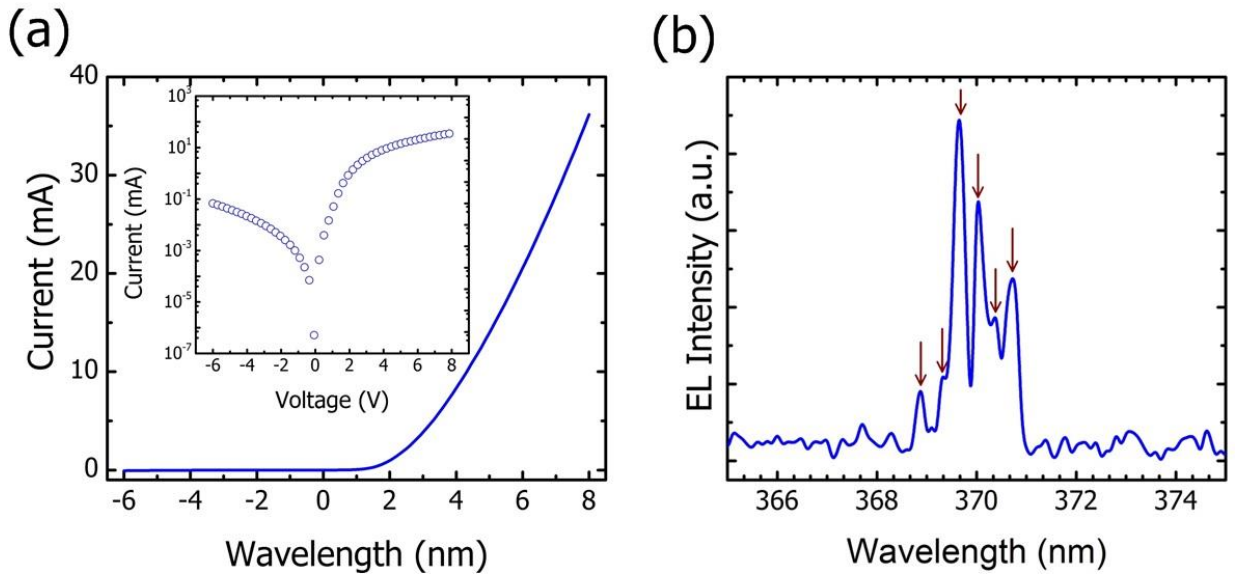

Figure 6-2: (a) I-V characteristics measured at room-temperature of GaN/$Al_xGa_{1-x}N$ MQWs nanowire-based laser device. Inset: I-V characteristics of the device under forward and reserve bias in a semi-log scale. (b) Fabry-Pérot modes measured under CW biasing conditions at room-temperature.

Shown in Figure 6-2b, the presence of multiple resonance modes can be clearly measured. The mode spacing is estimated to be ~0.3 nm. The light-current characteristics are plotted in Figure 6-3a. A threshold of ~10.6 mA can be clearly measured, which is 2 orders of magnitude lower, compared to conventional GaN quantum well lasers in this wavelength range [79, 264, 265]. The significantly reduced threshold current is directly related to the nearly defect-free AlGaN nanowire heterostructures, the core-shell nanowire arrays with negligible surface recombination, and the reduced optical scattering loss in regular nanowire arrays. The output spectra below and above threshold are shown Figure 6-3b. Below threshold, a broad spontaneous emission spectrum is measured. At 1.3×I_{th}, the device emission is dominated by a single emission peak, superimposed on the broad emission background. The spectral linewidth is very narrow, ~0.2 nm, shown in the inset of Figure 6-3b.

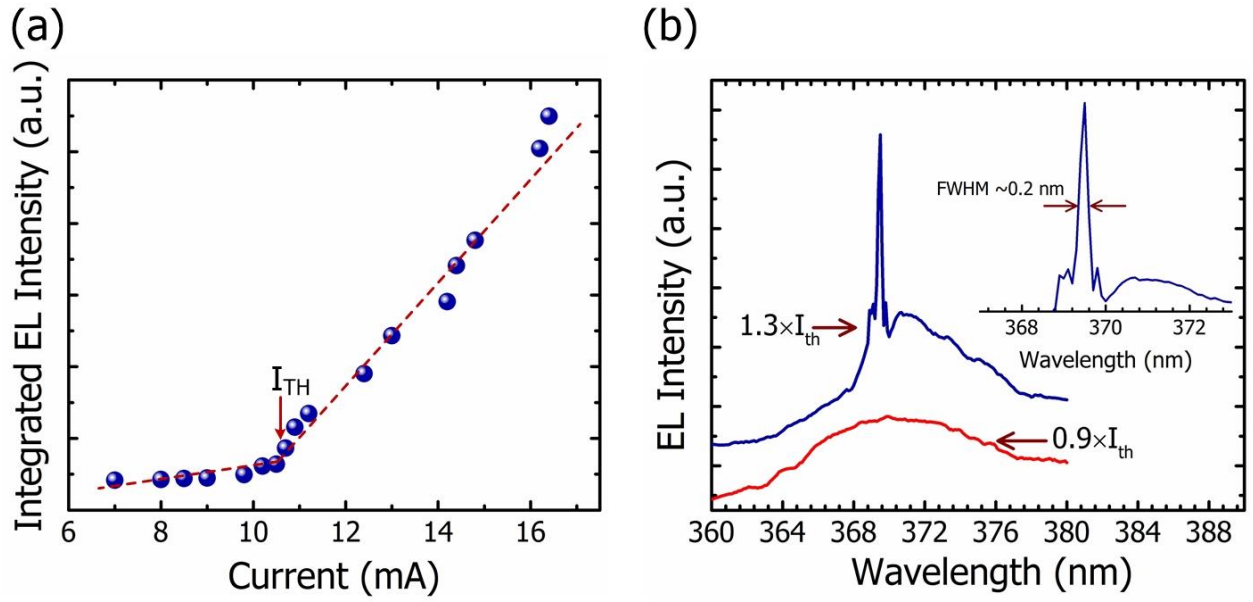

Figure 6-3: (a) Integrated light intensity as a function of injection current characteristics of nanowire-based edge emitting laser. Red arrow indicates the threshold current density. (b) Electroluminescence spectra below (red) and above (blue) threshold current. Inset: spectral linewidth ~0.2 nm.

In order to further confirm the achievement of lasing, the polarization properties of the emission were measured and analyzed. The measurement configuration is illustrated in the inset of Figure 6-4. The device emission shows clearly TE polarization. No emission peaks can be measured in the TM polarization configuration.

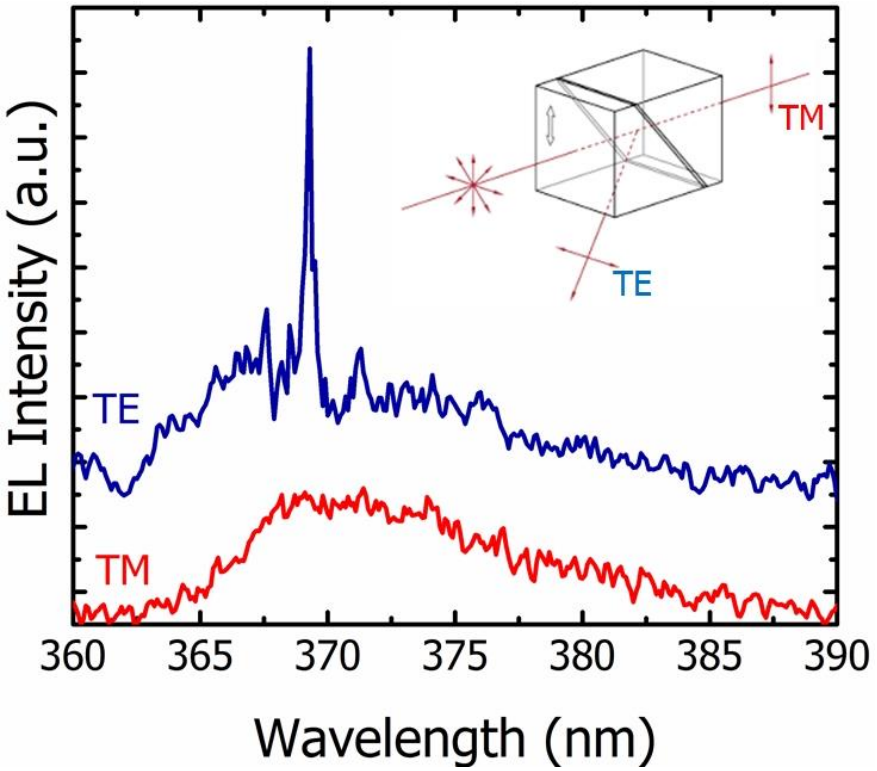

Figure 6-4: TE- and TM-polarized electroluminescence emission spectra acquired at room temperature under continuous wave bias.

6.4. Conclusion

In summary, we have demonstrated an electrically injected semiconductor edge emitting laser by utilizing the selective area growth of AlGaN nanowire arrays. The device threshold current density is substantially reduced, compared to the conventional edge emitting lasers in this wavelength range. The device performance can be further improved by optimizing the nanowire configuration and the DBR pairs. More importantly, such nanowire arrays provide a unique approach for achieving semiconductor edge emitting lasers in the UV-B and UV-C bands that were not previously possible. This work also bridges the gap between conventional single nanowire devices and large area edge emitting lasers often required for practical applications.

Chapter 7: Conclusion and Future Work

7.1. Summary of the Thesis Work

The work presented in this thesis includes the development of superior quality InN and AlGaN nanowires and their applications including LEDs and lasers operating in the deep UV to the near-infrared spectral range. In what follows, we briefly summarize the major achievements of this thesis.

Due to the narrow bandgap (~0.65 eV) and extremely large electron mobility (~10,000 $cm^2/V \cdot s$ at room-temperature), InN nanowires have emerged as a promising candidate for infrared optoelectronic and high-speed devices. However, the realization of any practical devices *prior to* this thesis work is not possible which is mainly due to the poor material quality with large background electron concentration and surface electron accumulation, limiting the achievement of direct *p*-type conduction. In this thesis work, we have demonstrated, for the first time, *p*-type conduction and electroluminescence emission of InN. We report on the observation of ambipolar transport characteristics of InN:Mg nanowires at room-temperature, providing unambiguous evidence that the Fermi level is fundamentally unpinned on the grown surfaces of InN. We also report on the achievement of electroluminescence emission of single InN *p-i-n* nanowire devices. Electroluminescence emission with a peak energy of 0.71 eV (1.75 μm) was observed at 77 K. The measurement of near-bandgap electroluminescence provides unambiguous evidence for the achievement of *p*-type conduction of InN.

Secondly, we have also demonstrated $Al_xGa_{1-x}N$ nanowire arrays grown by SAG approach with Ti mask. The luminescence peak emission of the AlGaN nanowires grown by SAG technique can be tuned from 327 nm to 210 nm, covering the entire ultraviolet spectral range. The AlGaN

DUV LEDs operating at 279 nm exhibit excellent optical and electrical performance. By further utilizing the advantages of SAG $Al_xGa_{1-x}N$ nanowire arrays, we have also demonstrated that nearly dislocation-free semipolar AlGaN templates can be achieved on *c*-plane sapphire substrate through controlled nanowire coalescence by selective-area epitaxy. The coalesced Mg-doped AlGaN layers exhibit superior charge carrier transport properties at room-temperature. The semipolar AlGaN UV LEDs demonstrate excellent optical and electrical performance. This work establishes the use of engineered nanowire structures as a viable architecture to achieve large-area, dislocation-free planar photonic and electronic devices. This unique concept will also enable the scaled up manufacturing of large-area, low-cost semipolar/nonpolar GaN and/or AlN templates/substrates. We have further demonstrated, for the first time, an electrically injected nanowire edge-emitting lasers operating in the UV spectral range.

7.2. Suggested Future Work

The goal of this thesis is to develop a fundamental understanding and practical exploration of the emerging III-nitride nanomaterials by optimizing the device epitaxial growth, fabrication and characterization. Described below, for the future work, we aim to have a thorough understanding of the epitaxy and characteristics of AlGaN quantum-confined nanostructures and demonstrate high power DUV semiconductor lasers, including edge and surface emitting lasers that can operate in the UV-B and UV-C bands.

7.2.1. AlGaN Dot-In-Nanowire Heterostructure

As presented in Chapters 4 & 5, we have successfully demonstrated UV and DUV AlGaN LEDs by utilizing the selective area growth of AlGaN nanowire arrays. Recently, with the use of dot-in-nanowire structures, high efficiency LEDs have been demonstrated in the visible range

[140, 267]. The development of AlGaN dot-in-nanowire structure utilizing SAG technique will provide a unique approach for achieving high power LEDs with emission wavelengths in the UV-B (280 nm – 315 nm) and UV-C (< 280 nm) bands that were not previously possible. Shown in the Figure 7-1 is a schematic plot of the nanowire-based devices fabricated from proposed AlGaN dot-in-nanowire structures. There are certain challenges that need to be overcome, such as, device instability, short lifetime, doping inefficiency which results in high resistance, crystal quality as well as low output power. Those challenges require further optimization of the growth parameters as well as structural design and device fabrication process. For example, the number of dots in nanowire structure, nanoscale pattern design, etc. are of great importance to improve carrier confinement and minimize light scattering, which will significantly enhance light extraction efficiency. By increasing lateral growth rate during epitaxial process, the nanowire spacing can be drastically reduced from tens of nm to few nm due to increased nanowire diameter, resulting in significant reduction of light scattering. Such nanowire arrays can also be designed as edge emitting lasers.

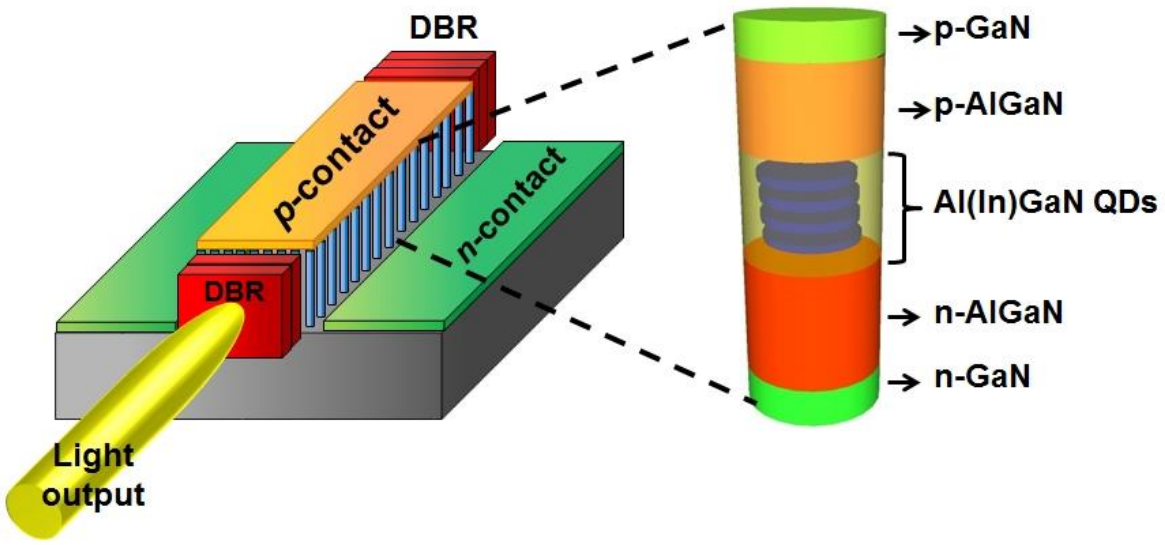

Figure 7-1: Schematic illustration of AlGaN dot-in-nanowire based devices by selective area growth approach.

7.2.2. AlGaN Nanowall Deep UV LEDs and Lasers

We have recently demonstrated that significantly enhanced Mg-dopant incorporation and efficient *p*-type conduction can be achieved in low dimensional nanostructures, such as nanowires [221, 222]. We have further demonstrated AlN nanowire LEDs operating at 210 nm with excellent electrical efficiency [145, 146]. However, the device performance including output power is severely limited by the lack of transparent *p*-metal contact layer and the unique TM polarization of light emission from AlN [143, 174, 252, 268]. In this regard, we propose to investigate the molecular beam epitaxy, and structural, electrical and optical characterization of Al(Ga)N nanowall structures grown on sapphire substrate.

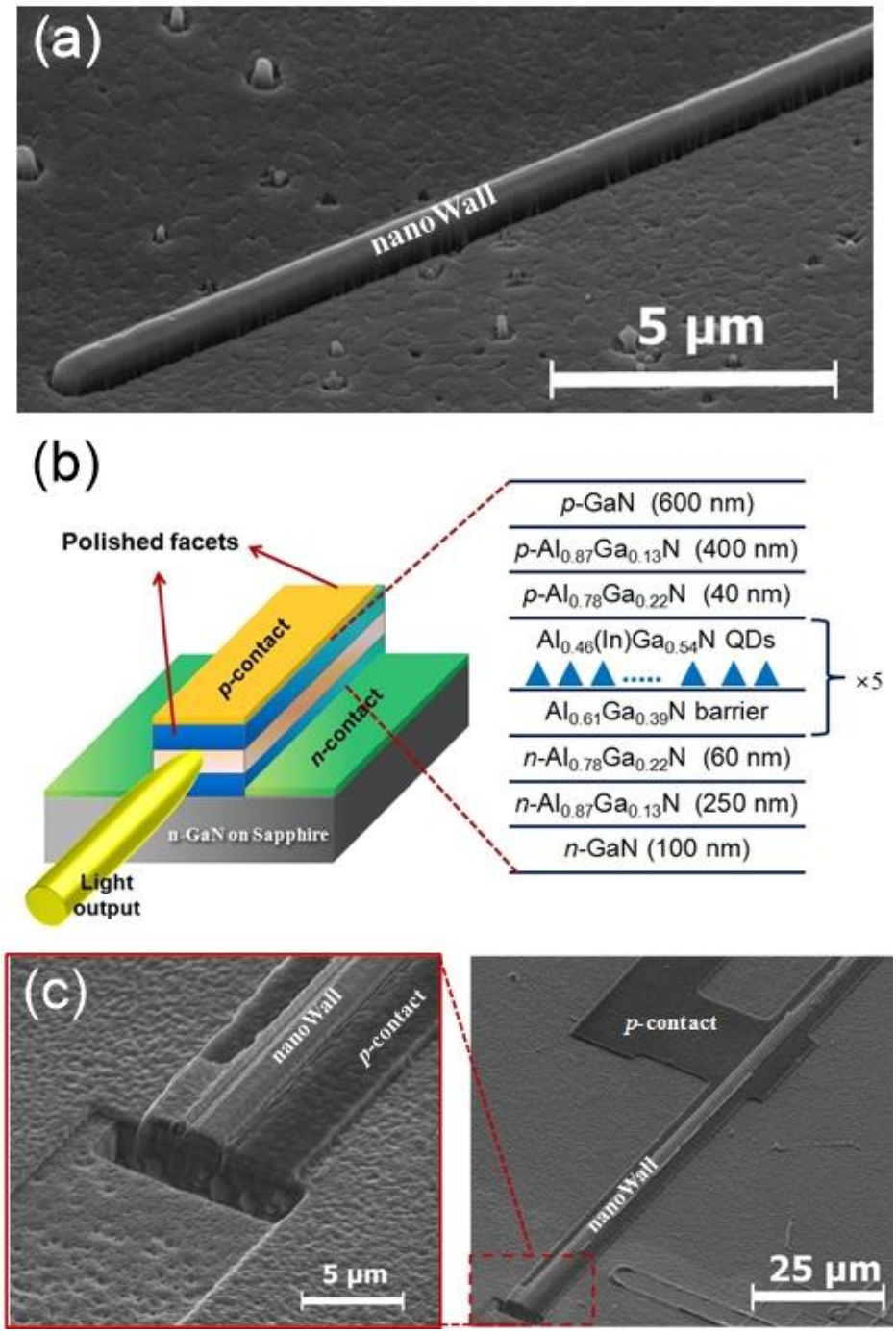

Figure 7-2: (a) A SEM image of nanowall heterostructures grown on pre-patterned sapphire substrate by MBE. (b) Schematic illustration of GaN/$Al_xGa_{1-x}N$ nanowall based devices. (c) A SEM image of fabricated nanowall based devices.

In this work, GaN or AlN template on sapphire substrate will be firstly patterned with top-down approach, including electron beam lithography and dry etching. The widths of the etched stripe patterns can be varied from tens of nm to hundreds of nm. Subsequently, AlGaN heterostructures will be grown using the epitaxy conditions developed for AlGaN nanowires described in this thesis as presented in Figure 7-2a. Illustrated in Figures 7-2b and 7-2c are the schematic plot of the proposed AlGaN nanowall based edge emitting laser and a SEM image of a fabricated device, respectively. Compared to nanowires, such nanowall structures can be readily fabricated into large area devices without the use of any surface passivation or planarization. More importantly, the TM polarized emission can be efficiently extracted from the lateral surfaces. Moreover, such nanowall structures can be designed as edge-emitting lasers with significantly improved power operation, compared to nanowire devices.

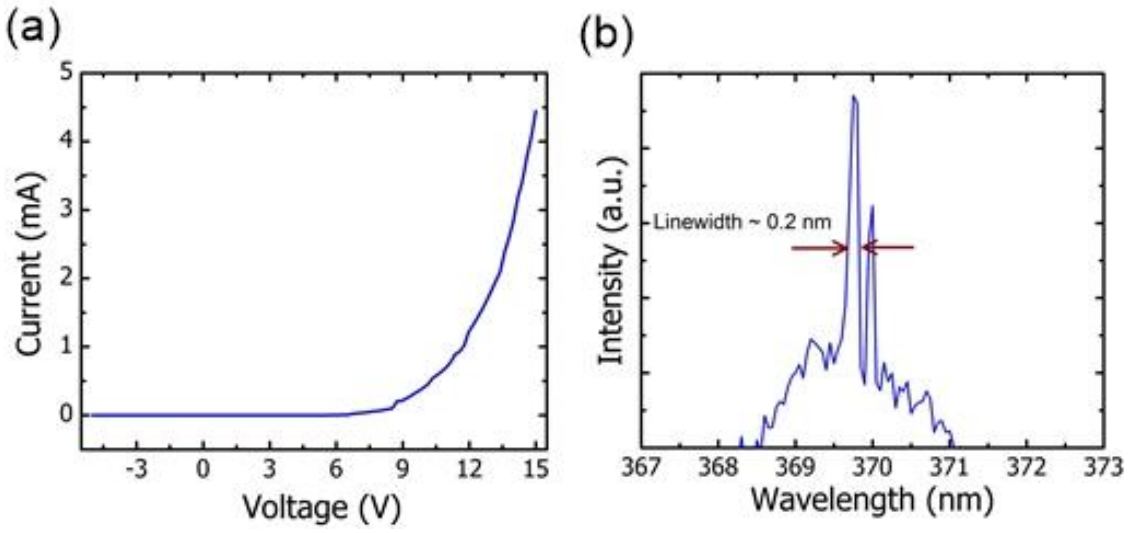

Figure 7-3: (a) Current-voltage characteristics of AlGaN nanowall based devices. (b) Room-temperature EL spectrum with injection current of 0.5 mA. Spectral linewidth of ~0.2 nm.

The fabricated nanowall edge emitting lasers exhibit relatively good I-V characteristics. Illustrated in Figure 7-3a is the I-V curve of a nanowall based edge emitting laser measured at

room-temperature. The device shows a turn on voltage of ~6.5 V and exhibits small leakage current under reverse bias. Room-temperature EL spectra were collected using an optical fiber and analyzed by a high resolution spectrometer equipped with a photomultiplier tube (PMT). As seen the devices exhibit a lasing spectrum at 369.6 nm with a narrow linewidth of ~0.2 nm under an injection current of 500 μA.

7.2.3. Electrically Injected Ultraviolet Plasmonic Stripe Laser

We also propose to develop low threshold plasmonic Al(Ga)N lasers operating in the deep UV spectral range, schematically illustrated in Figure 7-4. To date, the size reduction of photonic components down to nanometer scale, for example, nano-LEDs and nano-lasers, is highly desirable for current communication and computation technologies. However, diffraction limit of light when the dimensions of optical components approach the wavelength of light severely limits the fabrication process. One of the most promising methods to address these challenges is to utilize surface plasmons, which is able to confine light to very small dimensions at the interface of metal-dielectric [200, 269-272]. To date, little attention has been paid to plasmonic laser operating in DUV range which is mainly due to the bottleneck of achieving high quality nanoscale structures and metal layer, which limits surface plasmons coupling efficiency. In this context, we will investigate the MBE growth, fabrication, and characterization AlGaN nanowall/stripe based plasmonic lasers. The structure consists of an epitaxial Al layer, and AlN/AlGaN nanowall/stripe heterostructures as the gain media. Devices under both optical pumping and electrical injection will be realized. In addition, stripe plasmonic lasers will be demonstrated to achieve high output power. These laser devices can be individually addressed and can be designed as suitable light sources for future high resolution projection systems. Shown in Figure 7-4 is the demonstration of electrical injected UV plasmonic stripe laser with some preliminary results.

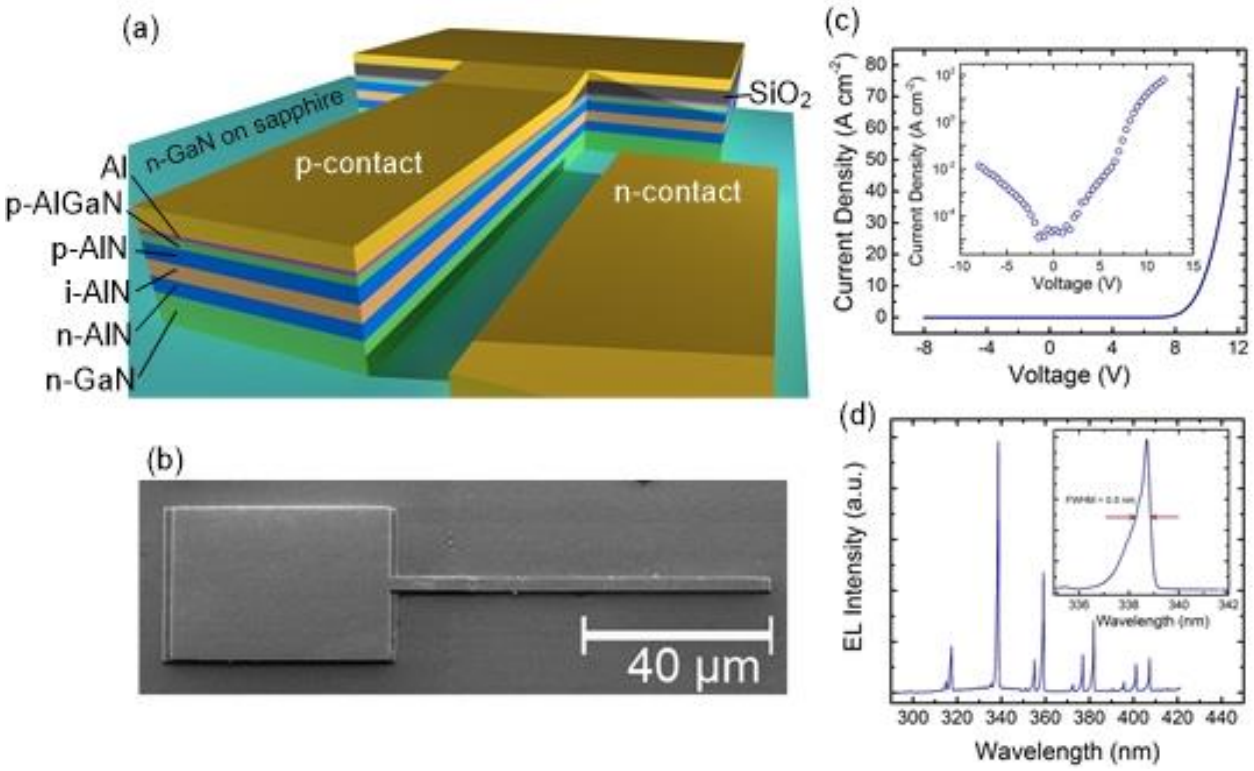

Figure 7-4: (a) Schematic illustration of AlN/AlGaN stripe plasmonic laser operating in UV range. (b) A SEM image of as-grown AlN/AlGaN stripe. (c) I-V characteristics of stripe laser. (d) Room-temperature EL spectrum of stripe laser measured under continuous wave condition. Spectral linewidth ~ 0.5 nm.

List of Publications And Copyrights

Referred and Archival Journal Publications

1. B. H. Le, S. Zhao, X. Liu, S. Y. Woo, G. A. Botton and Z. Mi, "Controlled Coalescence of AlGaN Nanowire Arrays: An Architecture for Dislocation-Free Planar Ultraviolet Photonic Device Applications", *Advanced Materials*, DOI: 10.1002/adma.201602645, 2016.
2. B. H. Le, X. Liu, S. Y. Woo, S. Zhao, G. A. Botton and Z. Mi, " Ultraviolet GaN/AlGaN Heterostructure Light Emitting Diode Operating at 279 nm by Selective Area Epitaxial Growth", 2016 (under preparation).
3. B. H. Le, X. Liu, , S. Zhao, N. H. Tran, and Z. Mi, "Electrically Injected Ultraviolet AlGaN Plasmonic Stripe Lasers", 2016 (under preparation).
4. N. H. Tran, B. H. Le, S. Zhao, and Z. Mi*, "On the Mechanism of Highly Efficiency p-Type Conduction of Mg-doped Ultra-Wide-Bandgap AlN Nanostructures", 2016 (accepted to *Appl. Phys. Lett.*).
5. B. H. Le, S. Zhao, N. H. Tran, T. Szkopek, and Z. Mi, "On the Fermi-level pinning of InN grown surfaces," *Applied Physics Express*, vol. 8, p. 061001, 2015.
6. B. H. Le, S. Zhao, N. H. Tran, and Z. Mi, "Electrically injected near-infrared light emission from single InN nanowire *p-i-n* diode," *Applied Physics Letters*, vol. 105, p. 231124, 2014.
7. S. Zhao, A. Connie, B. H. Le, X. Kong, H. Guo, X. Du, *et al.*, "p-Type AlN nanowires and AlN nanowire light emitting diodes on Si," in *Summer Topicals Meeting Series (SUM), 2015*, 2015, pp. 131-132.

8. S. Zhao, Z. Mi, and B. H. Le, "p-Type InN nanowires: towards ultrahigh speed nanoelectronics and nanophotonics," in *SPIE OPTO*, 2014, pp. 898617-898617-7.

9. Z. Mi, S. Zhao, B. H. Le, O. Salehzadeh, S. Alagha, K. L. Kavanagh, and S. P. Watkins, "Molecular beam epitaxy growth and characterization of intrinsic and p-type InN" Proc. SPIE 8996, doi:10.1117/12.2038663, 2014.

10. S. Zhao, B. H. Le, D. Liu, X. Liu, M. Kibria, T. Szkopek, *et al.*, "p-Type InN Nanowires," *Nano letters*, vol. 13, pp. 5509-5513, 2013.

11. N. Hong Tran, B. H. Le, S. Fan, S. Zhao, Z. Mi, B. A. Schmidt, *et al.*, "Optical and structural characterization of nitrogen-rich InN: Transition from nearly intrinsic to strongly n-type degenerate with temperature," *Applied Physics Letters*, vol. 103, p. 262101, 2013.

12. A. Shih, S. Fathololoumi, S. Zhao, B. H. Le, H. P. T. Nguyen, I. Shih, *et al.*, "Negative Differential Resistance in GaN/AlN Heterostructure Nanowires," *Journal ISSN*, vol. 1929, p. 1248, 2012.

Conference/Meeting Presentations (Oral)

1. B. H. Le, S. Zhao, X. Liu, S. Y. Woo, G. A. Botton and Z. Mi , "Controlled Coalescence of AlGaN Nanowire Arrays: An Architecture for Dislocation-Free Planar Ultraviolet Photonic Device Applications", 32nd North American Molecular Beam Epitaxy Conference (NAMBE) Saratoga Springs, New York, 2016.

2. A. Pofelski, S. Y. Woo, B. H. Le, X. Liu, S. Zhao, Z. Mi, G. A. Botton, "Strain at Coalescence of Patterned (Al)GaN Nanorod Arrays Formed by Selective Area Growth for Optoelectronic Devices, 2016.

3. D. A. Laleyan, S. Zhao, B. H. Le, N. H. Tran, and Z. Mi, "AlN/BN Nanowire Heterostructures for High Efficiency Deep Ultraviolet Photonics", 58th Electronic Materials Conference, Delaware, 2016.
4. B. H. Le, S. Zhao, X. Liu, Y. H. Ra, M. Djavid, and Z. Mi, "Electrically Injected GaN/AlGaN Nanowire Ultraviolet Lasers by Selective Area Growth", 31st North American Molecular Beam Epitaxy Conference (NAMBE), Mexico, 2015.
5. B. H. Le, S. Zhao, N. H. Tran, T. Szkopek, and Z. Mi, "Demonstration of p-type InN Nanowires: Electrical Transport Properties and Near-infrared Electroluminescence Emission", 57th Electronic Materials Conference, Ohio State University, 2015.
6. B. H. Le, S. Zhao, N. H. Tran, T. Szkopek, and Z. Mi, "Mg-doped InN nanowires: p-Type conduction and ambipolar behaviors", 18th International Conference on Molecular Beam Epitaxy, Arizona, 2014.

Poster presentations

1. B. H. Le, X. Liu, S. Zhao, K. H. Li and Z. Mi, "Application of $Al_xGa_{1-x}N$/AlN nanowire heterostructures in ultraviolet absorption coefficient measurement of wood fibre networks", 2nd FIBRE Conference, UBC, Vancouver, British Columbia.
2. B. H. Le, S. Zhao, A. Connie and Z. Mi, "Application of $Al_xGa_{1-x}N$/AlN nanowire heterostructures in ultraviolet absorption coefficient measurement of wood fibre networks", Green Fibre Network Semi-Annual Meeting, May 2014, L'Esterel, Quebec.
3. B. H. Le, N. H. Tran, H. P. T. Nguyen, and Z Mi, "Current-Voltage Characteristics of Single InGaN/GaN Nanowire LEDs", 10th International Conference on Nitride Semiconductors, August 25-30, 2013, Washington, D.C.

4. B. H. Le, N. H. Tran, H. P. T. Nguyen, and Z Mi, "InGaN/GaN Dot-in-a-Wire Intermediate-Band Solar Cell Devices", 30th North American Molecular Beam Epitaxy Conference (NAMBE), Banff, Alberta, 2013.
5. N. H. Tran, B. H Le, S. Zhao, Z. Mi, and K. S. A. Butcher, "Unusual Photoluminescence Emission at ~0.68 eV from Nonstoichiometric InN:N", The 16th Canadian Semiconductor Science and Technology Conference (CSSTC), Lakehead University, Thunder Bay, Ontario, 2013.
6. B. H. Le, and Z. Mi, "Application of broadband InN nanowire-based infrared spectroscopy in Nanocrystalline Cellulose moisture analysis", Green Fibre Network Semi-Annual Meeting, May 2013, the Nav Centre, Cornwall, Ontario.
7. B. H. Le, Q. Wang, S. Zhao and Z. Mi, "Application of AlxGa1-xN Nanowire Heterostructures in Ultraviolet Absorption Coefficient Measurement of Wood Fibre Networks", Green Fibre Network Semi-Annual Meeting, October 23 – 25, 2013, Fredericton.
8. B. H. Le, S. Fathololoumi, S. Zhao, Z. Mi, "Broadband InN nanowire-based infrared spectroscopy for nanoscale moisture detection in Wood Fibre Networks", Green Fibre Network Semi-Annual Meeting, May 1-3, 2012, the Nav Centre, Cornwall, Ontario.
9. B. H. Le, S. Fathololoumi, S. Zhao, Z. Mi, "Broadband Infrared Spectroscopy for Nanoscale Analysis of Water Vapour in Wood Fibre Networks", Vancouver, November 13 – 15, 2012, FPInnovations, 3800 Westbrook Mall, UBC.

Awards

1. Best poster presentation award with title “Broadband InN nanowire-based infrared spectroscopy for nanoscale moisture detection in Wood Fibre Networks” at Semi–annual Green Fibre meeting, Vancouver, November 13 – 15, 2012, FPInnovations, 3800 Westbrook Mall, UBC.
2. Best student presentation award for oral presentation “Mg-doped InN Nanowires: P-type Conduction and Ambipolar Behaviors”, 18th International Conference on Molecular Beam Epitaxy, Arizona, 2014.

References

[1] J. Wu, "When group-III nitrides go infrared: New properties and perspectives," *J. Appl. Phys.*, vol. 106, p. 011101, 2009.

[2] A. G. Bhuiyan, A. Hashimoto, and A. Yamamoto, "Indium nitride (InN): A review on growth, characterization, and properties," *J. Appl. Phys.*, vol. 94, p. 2779, 2003.

[3] S. Strite and H. Morkoç, "GaN, AlN, and InN: a review," *J. Vac. Sci. & Tech. B*, vol. 10, pp. 1237-1266, 1992.

[4] S. K. O'Leary, B. E. Foutz, M. S. Shur, and L. F. Eastman, "Steady-state and transient electron transport within the III–V nitride semiconductors, GaN, AlN, and InN: a review," *J. Mater. Sci.: Materials in Electronics*, vol. 17, pp. 87-126, 2006.

[5] C.-Y. Chang, G.-C. Chi, W.-M. Wang, L.-C. Chen, K.-H. Chen, F. Ren, *et al.*, "Electrical transport properties of single GaN and InN nanowires," *J. Elec. Mater.*, vol. 35, pp. 738-743, 2006.

[6] W. Walukiewicz, J. W. Ager, K. M. Yu, Z. Liliental-Weber, J. Wu, S. X. Li, *et al.*, "Structure and electronic properties of InN and In-rich group III-nitride alloys," *J. Phys. D: Appl. Phys.*, vol. 39, pp. R83-R99, 2006.

[7] F. Ponce and D. Bour, "Nitride-based semiconductors for blue and green light-emitting devices," *Nature*, vol. 386, pp. 351-359, 1997.

[8] M. H. Crawford, "LEDs for solid-state lighting: performance challenges and recent advances," *Selected Topics in Quantum Electronics, IEEE Journal of*, vol. 15, pp. 1028-1040, 2009.

[9] S. Nakamura, T. Mukai, and M. Senoh, "Candela-class high-brightness InGaN/AlGaN double-heterostructure blue-light-emitting diodes," *Appl. Phys. Lett.*, vol. 64, pp. 1687-1689, 1994.

[10] S. Nakamura, M. Senoh, N. Iwasa, and S.-i. Nagahama, "High-brightness InGaN blue, green and yellow light-emitting diodes with quantum well structures," *Japanese J. Appl. Phys. Part 2 Letters*, Vol. 34, Pp. L797-L797, 1995.

[11] S. Nakamura, M. Senoh, N. Iwasa, S.-i. Nagahama, T. Yamada, and T. Mukai, "Superbright green InGaN single-quantum-well-structure light-emitting diodes," *Japanese J. Appl. Phys.*, vol. 34, p. L1332, 1995.

[12] F. Hide, P. Kozodoy, S. P. DenBaars, and A. J. Heeger, "White light from InGaN/conjugated polymer hybrid light-emitting diodes," *Appl. Phys. Lett.*, vol. 70, pp. 2664-2666, 1997.

[13] S. Nakamura, "The roles of structural imperfections in InGaN-based blue light-emitting diodes and laser diodes," *Science*, vol. 281, pp. 956-961, 1998.

[14] T. Mukai, M. Yamada, and S. Nakamura, "Characteristics of InGaN-based UV/blue/green/amber/red light-emitting diodes," *Japanese J. Appl. Phys.*, vol. 38, p. 3976, 1999.

[15] W. Wong, T. Sands, N. Cheung, M. Kneissl, D. Bour, P. Mei, *et al.*, "Fabrication of thin-film InGaN light-emitting diode membranes by laser lift-off," *Appl. Phys. Lett.*, vol. 75, pp. 1360-1362, 1999.

[16] J. Wierer, M. Krames, J. Epler, N. Gardner, M. Craford, J. Wendt, *et al.*, "InGaN/GaN quantum-well heterostructure light-emitting diodes employing photonic crystal structures," *Appl. Phys. Lett.*, vol. 84, pp. 3885-3887, 2004.

[17] S. Nakamura, M. Senoh, S.-i. Nagahama, N. Iwasa, T. Yamada, T. Matsushita, *et al.*, "InGaN multi-quantum-well-structure laser diodes with cleaved mirror cavity facets," *J Japanese J. Appl. Phys.*, vol. 35, p. L217, 1996.

[18] S. Nakamura, M. Senoh, S.-i. Nagahama, N. Iwasa, T. Yamada, T. Matsushita, *et al.*, "Room-temperature continuous-wave operation of InGaN multi-quantum-well structure laser diodes with a lifetime of 27 hours," *Appl. Phys. Lett.*, vol. 70, pp. 1417-1419, 1997.

[19] Y. Narukawa, Y. Kawakami, M. Funato, S. Fujita, S. Fujita, and S. Nakamura, "Role of self-formed InGaN quantum dots for exciton localization in the purple laser diode emitting at 420 nm," *Appl. Phys. Lett.*, vol. 70, pp. 981-983, 1997.
[20] S. Nakamura, M. Senoh, S. i. Nagahama, N. Iwasa, T. Yamada, T. Matsushita, *et al.*, "InGaN/GaN/AlGaN-based laser diodes with modulation-doped strained-layer superlattices grown on an epitaxially laterally overgrown GaN substrate," *Appl. Phys. Lett.*, vol. 72, pp. 211-213, 1998.
[21] F. Della Sala, A. Di Carlo, P. Lugli, F. Bernardini, V. Fiorentini, R. Scholz, *et al.*, "Free-carrier screening of polarization fields in wurtzite GaN/InGaN laser structures," *Appl. Phys. Lett.*, vol. 74, pp. 2002-2004, 1999.
[22] S. Nakamura, S. Pearton, and G. Fasol, *The blue laser diode: the complete story*: Springer, 2000.
[23] D. Queren, A. Avramescu, G. Brüderl, A. Breidenassel, M. Schillgalies, S. Lutgen, *et al.*, "500 nm electrically driven InGaN based laser diodes," *Appl. Phys. Lett.*, vol. 94, p. 081119, 2009.
[24] A. Osinsky, S. Gangopadhyay, R. Gaska, B. Williams, M. A. Khan, D. Kuksenkov, *et al.*, "Low noise p-π-n GaN ultraviolet photodetectors," *Appl. Phys. Lett.*, vol. 71, pp. 2334-2336, 1997.
[25] F. Binet, J. Duboz, E. Rosencher, F. Scholz, and V. Härle, "Mechanisms of recombination in GaN photodetectors," *Appl. Phys. Lett.*, vol. 69, pp. 1202-1204, 1996.
[26] G. Xu, A. Salvador, W. Kim, Z. Fan, C. Lu, H. Tang, *et al.*, "High speed, low noise ultraviolet photodetectors based on GaN pin and AlGaN (p)-GaN (i)-GaN (n) structures," *Appl. Phys. Lett.*, vol. 71, pp. 2154-2156, 1997.
[27] E. Miyazaki, S. Itami, and T. Araki, "Using a light-emitting diode as a high-speed, wavelength selective photodetector," *Review of scientific instruments*, vol. 69, pp. 3751-3754, 1998.
[28] J. Wu, W. Walukiewicz, K. Yu, W. Shan, J. Ager Iii, E. Haller, *et al.*, "Superior radiation resistance of In1− xGaxN alloys: Full-solar-spectrum photovoltaic material system," *J. Appl. Phys.*, vol. 94, pp. 6477-6482, 2003.
[29] O. Jani, I. Ferguson, C. Honsberg, and S. Kurtz, "Design and characterization of GaN∕InGaN solar cells," *Appl. Phys. Lett.*, vol. 91, p. 132117, 2007.
[30] C. J. Neufeld, N. G. Toledo, S. C. Cruz, M. Iza, S. P. DenBaars, and U. K. Mishra, "High quantum efficiency InGaN/GaN solar cells with 2.95 eV band gap," *Appl. Phys. Lett.*, vol. 93, pp. 143502-143502-3, 2008.
[31] X. Zheng, R.-H. Horng, D.-S. Wuu, M.-T. Chu, W.-Y. Liao, M.-H. Wu, *et al.*, "High-quality InGaN/GaN heterojunctions and their photovoltaic effects," *Appl. Phys. Lett.*, vol. 93, pp. 261108-261108-3, 2008.
[32] M. A. Khan, A. Bhattarai, J. Kuznia, and D. Olson, "High electron mobility transistor based on a GaN-AlxGa1− xN heterojunction," *Appl. Phys. Lett.*, vol. 63, pp. 1214-1215, 1993.
[33] M. A. Khan, J. Kuznia, D. Olson, W. Schaff, J. Burm, and M. Shur, "Microwave performance of a 0.25 μm gate AlGaN/GaN heterostructure field effect transistor," *Appl. Phys. Lett.*, vol. 65, pp. 1121-1123, 1994.
[34] Y. Zhang and J. Singh, "Charge control and mobility studies for an AlGaN/GaN high electron mobility transistor," *J. Appl. Phys.*, vol. 85, pp. 587-594, 1999.
[35] M. A. Khan, X. Hu, G. Sumin, A. Lunev, J. Yang, R. Gaska, *et al.*, "AlGaN/GaN metal oxide semiconductor heterostructure field effect transistor," *Electron Device Letters, IEEE*, vol. 21, pp. 63-65, 2000.
[36] J. L. Pau, J. Anduaga, C. Rivera, Á. Navarro, I. Álava, M. Redondo, *et al.*, "Optical sensors based on III-nitride photodetectors for flame sensing and combustion monitoring," *Appl. Optics*, vol. 45, pp. 7498-7503, 2006.
[37] S.-J. Chang, T. Ko, Y.-K. Su, Y.-Z. Chiou, C. Chang, S.-C. Shei, *et al.*, "GaN-based pin sensors with ITO contacts," *Sensors Journal, IEEE*, vol. 6, pp. 406-411, 2006.
[38] Y. Su, S. Chang, C. Chen, J. Chen, G. Chi, J. Sheu, *et al.*, "GaN metal-semiconductor-metal ultraviolet sensors with various contact electrodes," *Sensors Journal, IEEE*, vol. 2, pp. 366-371, 2002.

[39] T. Tansley and C. Foley, "Optical band gap of indium nitride," *J. Appl. Phys.*, vol. 59, pp. 3241-3244, 1986.
[40] T. Matsuoka, H. Okamoto, M. Nakao, H. Harima, and E. Kurimoto, "Optical bandgap energy of wurtzite InN," *Appl. Phys. Lett.*, vol. 81, p. 1246, 2002.
[41] J. Wu, W. Walukiewicz, K. Yu, J. W. Ager, E. Haller, H. Lu, *et al.*, "Unusual properties of the fundamental band gap of InN," *Appl. Phys. Lett.*, vol. 80, pp. 3967-3969, 2002.
[42] V. Y. Davydov, A. Klochikhin, R. Seisyan, V. Emtsev, S. Ivanov, F. Bechstedt, *et al.*, "Absorption and emission of hexagonal InN. Evidence of narrow fundamental band gap," *Phys. Stat. Sol. (b)*, vol. 229, pp. r1-r3, 2002.
[43] Y. L. Chang, F. Li, A. Fatehi, and Z. Mi, "Molecular beam epitaxial growth and characterization of non-tapered InN nanowires on Si(111)," *Nanotechnology*, vol. 20, p. 345203, Aug 26 2009.
[44] J. Wu, W. Walukiewicz, W. Shan, K. Yu, J. Ager, S. Li, *et al.*, "Temperature dependence of the fundamental band gap of InN," *J. Appl. Phys.*, vol. 94, pp. 4457-4460, 2003.
[45] J. Wu, W. Walukiewicz, W. Shan, K. Yu, J. Ager III, E. Haller, *et al.*, "Effects of the narrow band gap on the properties of InN," *Phys. Rev. B*, vol. 66, p. 201403, 2002.
[46] X. Wang, S. Liu, N. Ma, L. Feng, G. Chen, F. Xu, *et al.*, "High-electron-mobility InN layers grown by boundary-temperature-controlled epitaxy," *Appl. Phys. Exp.*, vol. 5, p. 5502, 2012.
[47] S. Wang, H. Liu, B. Gao, and H. Cai, "Monte Carlo calculation of electron diffusion coefficient in wurtzite indium nitride," *Appl. Phys. Lett.*, vol. 100, p. 142105, 2012.
[48] S. Zhao, "Molecular beam epitaxial growth characterization and nanophotonic device applications of InN nanowires on Si platform," PhD thesis, 2013.
[49] J. N. Chris G. Van de Walle, "Universal alignment of hydrogen levels in semiconductors, insulators and solutions," *Nature*, vol. 423, 2003.
[50] I. Mahboob, T. Veal, L. Piper, C. McConville, H. Lu, W. Schaff, *et al.*, "Origin of electron accumulation at wurtzite InN surfaces," *Phys. Rev. B*, vol. 69, p. 201307, 2004.
[51] E. Calleja, J. Grandal, M. Sánchez-García, M. Niebelschütz, V. Cimalla, and O. Ambacher, "Evidence of electron accumulation at nonpolar surfaces of InN nanocolumns," *Appl. Phys. Lett.*, vol. 90, p. 262110, 2007.
[52] A. Yoshikawa, X. Wang, Y. Ishitani, and A. Uedono, "Recent advances and challenges for successful p-type control of InN films with Mg acceptor doping by molecular beam epitaxy," *Phys. Stat. Sol. (a)*, vol. 207, pp. 1011-1023, 2010.
[53] T. Richter, H. Luth, T. Schapers, R. Meijers, K. Jeganathan, S. Estevez Hernandez, *et al.*, "Electrical transport properties of single undoped and n-type doped InN nanowires," *Nanotechnology*, vol. 20, p. 405206, Oct 7 2009.
[54] C. Van de Walle, J. Lyons, and A. Janotti, "Controlling the conductivity of InN," *Phys. Stat. Sol. (a)*, vol. 207, pp. 1024-1036, 2010.
[55] C.-T. Kuo, S.-C. Lin, K.-K. Chang, H.-W. Shiu, L.-Y. Chang, C.-H. Chen, *et al.*, "Is electron accumulation universal at InN polar surfaces?," *Appl. Phys. Lett.*, vol. 98, p. 052101, 2011.
[56] T. D. Veal, I. Mahboob, L. F. J. Piper, C. F. McConville, H. Lu, and W. J. Schaff, "Indium nitride: Evidence of electron accumulation," *J. Vac. Sci. & Tech. B: Microelectronics and Nanometer Structures*, vol. 22, p. 2175, 2004.
[57] C. G. Van de Walle and D. Segev, "Microscopic origins of surface states on nitride surfaces," *J. Appl. Phys.*, vol. 101, p. 081704, 2007.
[58] I. Mahboob, T. Veal, C. McConville, H. Lu, and W. Schaff, "Intrinsic Electron Accumulation at Clean InN Surfaces," *Phys. Rev. Lett.*, vol. 92, 2004.
[59] T. Stoica, R. J. Meijers, R. Calarco, T. Richter, E. Sutter, and H. Lüth, "Photoluminescence and intrinsic properties of MBE-grown InN nanowires," *Nano Lett.*, vol. 6, pp. 1541-1547, 2006.
[60] C.-H. Shen, H.-Y. Chen, H.-W. Lin, S. Gwo, A. Klochikhin, and V. Y. Davydov, "Near-infrared photoluminescence from vertical InN nanorod arrays grown on silicon: Effects of surface electron accumulation layer," *Appl. Phys. Lett.*, vol. 88, pp. 253104-253104-3, 2006.

[61] P. King, T. D. Veal, C. F. McConville, F. Fuchs, J. Furthmuller, F. Bechstedt, *et al.*, "Universality of electron accumulation at wurtzite< equation> c</equation>-and< equation> a</equation>-plane and zinc-blende InN surfaces," *Appl. Phys. Lett.*, vol. 91, pp. 092101-092101-3, 2007.
[62] C.-L. Wu, H.-M. Lee, C.-T. Kuo, C.-H. Chen, and S. Gwo, "Absence of Fermi-level pinning at cleaved nonpolar InN surfaces," *Phys. Rev. Lett.*, vol. 101, p. 106803, 2008.
[63] H. Eisele and P. Ebert, "Non-polar group-III nitride semiconductor surfaces," *Phys. Stat. Sol. (RRL)-Rapid Research Letters*, vol. 6, pp. 359-369, 2012.
[64] P. Ebert, S. Schaafhausen, A. Lenz, A. Sabitova, L. Ivanova, M. Dähne, *et al.*, "Direct measurement of the band gap and Fermi level position at InN (112¯ 0)," *Appl. Phys. Lett.*, vol. 98, p. 062103, 2011.
[65] A. Mayevsky and G. G. Rogatsky, "Mitochondrial function in vivo evaluated by NADH fluorescence: from animal models to human studies," *American journal of physiology-Cell physiology*, vol. 292, pp. C615-C640, 2007.
[66] K. B. A. T. K. Asif Khan, "Ultraviolet light-emitting diodes based on group three nitrides," *Nat. Photo.*, 2008.
[67] H. Hirayama, S. Fujikawa, N. Noguchi, J. Norimatsu, T. Takano, K. Tsubaki, *et al.*, "222-282 nm AlGaN and InAlGaN-based deep-UV LEDs fabricated on high-quality AlN on sapphire," *Phys. Stat. Sol. (a)*, vol. 206, pp. 1176-1182, 2009.
[68] M. A. Khan, M. Shatalov, H. Maruska, H. Wang, and E. Kuokstis, "III–nitride UV devices," *Japanese J. Appl. Phys.*, vol. 44, p. 7191, 2005.
[69] A. Khan, K. Balakrishnan, and T. Katona, "Ultraviolet light-emitting diodes based on group three nitrides," *Nat. Photon.*, vol. 2, pp. 77-84, 2008.
[70] X. Hu, J. Deng, J. P. Zhang, A. Lunev, Y. Bilenko, T. Katona, *et al.*, "Deep ultraviolet light-emitting diodes," *Phys. Stat. Sol. (a)*, vol. 203, pp. 1815-1818, 2006.
[71] H. Hirayama, S. Fujikawa, N. Noguchi, J. Norimatsu, T. Takano, K. Tsubaki, *et al.*, "222–282 nm AlGaN and InAlGaN-based deep-UV LEDs fabricated on high-quality AlN on sapphire," *Phys. Stat. Sol. (a)*, vol. 206, pp. 1176-1182, 2009.
[72] Y. Muramoto, M. Kimura, and S. Nouda, "Development and future of ultraviolet light-emitting diodes: UV-LED will replace the UV lamp," *Semi. Sci. and Technology*, vol. 29, p. 084004, 2014.
[73] C. Pernot, M. Kim, S. Fukahori, T. Inazu, T. Fujita, Y. Nagasawa, *et al.*, "Improved efficiency of 255–280 nm AlGaN-based light-emitting diodes," *Appl. Phys. Exp.*, vol. 3, p. 061004, 2010.
[74] P. Dong, J. Yan, J. Wang, Y. Zhang, C. Geng, T. Wei, *et al.*, "282-nm AlGaN-based deep ultraviolet light-emitting diodes with improved performance on nano-patterned sapphire substrates," *App. Phys. Lett.*, vol. 102, p. 241113, 2013.
[75] H. Hirayama, N. Maeda, S. Fujikawa, S. Toyoda, and N. Kamata, "Recent progress and future prospects of AlGaN-based high-efficiency deep-ultraviolet light-emitting diodes," *Japanese J. Appl. Phys.*, vol. 53, p. 100209, 2014.
[76] Y. Taniyasu, M. Kasu, and T. Makimoto, "An aluminium nitride light-emitting diode with a wavelength of 210 nanometres," *Nature*, vol. 441, pp. 325-328, 2006.
[77] A. Bhattacharyya, T. Moustakas, L. Zhou, D. J. Smith, and W. Hug, "Deep ultraviolet emitting AlGaN quantum wells with high internal quantum efficiency," *App. Phys. Lett.*, vol. 94, p. 181907, 2009.
[78] H. Yoshida, M. Kuwabara, Y. Yamashita, K. Uchiyama, and H. Kan, "The current status of ultraviolet laser diodes," *Phys. Stat. Sol. (a)*, vol. 208, pp. 1586-1589, 2011.
[79] M. Kneissl, Z. Yang, M. Teepe, C. Knollenberg, O. Schmidt, P. Kiesel, *et al.*, "Ultraviolet semiconductor laser diodes on bulk AlN," *J. Appl. Phys.*, vol. 101, p. 123103, 2007.
[80] K. Takeda, F. Mori, Y. Ogiso, T. Ichikawa, K. Nonaka, M. Iwaya, *et al.*, "Internal quantum efficiency of GaN/AlGaN-based multi quantum wells on different dislocation densities underlying layers," *Phys. Stat. Sol. (c)*, vol. 7, pp. 1916-1918, 2010.

[81] K. Ban, J.-i. Yamamoto, K. Takeda, K. Ide, M. Iwaya, T. Takeuchi, *et al.*, "Internal quantum efficiency of whole-composition-range AlGaN multiquantum wells," *Appl. Phys. Exp.*, vol. 4, p. 052101, 2011.
[82] S. Kamiyama, M. Iwaya, N. Hayashi, T. Takeuchi, H. Amano, I. Akasaki, *et al.*, "Low-temperature-deposited AlGaN interlayer for improvement of AlGaN/GaN heterostructure," *J. Crys.Growth*, vol. 223, pp. 83-91, 2001.
[83] J. Han, K. Waldrip, S. R. Lee, J. J. Figiel, S. Hearne, G. A. Petersen, *et al.*, "Control and elimination of cracking of AlGaN using low-temperature AlGaN interlayers," *Appl. Phys. Lett.*, vol. 78, pp. 67-69, 2001.
[84] B. Haskell, T. Baker, M. McLaurin, F. Wu, P. Fini, S. DenBaars, *et al.*, "Defect reduction in (View Record in Scopus| Full Text via CrossRef 1 100) m-plane gallium nitride via lateral epitaxial overgrowth by hydride vapor phase epitaxy," *Appl. Phys. Lett.*, vol. 86, p. 111917, 2005.
[85] T. Kawashima, T. Nagai, D. Iida, A. Miura, Y. Okadome, Y. Tsuchiya, *et al.*, "Reduction in defect density over whole area of (1$\ bar 1 $00) m-plane GaN using one-sidewall seeded epitaxial lateral overgrowth," *Phys. Stat. Sol. (b)*, vol. 244, pp. 1848-1852, 2007.
[86] X. Ni, Ü. Özgür, Y. Fu, N. Biyikli, J. Xie, A. Baski, *et al.*, "Defect reduction in (112¯ 0) a-plane GaN by two-stage epitaxial lateral overgrowth," *Appl. Phys. Lett.*, vol. 89, p. 262105, 2006.
[87] B. M. Imer, F. Wu, S. P. DenBaars, and J. S. Speck, "Improved quality (11 (2) over-bar0) a-plane GaN with sidewall lateral epitaxial overgrowth," *Appl. Phys. Lett.*, vol. 88, 2006.
[88] M. Craven, S. Lim, F. Wu, J. Speck, and S. DenBaars, "Threading dislocation reduction via laterally overgrown nonpolar (1120) a-plane GaN," *Appl. Phys. Lett.*, vol. 81, pp. 1201-1203, 2002.
[89] S. Rosner, G. Girolami, H. Marchand, P. Fini, J. Ibbetson, L. Zhao, *et al.*, "Cathodoluminescence mapping of epitaxial lateral overgrowth in gallium nitride," *Appl. Phys. Lett.*, vol. 74, pp. 2035-2037, 1999.
[90] I. Kidoguchi, A. Ishibashi, G. Sugahara, and Y. Ban, "Air-bridged lateral epitaxial overgrowth of GaN thin films," *Appl. Phys. Lett.*, vol. 76, pp. 3768-3770, 2000.
[91] T.-Y. Tang, C.-H. Lin, Y.-S. Chen, W.-Y. Shiao, W.-M. Chang, C.-H. Liao, *et al.*, "Nitride nanocolumns for the development of light-emitting diode," *IEEE Transactions on Electron Devices*, vol. 57, pp. 71-78, 2010.
[92] T. Kinoshita, T. Obata, H. Yanagi, and S.-i. Inoue, "High p-type conduction in high-Al content Mg-doped AlGaN," *Appl. Phys. Lett.*, vol. 102, p. 012105, 2013.
[93] K. Kumakura, T. Makimoto, and N. Kobayashi, "Mg-acceptor activation mechanism and transport characteristics in p-type InGaN grown by metalorganic vapor phase epitaxy," *J. Appl. Phys.*, vol. 93, p. 3370, 2003.
[94] X. Wang, S.-B. Che, Y. Ishitani, and A. Yoshikawa, "Hole mobility in Mg-doped p-type InN films," *Appl. Phys. Lett.*, vol. 92, p. 132108, 2008.
[95] C. G. Van de Walle and J. Neugebauer, "First-principles calculations for defects and impurities: Applications to III-nitrides," *J. Appl. Phys.*, vol. 95, pp. 3851-3879, 2004.
[96] P. Kozodoy, H. Xing, S. P. DenBaars, U. K. Mishra, A. Saxler, R. Perrin, *et al.*, "Heavy doping effects in Mg-doped GaN," *J. Appl. Phys.*, vol. 87, pp. 1832-1835, 2000.
[97] C. Stampfl and C. G. Van de Walle, "Doping of AlxGa1− xN," *Appl. Phys. Lett*, vol. 72, pp. 459-461, 1998.
[98] M. Katsuragawa, S. Sota, M. Komori, C. Anbe, T. Takeuchi, H. Sakai, *et al.*, "Thermal ionization energy of Si and Mg in AlGaN," *J. Crys. Growth*, vol. 189, pp. 528-531, 1998.
[99] M. Kibria, S. Zhao, F. Chowdhury, Q. Wang, H. Nguyen, M. Trudeau, *et al.*, "Tuning the surface Fermi level on p-type gallium nitride nanowires for efficient overall water splitting," *Nat. Com.*, vol. 5, 2014.
[100] C.-C. Pan, S. Tanaka, F. Wu, Y. Zhao, J. S. Speck, S. Nakamura, *et al.*, "High-power, low-efficiency-droop semipolar (2021) single-quantum-well blue light-emitting diodes," *App. Phys. Exp.*, vol. 5, p. 062103, 2012.

[101] J. Mickevičius, E. Kuokštis, V. Liuolia, G. Tamulaitis, M. Shur, J. Yang, *et al.*, "Photoluminescence dynamics of AlGaN quantum wells with built-in electric fields and localized states," *Phys. Stat. Sol. (a)*, vol. 207, pp. 423-427, 2010.
[102] R. Langer, J. Simon, V. Ortiz, N. Pelekanos, A. Barski, R. Andre, *et al.*, "Giant electric fields in unstrained GaN single quantum wells," *Appl. Phys. Lett.*, vol. 74, pp. 3827-3829, 1999.
[103] J. S. Im, H. Kollmer, J. Off, A. Sohmer, F. Scholz, and A. Hangleiter, "Reduction of oscillator strength due to piezoelectric fields in G a N/A $l_xGa_{1-x}N$ quantum wells," *Phys. Rev. B*, vol. 57, p. R9435, 1998.
[104] T. F. Kent, S. D. Carnevale, A. Sarwar, P. J. Phillips, R. F. Klie, and R. C. Myers, "Deep ultraviolet emitting polarization induced nanowire light emitting diodes with $Al_xGa_{1-x}N$ active regions," *Nanotechnology*, vol. 25, p. 455201, 2014.
[105] K. Nam, J. Li, M. Nakarmi, J. Lin, and H. Jiang, "Unique optical properties of AlGaN alloys and related ultraviolet emitters," *Appl. Phys. Lett.*, vol. 84, pp. 5264-5266, 2004.
[106] J. Li, K. Nam, M. Nakarmi, J. Lin, H. Jiang, P. Carrier, *et al.*, "Band structure and fundamental optical transitions in wurtzite AlN," *Appl. Phys. Lett.*, vol. 83, pp. 5163-5165, 2003.
[107] M. Kneissl, T. Kolbe, C. Chua, V. Kueller, N. Lobo, J. Stellmach, *et al.*, "Advances in group III-nitride-based deep UV light-emitting diode technology," *Semicond. Sci. Technol.*, vol. 26, p. 014036, 2010.
[108] J. Ristić, E. Calleja, S. Fernández-Garrido, L. Cerutti, A. Trampert, U. Jahn, *et al.*, "On the mechanisms of spontaneous growth of III-nitride nanocolumns by plasma-assisted molecular beam epitaxy," *J. Crys. Growth*, vol. 310, pp. 4035-4045, 2008.
[109] E. Calleja, J. Ristić, S. Fernández-Garrido, L. Cerutti, M. Sánchez-García, J. Grandal, *et al.*, "Growth, morphology, and structural properties of group-III-nitride nanocolumns and nanodisks," *Phys. Stat. Sol. (b)*, vol. 244, pp. 2816-2837, 2007.
[110] I. Shalish, G. Seryogin, W. Yi, J. Bao, M. A. Zimmler, E. Likovich, *et al.*, "Epitaxial catalyst-free growth of InN nanorods on c-plane sapphire," *Nanoscale Res. Lett.*, vol. 4, p. 532, 2009.
[111] S. Zhao, M. Kibria, Q. Wang, H. Nguyen, and Z. Mi, "Growth of large-scale vertically aligned GaN nanowires and their heterostructures with high uniformity on SiO x by catalyst-free molecular beam epitaxy," *Nanoscale*, vol. 5, pp. 5283-5287, 2013.
[112] N. A. S. Kris A. Bertness, and Albert V. Davydov, "GaN Nanowires Grown by Molecular Beam Epitaxy," *IEEE J. Selected Topics In Quantum Electronics*, 2011.
[113] T. Stoica, R. Meijers, R. Calarco, T. Richter, and H. Lüth, "MBE growth optimization of InN nanowires," *J. Crys. Growth*, vol. 290, pp. 241-247, 2006.
[114] T. Stoica, E. Sutter, R. J. Meijers, R. K. Debnath, R. Calarco, H. Lüth, *et al.*, "Interface and Wetting Layer Effect on the Catalyst-Free Nucleation and Growth of GaN Nanowires," *Small*, vol. 4, pp. 751-754, 2008.
[115] C. Chao, J.-I. Chyi, C. Hsiao, C. Kei, S. Kuo, H.-S. Chang, *et al.*, "Catalyst-free growth of indium nitride nanorods by chemical-beam epitaxy," *Appl. Phys. Lett.*, vol. 88, p. 233111, 2006.
[116] G. Cheng, E. Stern, D. Turner-Evans, and M. A. Reed, "Electronic properties of InN nanowires," *Appl. Phys. Lett.*, vol. 87, p. 253103, 2005.
[117] C.-Y. Chang, G.-C. Chi, W.-M. Wang, L.-C. Chen, K.-H. Chen, F. Ren, *et al.*, "Transport properties of InN nanowires," *Appl. Phys. Lett.*, vol. 87, p. 093112, 2005.
[118] F. Werner, F. Limbach, M. Carsten, C. Denker, J. Malindretos, and A. Rizzi, "Electrical conductivity of InN nanowires and the influence of the native indium oxide formed at their surface," *Nano Lett.*, vol. 9, pp. 1567-1571, 2009.
[119] J. Grandal, M. Sánchez-García, E. Calleja, E. Luna, and A. Trampert, "Accommodation mechanism of InN nanocolumns grown on Si (111) substrates by molecular beam epitaxy," *Appl. Phys. Lett.*, vol. 91, p. 021902, 2007.
[120] Y.-L. Chang, Z. Mi, and F. Li, "Photoluminescence Properties of a Nearly Intrinsic Single InN Nanowire," *Adv. Func. Mater.*, vol. 20, pp. 4146-4151, 2010.

[121] S. Zhao, S. Fathololoumi, K. H. Bevan, D. P. Liu, M. G. Kibria, Q. Li, *et al.*, "Tuning the surface charge properties of epitaxial InN nanowires," *Nano Lett.*, vol. 12, pp. 2877-82, Jun 13 2012.
[122] S. Zhao, Z. Mi, M. Kibria, Q. Li, and G. Wang, "Understanding the role of Si doping on surface charge and optical properties: Photoluminescence study of intrinsic and Si-doped InN nanowires," *Phys. Rev. B*, vol. 85, p. 245313, 2012.
[123] S. Zhao, O. Salehzadeh, S. Alagha, K. Kavanagh, S. Watkins, and Z. Mi, "Probing the electrical transport properties of intrinsic InN nanowires," *Appl. Phys. Lett.*, vol. 102, pp. 073102-073102-5, 2013.
[124] W. Lin, S. Li, and J. Kang, "Near-ultraviolet light emitting diodes using strained ultrathin InN/GaN quantum well grown by metal organic vapor phase epitaxy," *Appl. Phys. Lett.*, vol. 96, p. 101115, 2010.
[125] G. Wu, G. Du, F. Gao, H. Wang, C. Shen, and W. Li, "Near-infrared electroluminescence emission from an n-InN nanodots/p-Si heterojunction structure," *J. Phys. D: Appl. Phys.*, vol. 45, p. 215102, 2012.
[126] J. Chen, G. Cheng, E. Stern, M. A. Reed, and P. Avouris, "Electrically excited infrared emission from InN nanowire transistors," *Nano Lett.*, vol. 7, pp. 2276-2280, 2007.
[127] K. Kishino, J. Kamimura, and K. Kamiyama, "Near-Infrared InGaN Nanocolumn Light-Emitting Diodes Operated at 1.46 μm," *Appl. Phys. Exp.*, vol. 5, p. 031001, 2012.
[128] R. Jones, K. Yu, S. Li, W. Walukiewicz, J. Ager, E. Haller, *et al.*, "Evidence for p-type doping of InN," *Phys. Rev. Lett.*, vol. 96, p. 125505, 2006.
[129] J. Wang, G. Tang, X. Wu, and M. Gu, "InN doped with Zn: Bulk and surface investigation from first principles," *Sol. Stat. Com.*, vol. 152, pp. 1168-1171, 2012.
[130] M.-Y. Xie, N. B. Sedrine, S. Schöche, T. Hofmann, M. Schubert, L. Hung, *et al.*, "Effect of Mg doping on the structural and free-charge carrier properties of InN films," *J. Appl. Phys.*, vol. 115, p. 163504, 2014.
[131] L. Dmowski, M. Baj, X. Wang, X. Zheng, D. Ma, L. Kończewicz, *et al.*, "Advantage of In-over N-polarity for disclosure of p-type conduction in InN: Mg," *J. Appl. Phys.*, vol. 115, p. 173704, 2014.
[132] J. H. Chai, Y. W. Song, R. J. Reeves, and S. M. Durbin, "Optical and electrical characteristics of Mn-doped InN grown by plasma-assisted molecular beam epitaxy," *Phys. Stat. Sol. (a)*, vol. 209, pp. 95-99, 2012.
[133] K. Wang, N. Miller, R. Iwamoto, T. Yamaguchi, M. Mayer, T. Araki, *et al.*, "Mg doped InN and confirmation of free holes in InN," *App. Phys. Lett.*, vol. 98, pp. 042104-042104-3, 2011.
[134] N. Miller, J. Ager, H. Smith, M. Mayer, K. Yu, E. Haller, *et al.*, "Hole transport and photoluminescence in Mg-doped InN," *J. Appl. Phys.*, vol. 107, pp. 113712-113712-8, 2010.
[135] N. Ma, X. Wang, S. Liu, G. Chen, J. Pan, L. Feng, *et al.*, "Hole mobility in wurtzite InN," *App. Phys. Lett.*, vol. 98, pp. 192114-192114-3, 2011.
[136] D. Segev and C. G. Van de Walle, "Origins of Fermi-level pinning on GaN and InN polar and nonpolar surfaces," *EPL (Europhysics Letters)*, vol. 76, p. 305, 2006.
[137] S. Zhao, B. Le, D. Liu, X. Liu, M. Kibria, T. Szkopek, *et al.*, "p-Type InN Nanowires," *Nano Lett.*, vol. 13, pp. 5509-5513, 2013.
[138] V. M. Polyakov, F. Schwierz, F. Fuchs, J. Furthmüller, and F. Bechstedt, "Low-field and high-field electron transport in zinc blende InN," *Appl. Phys. Lett.*, vol. 94, p. 022102, 2009.
[139] S. Zhao and Z. Mi, "Is the Fermi-level pinned on InN grown surfaces?," *Phys. Stat. Sol. (c)*, 2014.
[140] H. P. Nguyen, S. Zhang, A. T. Connie, M. G. Kibria, Q. Wang, I. Shih, *et al.*, "Breaking the carrier injection bottleneck of phosphor-free nanowire white light-emitting diodes," *Nano Lett.*, vol. 13, pp. 5437-42, Nov 13 2013.
[141] H. P. Nguyen, K. Cui, S. Zhang, M. Djavid, A. Korinek, G. A. Botton, *et al.*, "Controlling electron overflow in phosphor-free InGaN/GaN nanowire white light-emitting diodes," *Nano Lett.*, vol. 12, pp. 1317-23, Mar 14 2012.
[142] F. Glas, "Critical dimensions for the plastic relaxation of strained axial heterostructures in free-standing nanowires," *Phys. Rev. B*, vol. 74, p. 121302, 2006.

[143] Z. Mi, S. Zhao, S. Woo, M. Bugnet, M. Djavid, X. Liu, *et al.*, "Molecular beam epitaxial growth and characterization of Al (Ga) N nanowire deep ultraviolet light emitting diodes and lasers," *J. Phys. D: Appl. Phys.*, vol. 49, pp. 364006-364013, 2016.
[144] Q. Wang, A. T. Connie, H. P. Nguyen, M. G. Kibria, S. Zhao, S. Sharif, *et al.*, "Highly efficient, spectrally pure 340 nm ultraviolet emission from AlxGa(1)-xN nanowire based light emitting diodes," *Nanotechnology*, vol. 24, p. 345201, Aug 30 2013.
[145] S. Zhao, A. T. Connie, M. H. Dastjerdi, X. H. Kong, Q. Wang, M. Djavid, *et al.*, "Aluminum nitride nanowire light emitting diodes: Breaking the fundamental bottleneck of deep ultraviolet light sources," *Sci. Rep.*, vol. 5, p. 8332, 2015.
[146] S. Zhao, M. Djavid, and Z. Mi, "Surface Emitting, High Efficiency Near-Vacuum Ultraviolet Light Source with Aluminum Nitride Nanowires Monolithically Grown on Silicon," *Nano Lett.*, vol. 15, pp. 7006-7009, 2015.
[147] I. Tiginyanu, V. Ursaki, V. Zalamai, S. Langa, S. Hubbard, D. Pavlidis, *et al.*, "Luminescence of GaN nanocolumns obtained by photon-assisted anodic etching," *Appl. Phys. Lett.*, vol. 83, pp. 1551-1553, 2003.
[148] M. Endo, Z. Jin, S. Kasai, and H. Hasegawa, "Reactive ion beam etching of GaN and AlGaN/GaN for nanostructure fabrication using methane-based gas mixtures," *Japanese J. Appl. Phys.*, vol. 41, p. 2689, 2002.
[149] S.-Y. Park, S. J. Di Giacomo, R. Anisha, P. R. Berger, P. E. Thompson, and I. Adesida, "Fabrication of nanowires with high aspect ratios utilized by dry etching with SF6: C4F8 and self-limiting thermal oxidation on Si substrate," *J. Vac. Sci. Technol. B*, vol. 28, pp. 763-768, 2010.
[150] H. Peng, X. Zhou, N. Wang, Y. Zheng, L. Liao, W. Shi, *et al.*, "Bulk-quantity GaN nanowires synthesized from hot filament chemical vapor deposition," *Chem. Phys. Lett.*, vol. 327, pp. 263-270, 2000.
[151] R. Debnath, R. Meijers, T. Richter, T. Stoica, R. Calarco, and H. Lüth, "Mechanism of molecular beam epitaxy growth of GaN nanowires on Si (111)," *App. Phys. Lett.*, vol. 90, p. 123117, 2007.
[152] K. A. Bertness, A. Roshko, L. M. Mansfield, T. E. Harvey, and N. A. Sanford, "Mechanism for spontaneous growth of GaN nanowires with molecular beam epitaxy," *J. Crys. Growth*, vol. 310, pp. 3154-3158, 2008.
[153] P. Mohseni, C. Maunders, G. Botton, and R. LaPierre, "GaP/GaAsP/GaP core–multishell nanowire heterostructures on (111) silicon," *Nanotechnology*, vol. 18, p. 445304, 2007.
[154] T. Kuykendall, P. Ulrich, S. Aloni, and P. Yang, "Complete composition tunability of InGaN nanowires using a combinatorial approach," *Nat. Mater.*, vol. 6, pp. 951-956, 2007.
[155] R. S. Wagner and W. C. Ellis, *Appl. Phys. Lett.*, vol. 4, p. 89, 1964.
[156] Y. Wu and P. Yang, "Direct observation of vapor-liquid-solid nanowire growth," *J. Ameri. Chem. Soci.*, vol. 123, pp. 3165-3166, 2001.
[157] D. Dheeraj, H. Zhou, A. Moses, T. Hoang, A. Van Helvoort, B. Fimland, *et al.*, "Heterostructured III-V Nanowires with Mixed Crystal Phases Grown by Au-assisted Molecular Beam Epitaxy," *Nanowires, InTech*, 2010.
[158] W. I. Park, G. Zheng, X. Jiang, B. Tian, and C. M. Lieber, "Controlled synthesis of millimeter-long silicon nanowires with uniform electronic properties," *Nano letters*, vol. 8, pp. 3004-3009, 2008.
[159] Z. Cai, S. Garzon, M. Chandrashekhar, R. Webb, and G. Koley, "Synthesis and properties of high-quality InN nanowires and nanonetworks," *J. Electrochem. Mater.*, vol. 37, pp. 585-592, 2008.
[160] V. Gottschalch, G. Wagner, J. Bauer, H. Paetzelt, and M. Shirnow, "VLS growth of GaN nanowires on various substrates," *J. Crys. Growth*, vol. 310, pp. 5123-5128, 2008.
[161] E. Stern, G. Cheng, E. Cimpoiasu, R. Klie, S. Guthrie, J. Klemic, *et al.*, "Electrical characterization of single GaN nanowires," *Nanotechnology*, vol. 16, p. 2941, 2005.
[162] S. Kang, B. Kang, and D. Yoon, "Growth and properties of vertically well-aligned GaN nanowires by thermal chemical vapor deposition process," *Mater. Lett.*, vol. 65, pp. 763-765, 2011.
[163] Z. Yan and A. Milnes, "Deep level transient spectroscopy of silver and gold levels in LEC grown gallium arsenide," *J. Electrochem. Soc.*, vol. 129, pp. 1353-1356, 1982.

[164] L. J. Lauhon, M. S. Gudiksen, D. Wang, and C. M. Lieber, "Epitaxial core–shell and core–multishell nanowire heterostructures," *Nature,* vol. 420, pp. 57-61, 2002.
[165] J. Ristić, M. Sánchez-García, J. Ulloa, E. Calleja, J. Sanchez-Páramo, J. Calleja, *et al.*, "AlGaN nanocolumns and AlGaN/GaN/AlGaN nanostructures grown by molecular beam epitaxy," *Phys. Stat. Sol. (b),* vol. 234, pp. 717-721, 2002.
[166] P. Dogan, O. Brandt, C. Pfüller, J. Lähnemann, U. Jahn, C. Roder, *et al.*, "Formation of high-quality GaN microcrystals by pendeoepitaxial overgrowth of GaN nanowires on Si (111) by molecular beam epitaxy," *Cryst. Growth Des.*, vol. 11, pp. 4257-4260, 2011.
[167] S. Fan, S. Zhao, X. Liu, and Z. Mi, "Study on the coalescence of dislocation-free GaN nanowires on Si and SiOx," *J. Vac. Sci. Technol. B,* vol. 32, p. 02C114, 2014.
[168] K. Kato, K. Kishino, H. Sekiguchi, and A. Kikuchi, "Overgrowth of GaN on Be-doped coalesced GaN nanocolumn layer by rf-plasma-assisted molecular-beam epitaxy—Formation of high-quality GaN microcolumns," *J. Crys. Growth,* vol. 311, pp. 2956-2961, 2009.
[169] V. Consonni, M. Knelangen, U. Jahn, A. Trampert, L. Geelhaar, and H. Riechert, "Effects of nanowire coalescence on their structural and optical properties on a local scale," *Appl. Phys. Lett.,* vol. 95, p. 241910, 2009.
[170] K. A. Grossklaus, A. Banerjee, S. Jahangir, P. Bhattacharya, and J. M. Millunchick, "Misorientation defects in coalesced self-catalyzed GaN nanowires," *J. Crys. Growth,* vol. 371, pp. 142-147, 2013.
[171] B. Jenichen, O. Brandt, C. Pfuller, P. Dogan, M. Knelangen, and A. Trampert, "Macro- and micro-strain in GaN nanowires on Si(111)," *Nanotechnology,* vol. 22, p. 295714, Jul 22 2011.
[172] V. Kaganer, B. Jenichen, O. Brandt, S. Fernández-Garrido, P. Dogan, L. Geelhaar, *et al.*, "Inhomogeneous strain in GaN nanowires determined from x-ray diffraction peak profiles," *Phys. Rev. B,* vol. 86, p. 115325, 2012.
[173] S. Fernández-Garrido, V. Kaganer, C. Hauswald, B. Jenichen, M. Ramsteiner, V. Consonni, *et al.*, "Correlation between the structural and optical properties of spontaneously formed GaN nanowires: a quantitative evaluation of the impact of nanowire coalescence," *Nanotechnology,* vol. 25, p. 455702, 2014.
[174] M. Djavid and Z. Mi, "Enhancing the light extraction efficiency of AlGaN deep ultraviolet light emitting diodes by using nanowire structures," *App. Phys. Lett.,* vol. 108, p. 051102, 2016.
[175] B. Joyce and J. Baldrey, "Selective epitaxial deposition of silicon," *Nature,* vol. 195, pp. 485-486, 1962.
[176] F. Tausch and A. Lapierre, "A novel crystal growth phenomenon: single crystal GaAs overgrowth onto silicon dioxide," *J. Electrochem. Soc.,* vol. 112, pp. 706-709, 1965.
[177] P. Rai-Choudhury, "Epitaxial gallium arsenide from trimethyl gallium and arsine," *J. Electrochem. Soc.,* vol. 116, pp. 1745-1746, 1969.
[178] S. H. Jones and K. M. Lau, "Selective area growth of high quality GaAs by OMCVD using native oxide masks," *J. Electrochem. Soc.,* vol. 134, pp. 3149-3155, 1987.
[179] H. Paetzelt, V. Gottschalch, J. Bauer, G. Benndorf, and G. Wagner, "Selective-area growth of GaAs and InAs nanowires—homo- and heteroepitaxy using templates," *J. Crys. Growth,* vol. 310, pp. 5093-5097, 2008.
[180] S. Hertenberger, D. Rudolph, M. Bichler, J. J. Finley, G. Abstreiter, and G. Koblmüller, "Growth kinetics in position-controlled and catalyst-free InAs nanowire arrays on Si(111) grown by selective area molecular beam epitaxy," *J. Appl. Phys.,* vol. 108, p. 114316, 2010.
[181] T. Schumann, T. Gotschke, F. Limbach, T. Stoica, and R. Calarco, "Selective-area catalyst-free MBE growth of GaN nanowires using a patterned oxide layer," *Nanotechnology,* vol. 22, p. 095603, Mar 4 2011.
[182] H. Sekiguchi, K. Kishino, and A. Kikuchi, "Ti-mask selective-area growth of GaN by RF-plasma-assisted molecular-beam epitaxy for fabricating regularly arranged InGaN/GaN nanocolumns," *Appl. Phys. Exp.,* vol. 1, p. 124002, 2008.

[183] K. A. Bertness, A. W. Sanders, D. M. Rourke, T. E. Harvey, A. Roshko, J. B. Schlager, *et al.*, "Controlled nucleation of GaN nanowires grown with molecular beam epitaxy," *Adv. Func. Mater.*, vol. 20, pp. 2911-2915, 2010.
[184] J. Motohisa, J. Noborisaka, J. Takeda, M. Inari, and T. Fukui, "Catalyst-free selective-area MOVPE of semiconductor nanowires on (111)B oriented substrates," *J. Crys. Growth,* vol. 272, pp. 180-185, 2004.
[185] S. D. Hersee, X. Sun, and X. Wang, "The controlled growth of GaN nanowires," *Nano Lett.*, vol. 6, pp. 1808-1811, 2006.
[186] K. Kishino, H. Sekiguchi, and A. Kikuchi, "Improved Ti-mask selective-area growth (SAG) by rf-plasma-assisted molecular beam epitaxy demonstrating extremely uniform GaN nanocolumn arrays," *J. Crys. Growth,* vol. 311, pp. 2063-2068, 2009.
[187] H. Sekiguchi, K. Kishino, and A. Kikuchi, "Emission color control from blue to red with nanocolumn diameter of InGaN/GaN nanocolumn arrays grown on same substrate," *Appl. Phys. Lett.*, vol. 96, pp. 231104-231104-3, 2010.
[188] H. Sekiguchi, K. Kishino, and A. Kikuchi, "Emission color control from blue to red with nanocolumn diameter of InGaN/GaN nanocolumn arrays grown on same substrate," *Appl. Phys. Lett.*, vol. 96, p. 231104, 2010.
[189] K. Kishino, A. Yanagihara, K. Ikeda, and K. Yamano, "Monolithic integration of four-colour InGaN-based nanocolumn LEDs," *Electronics Letters,* vol. 51, pp. 852-854, 2015.
[190] K. Kishino and K. Yamano, "Green-light nanocolumn light emitting diodes with triangular-lattice uniform arrays of InGaN-based nanocolumns," *IEEE Journal of Quantum Electronics,* vol. 50, pp. 538-547, 2014.
[191] R. Vadivelu, Y. Igawa, and K. Kishino, "633 nm red emissions from InGaN nanocolumn light-emitting diode by radio frequency plasma assisted molecular beam epitaxy," *Japanese J. Appl. Phys.*, vol. 52, p. 08JE18, 2013.
[192] Y.-H. Ra, R. Wang, S. Y.-M. Woo, M. Djavid, S. M. Sadaf, J. Lee, *et al.*, "Full-Color Single Nanowire Pixels for Projection Displays," *Nano Lett.*, 2016.
[193] K. Kishino, T. Hoshino, S. Ishizawa, and A. Kikuchi, "Selective-area growth of GaN nanocolumns on titanium-mask-patterned silicon (111) substrates by RF-plasma-assisted molecular-beam epitaxy," *Electronics Letters,* vol. 44, p. 819, 2008.
[194] K. Tomioka, K. Ikejiri, T. Tanaka, J. Motohisa, S. Hara, K. Hiruma, *et al.*, "Selective-area growth of III-V nanowires and their applications," *J. Mater. Res.*, vol. 26, pp. 2127-2141, 2011.
[195] K. Yamano, K. Kishino, H. Sekiguchi, T. Oto, A. Wakahara, and Y. Kawakami, "Novel selective area growth (SAG) method for regularly arranged AlGaN nanocolumns using nanotemplates," *J. Crys. Growth,* vol. 425, pp. 316-321, 2015.
[196] H. Taketomi, Y. Aoki, Y. Takagi, A. Sugiyama, M. Kuwabara, and H. Yoshida, "Over 1 W record-peak-power operation of a 338 nm AlGaN multiple-quantum-well laser diode on a GaN substrate," *Japanese J. Appl. Phys.*, vol. 55, p. 05FJ05, 2016.
[197] Y. Aoki, M. Kuwabara, Y. Yamashita, Y. Takagi, A. Sugiyama, and H. Yoshida, "A 350-nm-band GaN/AlGaN multiple-quantum-well laser diode on bulk GaN," *Appl. Phys. Lett.*, vol. 107, p. 151103, 2015.
[198] H. Yoshida, Y. Yamashita, M. Kuwabara, and H. Kan, "A 342-nm ultraviolet AlGaN multiple-quantum-well laser diode," *Nat. Photon.*, vol. 2, pp. 551-554, 2008.
[199] H. Yoshida, Y. Yamashita, M. Kuwabara, and H. Kan, "Demonstration of an ultraviolet 336 nm AlGaN multiple-quantum-well laser diode," *Appl. Phys. Lett.*, vol. 93, p. 241106, 2008.
[200] Y. Hou, P. Renwick, B. Liu, J. Bai, and T. Wang, "Room temperature plasmonic lasing in a continuous wave operation mode from an InGaN/GaN single nanorod with a low threshold," *Sci Rep,* vol. 4, p. 5014, 2014.

[201] P. Anderson, C. Swartz, D. Carder, R. Reeves, S. Durbin, S. Chandril, *et al.*, "Buried p-type layers in Mg-doped InN," *Appl. Phys. Lett.*, vol. 89, p. 184104, 2006.
[202] M. A. Mayer, S. Choi, O. Bierwagen, H. M. Smith III, E. E. Haller, J. S. Speck, *et al.*, "Electrical and optical properties of p-type InN," *J. Appl. Phys.*, vol. 110, p. 123707, 2011.
[203] X. Wang, S.-B. Che, Y. Ishitani, and A. Yoshikawa, "Growth and properties of Mg-doped In-polar InN films," *Appl. Phys. Lett.*, vol. 90, p. 201913, 2007.
[204] N. Khan, N. Nepal, A. Sedhain, J. Lin, and H. Jiang, "Mg acceptor level in InN epilayers probed by photoluminescence," *Appl. Phys. Lett.*, vol. 91, pp. 012101-012101-3, 2007.
[205] J. Ager, N. Miller, R. Jones, K. Yu, J. Wu, W. Schaff, *et al.*, "Mg-doped InN and InGaN–Photoluminescence, capacitance–voltage and thermopower measurements," *Phys. Stat. Sol. (b)*, vol. 245, pp. 873-877, 2008.
[206] L. H. Dmowski, M. Baj, L. Konczewicz, T. Suski, D. K. Maude, S. Grzanka, *et al.*, "Coexistence of free holes and electrons in InN:Mg with In- and N-growth polarities," *J. Appl. Phys.*, vol. 111, p. 093719, 2012.
[207] X. Wang, S.-B. Che, Y. Ishitani, and A. Yoshikawa, "Hole mobility in Mg-doped< equation> p</equation>-type InN films," *Appl. Phys. Lett.*, vol. 92, pp. 132108-132108-3, 2008.
[208] I. Mahboob, T. Veal, C. McConville, H. Lu, and W. Schaff, "Intrinsic electron accumulation at clean InN surfaces," *Phys. Rev. Lett.*, vol. 92, p. 036804, 2004.
[209] Q. Hang, F. Wang, W. E. Buhro, and D. B. Janes, "Ambipolar conduction in transistors using solution grown InAs nanowires with Cd doping," *Appl. Phys. Lett.*, vol. 90, p. 062108, 2007.
[210] W. Linhart, J. Chai, R. J. Morris, M. Dowsett, C. F. McConville, S. Durbin, *et al.*, "Giant reduction of InN surface electron accumulation: Compensation of surface donors by Mg dopants," *Phys. Rev. Lett.*, vol. 109, p. 247605, 2012.
[211] S. Li, K. Yu, J. Wu, R. Jones, W. Walukiewicz, J. Ager, *et al.*, "Fermi-level stabilization energy in group III nitrides," *Phys. Rev. B*, vol. 71, 2005.
[212] D. Wang, Q. Wang, A. Javey, R. Tu, H. Dai, H. Kim, *et al.*, "Germanium nanowire field-effect transistors with SiO 2 and high-κ HfO 2 gate dielectrics," *Appl. Phys. Lett.*, vol. 83, pp. 2432-2434, 2003.
[213] Z. Zhong, F. Qian, D. Wang, and C. M. Lieber, "Synthesis of p-type gallium nitride nanowires for electronic and photonic nanodevices," *Nano Lett.*, vol. 3, pp. 343-346, 2003.
[214] M. A. B. S. Sørensen, C. B. Sørensen, P. E. Lindelof, K. L. Martinez, and J. Nygård, "Ambipolar transistor behavior in p-doped InAs nanowires grown by molecular beam epitaxy," *Appl. Phys. Lett.*, 2008.
[215] M. Radosavljevic, M. Freitag, K. Thadani, and A. Johnson, "Nonvolatile molecular memory elements based on ambipolar nanotube field effect transistors," *Nano Lett.*, vol. 2, pp. 761-764, 2002.
[216] Lay-Lay Chua1, Jana Zaumseil1, Jui-Fen Chang1, Eric C.-W. Ou3, Peter K.-H. Ho1,2, Henning Sirringhaus1 & Richard H. Friend1, "General observation of n-type field-effect behaviour in organic semiconductors," *Nature*, vol. 434, pp. 192-4, Mar 10 2005.
[217] C. M. Aguirre, P. L. Levesque, M. Paillet, F. Lapointe, B. C. St-Antoine, P. Desjardins, *et al.*, "The Role of the Oxygen/Water Redox Couple in Suppressing Electron Conduction in Field-Effect Transistors," *Adv. Mater.*, vol. 21, pp. 3087-3091, 2009.
[218] Y.-W. Song, "Photoluminescence of High Quality Epitaxial p-type InN," PhD, University of Canterbury, 2013.
[219] S. Zhao, X. Liu, and Z. Mi, "Photoluminescence properties of Mg-doped InN nanowires," *Appl. Phys. Lett.*, vol. 103, p. 203113, 2013.
[220] S. Zhao, H. P. Nguyen, M. G. Kibria, and Z. Mi, "III-Nitride nanowire optoelectronics," *Progress in Quantum Electronics*, vol. 44, pp. 14-68, 2015.
[221] A. T. Connie, S. Zhao, S. M. Sadaf, I. Shih, Z. Mi, X. Du, *et al.*, "Optical and electrical properties of Mg-doped AlN nanowires grown by molecular beam epitaxy," *Appl. Phys. Lett.*, vol. 106, p. 213105, 2015.

[222] S. Zhao, A. Connie, B. Le, X. Kong, H. Guo, X. Du, *et al.*, "p-Type AlN nanowires and AlN nanowire light emitting diodes on Si," in *Summer Topicals Meeting Series (SUM)*, pp. 131-132, 2015.
[223] K. Li, X. Liu, Q. Wang, S. Zhao, and Z. Mi, "Ultralow-threshold electrically injected AlGaN nanowire ultraviolet lasers on Si operating at low temperature," *Nat. Nanotech.*, vol. 10, pp. 140-144, 2015.
[224] A. Bengoechea-Encabo, F. Barbagini, S. Fernández-Garrido, J. Grandal, J. Ristic, M. A. Sanchez-Garcia, *et al.*, "Understanding the selective area growth of GaN nanocolumns by MBE using Ti nanomasks," *J. Crys. Growth*, vol. 325, pp. 89-92, 2011.
[225] B. H. Le, S. Zhao, X. Liu, S. Y. Woo, G. A. Botton, and Z. Mi, "Controlled Coalescence of AlGaN Nanowire Arrays: An Architecture for Nearly Dislocation-Free Planar Ultraviolet Photonic Device Applications," *Adv. Mater.*, 2016.
[226] T. Gotschke, T. Schumann, F. Limbach, T. Stoica, and R. Calarco, "Influence of the adatom diffusion on selective growth of GaN nanowire regular arrays," *Appl. Phys. Lett.*, vol. 98, p. 103102, 2011.
[227] E. Iliopoulos and T. Moustakas, "Growth kinetics of AlGaN films by plasma-assisted molecular-beam epitaxy," *Appl. Phys. Lett.*, vol. 81, pp. 295-297, 2002.
[228] S. Zhao, S. Woo, M. Bugnet, X. Liu, J. Kang, G. A. Botton, *et al.*, "Three-dimensional quantum confinement of charge carriers in self-organized AlGaN nanowires: A viable route to electrically injected deep ultraviolet lasers," *Nano Lett.*, vol. 15, pp. 7801-7807, 2015.
[229] A. Pierret, C. Bougerol, S. Murcia-Mascaros, A. Cros, H. Renevier, B. Gayral, *et al.*, "Growth, structural and optical properties of AlGaN nanowires in the whole composition range," *Nanotechnology*, vol. 24, p. 115704, 2013.
[230] J. massZhang, S. Wu, S. Rai, V. Mandavilli, V. Adivarahan, A. Chitnis, *et al.*, "AlGaN multiple-quantum-well-based, deep ultraviolet light-emitting diodes with significantly reduced long-wave emission," *Appl. Phys. Lett.*, vol. 83, p. 3456, 2003.
[231] T. Deguchi, "Quantum-confined Stark effect in an AlGaN/GaN/AlGaN single quantum well structure," *Japanese J. Appl. Phys.*, vol. 38, p. 914, 1999.
[232] A. Chakraborty, K. Kim, F. Wu, J. Speck, S. DenBaars, and U. Mishra, "Defect reduction in nonpolar a-plane GaN films using in situ SiNx nanomask," *Appl. Phys. Lett.*, vol. 89, 2006.
[233] N. Sawaki, T. Hikosaka, N. Koide, S. Tanaka, Y. Honda, and M. Yamaguchi, "Growth and properties of semi-polar GaN on a patterned silicon substrate," *J. Crys. Growth*, vol. 311, pp. 2867-2874, 2009.
[234] T.-W. Yeh, Y.-T. Lin, L. S. Stewart, P. D. Dapkus, R. Sarkissian, J. D. O'Brien, *et al.*, "InGaN/GaN multiple quantum wells grown on nonpolar facets of vertical GaN nanorod arrays," *Nano Lett.*, vol. 12, pp. 3257-3262, 2012.
[235] A. K. Rishinaramangalam, M. Nami, M. N. Fairchild, D. M. Shima, G. Balakrishnan, S. Brueck, *et al.*, "Semipolar InGaN/GaN nanostructure light-emitting diodes on c-plane sapphire," *Appl. Phys. Exp.*, vol. 9, p. 032101, 2016.
[236] Q. Li, Y. Lin, J. R. Creighton, J. J. Figiel, and G. T. Wang, "Nanowire-Templated Lateral Epitaxial Growth of Low-Dislocation Density Nonpolar a-Plane GaN on r-Plane Sapphire," *Adv. Mater.*, vol. 21, pp. 2416-2420, 2009.
[237] W. Shockley and W. Read, "Quantitative predictions from dislocation models of crystal grain boundaries," *Phys. Rev. B*, vol. 75, p. 692, 1949.
[238] A. Bengoechea-Encabo, F. Barbagini, S. Fernandez-Garrido, J. Grandal, J. Ristic, M. A. Sanchez-Garcia, *et al.*, "Understanding the selective area growth of GaN nanocolumns by MBE using Ti nanomasks," *J. Crys. Growth*, vol. 325, pp. 89-92, 2011.
[239] E. Calleja Pardo, A. Bengoechea Encabo, S. Albert, M. A. Sánchez García, F. Barbagini, E. Luna, *et al.*, "Understanding the Selective Area Nucleation and Growth of GaN nanocolumns by MBE using Ti nanomasks," *J. Crys. Growth*, vol. 325, pp. 89-92, 2011.

[240] J. J. Wierer Jr, Q. Li, D. D. Koleske, S. R. Lee, and G. T. Wang, "III-nitride core–shell nanowire arrayed solar cells," *Nanotechnology*, vol. 23, p. 194007, 2012.
[241] J. Speck and S. Nakamura, "Realization of high hole concentrations in M9 doped semipolar (101-1-) GaN," *Appl. Phys. Lett.*, vol. 89, p. 202104, 2006.
[242] L. Lahourcade, J. Pernot, A. Wirthmuller, M.-P. Chauvat, P. Ruterana, A. Laufer, *et al.*, "Mg doping and its effect on the semipolar GaN (1122) growth kinetics," *Appl. Phys. Lett.*, vol. 95, p. 171908, 2009.
[243] M. Nakarmi, K. Kim, M. Khizar, Z. Fan, J. Lin, and H. Jiang, "Electrical and optical properties of Mg-doped Al0. 7Ga0. 3N alloys," *Appl. Phys. Lett.*, vol. 86, pp. 92108-92500, 2005.
[244] A. Chakraborty, C. G. Moe, Y. Wu, T. Mates, S. Keller, J. S. Speck, *et al.*, "Electrical and structural characterization of Mg-doped p-type Al0. 69Ga0. 31N films on SiC substrate," *J. Appl. Phys.*, vol. 101, p. 3717, 2007.
[245] M. L. Nakarmi, K. H. Kim, J. Li, J. Y. Lin, and H. X. Jiang, "Enhanced p-type conduction in GaN and AlGaN by Mg-δ-doping," *Appl. Phys. Lett.*, vol. 82, p. 3041, 2003.
[246] T. Tanaka, A. Watanabe, H. Amano, Y. Kobayashi, I. Akasaki, S. Yamazaki, *et al.*, "p-type conduction in Mg-doped GaN and Al0. 08Ga0. 92N grown by metalorganic vapor phase epitaxy," *Appl. Phys. Lett.*, vol. 65, pp. 593-594, 1994.
[247] H. M. Ng, D. Doppalapudi, D. Korakakis, R. Singh, and T. D. Moustakas, "MBE growth and doping of III–V nitrides," *J. Crys. Growth*, vol. 189, pp. 349-353, 1998.
[248] J. Yang, F. Yang, T. Kent, M. Mills, and R. Myers, "Semipolar InN/AlN multiple quantum wells on {10 1^{-} 5} faceted AlN on silicon," *Appl. Phys. Lett.*, vol. 103, p. 121105, 2013.
[249] A. Cullis, "Strain-Induced Modulations in the Surface Morphology of Heteroepitaxial Layers," *Mrs Bulletin*, vol. 21, pp. 21-26, 1996.
[250] A. Toropov, E. Shevchenko, T. Shubina, V. Jmerik, D. Nechaev, M. Yagovkina, *et al.*, "Suppression of the quantum-confined Stark effect in $Al_xGa_{1-x}N/Al_yGa_{1-y}N$ corrugated quantum wells," *J. Appl. Phys.*, vol. 114, p. 124306, 2013.
[251] Y.-S. Chen, C.-H. Liao, Y.-C. Cheng, C.-T. Kuo, and H.-C. Wang, "Nanostructure study of the coalescence growth of GaN columns with molecular beam epitaxy," *Opt. Mater. Exp.*, vol. 3, pp. 1450-1458, 2013.
[252] M. Conroy, V. Z. Zubialevich, H. Li, N. Petkov, S. O'Donoghue, J. D. Holmes, *et al.*, "Ultra-High Density Arrays of Defect Free AlN Nanorods: A 'Space Filling'Approach," *ACS nano*, 2015.
[253] S. Y. Woo, M. Bugnet, H. P. Nguyen, Z. Mi, and G. A. Botton, "Atomic Ordering in InGaN Alloys within Nanowire Heterostructures," *Nano Lett.*, vol. 15, pp. 6413-6418, 2015.
[254] H. Peng, E. Makarona, Y. He, Y. Song, A. Nurmikko, J. Su, *et al.*, "Ultraviolet light-emitting diodes operating in the 340 nm wavelength range and application to time-resolved fluorescence spectroscopy," *Appl. Phys. Lett.*, vol. 85, pp. 1436-1438, 2004.
[255] V. Adivarahan, A. Chitnis, J. Zhang, M. Shatalov, J. Yang, G. Simin, *et al.*, "Ultraviolet light-emitting diodes at 340 nm using quaternary AlInGaN multiple quantum wells," *Appl. Phys. Lett.*, vol. 79, pp. 4240-4242, 2001.
[256] S.-R. Jeon, M. Gherasimova, Z. Ren, J. Su, G. Cui, J. Han, *et al.*, "High performance AlGaInN ultraviolet light-emitting diode at the 340 nm wavelength," *Japanese J. Appl. Phys.*, vol. 43, p. L1409, 2004.
[257] A. Yasan, R. McClintock, K. Mayes, S. Darvish, H. Zhang, P. Kung, *et al.*, "Comparison of ultraviolet light-emitting diodes with peak emission at 340 nm grown on GaN substrate and sapphire," *Appl. Phys. Lett.*, vol. 81, pp. 2151-2153, 2002.
[258] G. Brummer, D. Nothern, A. Y. Nikiforov, and T. Moustakas, "Deep ultraviolet distributed Bragg reflectors based on graded composition AlGaN alloys," *App. Phys. Lett.*, vol. 106, p. 221107, 2015.
[259] S. Gradečak, F. Qian, Y. Li, H.-G. Park, and C. M. Lieber, "GaN nanowire lasers with low lasing thresholds," *Appl. Phys. Lett.*, vol. 87, p. 173111, 2005.
[260] J. C. Johnson, H.-J. Choi, K. P. Knutsen, R. D. Schaller, P. Yang, and R. J. Saykally, "Single gallium nitride nanowire lasers," *Nat. Mater.*, vol. 1, pp. 106-110, 2002.

[261] M. H. Huang, S. Mao, H. Feick, H. Yan, Y. Wu, H. Kind, *et al.*, "Room-temperature ultraviolet nanowire nanolasers," *Science*, vol. 292, pp. 1897-9, Jun 8 2001.
[262] Q. Li, J. B. Wright, W. W. Chow, T. S. Luk, I. Brener, L. F. Lester, *et al.*, "Single-mode GaN nanowire lasers," *Opt. Exp.*, vol. 20, pp. 17873-17879, 2012.
[263] Y. Xiao, C. Meng, P. Wang, Y. Ye, H. Yu, S. Wang, *et al.*, "Single-nanowire single-mode laser," *Nano Lett.*, vol. 11, pp. 1122-1126, 2011.
[264] M. Kneissl, D. W. Treat, M. Teepe, N. Miyashita, and N. M. Johnson, "Ultraviolet InAlGaN multiple-quantum-well laser diodes," *Phys. Stat. Sol. (a)*, vol. 200, pp. 118-121, 2003.
[265] M. Kneissl, D. W. Treat, M. Teepe, N. Miyashita, and N. M. Johnson, "Continuous-wave operation of ultraviolet InGaN/InAlGaN multiple-quantum-well laser diodes," *Appl. Phys. Lett.*, vol. 82, pp. 2386-2388, 2003.
[266] J. Heo, W. Guo, and P. Bhattacharya, "Monolithic single GaN nanowire laser with photonic crystal microcavity on silicon," *Appl. Phys. Lett.*, vol. 98, p. 021110, 2011.
[267] H. P. T. Nguyen, K. Cui, S. Zhang, S. Fathololoumi, and Z. Mi, "Full-color InGaN/GaN dot-in-a-wire light emitting diodes on silicon," *Nanotechnology*, vol. 22, p. 445202, 2011.
[268] S. Zhao, S. Woo, S. Sadaf, Y. Wu, A. Pofelski, D. Laleyan, *et al.*, "Molecular beam epitaxy growth of Al-rich AlGaN nanowires for deep ultraviolet optoelectronics," *APL Materials*, vol. 4, p. 086115, 2016.
[269] Q. Zhang, G. Li, X. Liu, F. Qian, Y. Li, T. C. Sum, *et al.*, "A room temperature low-threshold ultraviolet plasmonic nanolaser," *Nat. Commun.*, vol. 5, p. 4953, 2014.
[270] Y. Bian and Q. Gong, "Deep-subwavelength light confinement and transport in hybrid dielectric-loaded metal wedges," *Laser & Photonics Reviews*, vol. 8, pp. 549-561, 2014.
[271] T. P. Sidiropoulos, S. Geburt, R. Roder, M. Ogrisek, S. A. Maier, C. Ronning, *et al.*, "Room temperature plasmonic nanowire laser near the surface plasmon frequency," in *Lasers and Electro-Optics Europe (CLEO EUROPE/IQEC), 2013 Conference on and International Quantum Electronics Conference*, 2013, pp. 1-1.
[272] R. M. Ma, R. F. Oulton, V. J. Sorger, and X. Zhang, "Plasmon lasers: coherent light source at molecular scales," *Laser & Photonics Reviews*, vol. 7, pp. 1-21, 2013.